

Relativistic Mean-Field Description of Exotic Excitations in Finite Nuclei

Dissertation
von
Nils Paar

Institut für Theoretische Physik T30
Physik-Department
Technische Universität München



May 2003

Physik-Department der Technischen Universität München
Theoretische Physik T30

Relativistic Mean-Field Description of Exotic Excitations in Finite Nuclei

Nils Paar

Vollständiger Abdruck der von der Fakultät für Physik der Technischen Universität München zur Erlangung des akademischen Grades eines

Doktors der Naturwissenschaften (Dr. rer. nat.)

genehmigten Dissertation.

Vorsitzender: Univ.-Prof. Dr. R. Krücken
Prüfer der Dissertation: 1. Univ.-Prof. Dr. P. Ring
2. Apl.-Prof. Dr. H. Hofmann

Die Dissertation wurde am 22.5.2003 bei der Technischen Universität München eingereicht und durch die Fakultät für Physik am 23.6.2003 angenommen.

Acknowledgments

This work would not have been possible without the valuable support and help that I have received from many people.

In particular, I am very grateful to Prof. Dr. Peter Ring for the supervision of my work and for the continuous support over the past three years, as well as for stimulating discussions, and for numerous opportunities to learn as well as attend conferences and workshops. I would also like to acknowledge, with gratitude, the hospitality at the Technische Universität München.

I should like to thank Prof. Dr. Dario Vretenar for useful suggestions and discussions on many topics of this work, within the collaboration with the nuclear theory group from the Physics Department at the University of Zagreb. In respect of the first studies of the pygmy resonances, I would like to thank Prof. Dr. Georgios Lalazissis for very useful conversations and supporting advice. It is a pleasure to thank Tamara Nikšić for frequent and helpful exchanges of ideas, and computer codes, over the past years, and for reading and commenting on the whole manuscript.

I am grateful to Dr. Andreas Wandelt for kindly sharing his knowledge and computer codes on relativistic RPA, and for help during my first months at the TU Physics department. I am especially thankful to Dr. Roger Hilton for drawing to my attention many important issues related to this work, and for a careful reading and revision of the manuscript. I am very grateful to Dr. Milena Serra for sharing her knowledge on the relativistic two-body matrix elements, and for important technical support at the final stage of my work.

Furthermore, for support and stimulating discussions, I thank Dr. A. Ansari, Daniel Peña Aerteaga, Dr. Paolo Finelli and all the other colleagues and guests at the Physics Department of the TU-Muenchen. In addition, I thank Dr. Marko Kralj, Dr. Antonio Šiber, Prof. Krešo Tomljenović, Damir Rister and Dipl. Phys. Ivica Zerec for many enlightening and stimulating discussions, sometimes leading to the belief that we actually "understand the world".

Finally, I should like to thank my family for support and understanding whilst I have been away from home. Above all, the most important "thanks" goes to Tanja Bizjak for her love, patience, and encouragement whilst working on this thesis.

This work has been supported in part by the Bundesministerium für Bildung und Forschung.

Contents

Introduction	1
1 Basic Concepts of the Relativistic Mean Field Theory	9
1.1 Relativistic Lagrangian Density	10
1.2 Covariant Density Functional Theory	12
1.3 Equations of Motion in the Relativistic Mean Field Approximation	16
1.4 Relativistic Hartree-Bogoliubov theory	19
2 Relativistic Quasiparticle Random Phase Approximation	25
2.1 Matrix Equations of Relativistic Quasi-Particle RPA	25
2.2 Relativistic QRPA in the RHB Canonical Basis	27
2.2.1 Fully Self-Consistent RQRPA equations	27
2.2.2 RQRPA Strength Distributions and Transition Densities	31
2.2.3 Spurious Solutions of the RQRPA Equations	32
2.2.4 Sum Rules of the Multipole Strength in Relativistic QRPA	38
3 Nature of the Multipole Excitations in Exotic Nuclei	43
3.1 Evolution of the Low-lying Isovector Dipole Response in Oxygen Isotopes	44
3.2 Pairing Effects on the Quadrupole Response in Drip-line Nuclei	52
3.3 Giant Resonances in Medium Light Neutron Rich Nuclei	56
3.4 Evolution of the Low-lying Isovector Dipole Strength in N=82 Isotones	62
3.5 Soft Collective Oscillations in Tin Isotopes	66
3.6 Pygmy Dipole Resonances in Stable Nuclei	74
4 Compression Modes in Finite Nuclei	81
4.1 Isoscalar Giant Monopole Resonance	81
4.2 The Puzzle of Isoscalar Dipole Strength Distribution	84
4.3 Toroidal Giant Dipole Resonances	86
5 Proton-Neutron Relativistic Quasiparticle RPA	93
5.1 Matrix Equations of the pn-RQRPA in the RHB Canonical Basis	95
5.2 An Illustrative Example - Isobaric Analog Resonances	98
5.3 Gamow-Teller resonance	101
5.4 Effects of the Dirac Sea in the Gamow-Teller sum-rule	103

Conclusion	107
A Relativistic Two-body Matrix Elements in the RQRPA Residual Interaction	111
B The Pairing Two-Body Matrix Elements	115
C Frequently Used Abbreviations	117
Bibliography	118
Curriculum Vitae	126
List of Publications	127

Introduction

One of the major challenges of nuclear physics is presently focused toward the exploration of exotic nuclei in the regions away from the valley of beta-stability [1]. Until recently, nuclear physics investigations, both experimentally and theoretically, have mainly been constrained to study nuclei with relatively small neutron-proton asymmetry. However, new experimental techniques with the radioactive nuclear beams have started to probe the unexplored regions of the nuclear chart, from stable nuclei toward the boundaries of nuclear existence, revealing interesting nuclear structure phenomena. The traditional nuclear structure models, which have been established mainly within the limited space around the valley of beta-stability, need to be reformulated to include the properties of exotic nuclei.

Knowledge about exotic nuclei may improve our present insight, not only into the origin of element abundances on the Earth, but also into the processes leading to the formation of matter in the universe. The chemical elements have been produced in violent nuclear reactions inside stars and supernovae explosions. At that stage, most nuclei were unstable, then followed by the nuclear reactions and decays toward stable nuclei. The fusion reactions inside stars, starting from the fusion of hydrogen into helium, are responsible for the production of elements up to iron. However, the origin of elements heavier than iron is still not fully understood. The most perspective paths for the formation of heavy nuclei are s-process, i.e. the slow neutron capture, and r-process, i.e. the rapid capture of neutrons. It is presumed that more than half of the elements heavier than $A=60$ are produced by the r-process, in a series of rapid neutron captures followed by β -decays. These events run only in environments with extremely high neutron densities. Under these conditions, the subsequent β -decays are much slower than the neutron captures leading to the formation of extremely neutron-rich nuclei. On the other side of the valley of stability, rp-processes (rapid proton capture), are relevant in the production of the proton-rich heavy nuclei. In general, it is assumed that in addition to more than 260 nuclei that are not subject to radioactive decay, probably more than 7000 different unstable nuclei exist.

Exotic nuclei became experimentally accessible after new accelerators, with improved high beam intensities and energies of radioactive ions, had been established. A large number of radioactive nuclei can also be produced in the fission nuclear reactors, from which the exotic nuclei are extracted into an accelerator for further studies. Experimental techniques have been steadily improved over the years, leading towards an excellent detection efficiency and resolution. Exotic isotopes can be produced by the breaking up of accelerated heavier nuclei either in the linear accelerator or in the heavy ion synchrotron.

By using the projectile fragmentation with in-flight separation, a large number of the produced exotic isotopes can be sorted out according to their nuclear mass and charge. Another technique is based on shooting at a target at rest using very intense beams, and producing unstable isotopes fixed in the target material from which they can be extracted for further use.

The properties of exotic nuclei are being studied in a series of major experimental facilities, e.g. NCSL, ORNL and ANL (USA), GSI (Germany), GANIL (France), RIKEN (Japan), CERN (Europe), Dubna (Russia), and TRIUMF (Canada). However, a new generation of radioactive ion beam facilities will strongly boost the nuclear structure studies of exotic nuclei, in particular the Rare Isotope Accelerator (RIA) in USA, the international accelerator facility for research with ions and anti-protons at GSI, and the Radioactive Ion Beam Factory (RIBF) in Japan [2].

Amongst the unique phenomena discovered in light exotic nuclei, particularly challenging are the halo structures composed from the weakly bound neutrons characterized by a large spatial extension of radial wave functions far from the core built from the rest of nucleons [3]. A very unusual behavior of neutron halos in light nuclei inspired many new experimental studies to map the nuclear chart in unknown regions, some close to the neutron and proton drip-lines. The existence of neutron skin is another interesting effect appearing in the neutron-rich medium-heavy and heavier nuclei. As the number of neutrons increases towards the drip-lines, the neutron density becomes extended in space beyond the proton density, giving rise to a neutron skin. In fact, in the neutron-rich weakly bound nuclei, both skins and halos can be expected [4]. Although nuclei beyond the particle drip-lines are unbound, it is not yet clear whether the existence of islands of stability on the other side from the drip-lines is possible. An extreme case of such a system would be a neutron star, bound together due to the equilibrium of gravitational force and the neutron degeneracy pressure.

Probably one of the most striking features in the nuclear structure of exotic nuclei are changes in the well known shell structure. In stable nuclei the magic numbers, $N, Z = 8, 20, 28, (40) 50, 82, 126$ and its origin are well identified. However, in the case of exotic neon, sodium and magnesium isotopes, experiments have shown that the shell closure at $N=20$ disappears [5]. In recent theoretical work it has been indicated that in neutron-rich nuclei new magic numbers appear, i.e. $N=6, 16, 34$, etc. instead of the usual magic numbers $N=8, 20, 40$, etc. [6]. This change has been explained by the strong attractive $V_{\tau\sigma}$ interaction, originating from the one boson exchange potential. In other studies, it has been shown that the single-particle spectra in exotic nuclei result with the shell quenching effects at extreme values of the isospin [7]. Therefore, the nuclear shell structure and magic numbers have to be systematically revised in the case of exotic nuclei.

The shell closure plays an important role to achieve the stability of nuclei composed from an extremely large number of protons and neutrons. Due to strong Coulomb repulsion in super-heavy nuclei, conditions of stability are not easy to obtain, i.e. typical production rates are one (or less) atom per week, and half lives are of the order of milliseconds. The location of the spherical super-heavy element is still an open question, although there have been some preliminary results suggesting possible existence of the stability island for $Z=114$ and $Z=118$ [8, 9]. According to the macroscopic-microscopic

models, the magic proton number is $Z=114$, in contrast to relativistic mean field models ($Z=120, N=172$), and Skyrme-Hartree Fock calculations ($Z=126, N=184$) [10].

Better insight into effects such as nuclear halos, neutron skins, proton-neutron pairing, new shell closures and exotic collective excitation phenomena may lead the way in theoretical efforts to achieve a consistent and unified model of the nucleus. At present time, only very light nuclei ($A < 10$) can be treated directly as clusters bound by a free nucleon-nucleon and three-nucleon forces. Another approach based on the shell-model calculations, is one of the best microscopic models of atomic nuclei. It includes the correlations among nucleons usually in the restricted space of valence nucleons, by using realistic nuclear interactions such as Kuo-Brown force and other modified versions [11]. Although this method has been very successful in the past, since the model space rapidly increases with the number of nucleons, practical calculations are extremely complex and limited only to the medium-mass nuclei. In recent years, the shell model has experienced an important evolution due to improvements in computational capacity, as well as new developments based on Monte-Carlo techniques, increasing the capability to treat configuration spaces with larger dimensions. However, their applications to heavy nuclei are still not possible. Alternative methods have been developed, in particular the self-consistent mean field theories, treating nucleons as independent particles moving in an average field generated by other nucleons. Probably the best known phenomenological mean-field effective interactions in nuclear physics, given by the Skyrme and Gogny energy functionals, have been developed over the past decades to achieve the present high-precision level in the analyzes of experimental data.

On the other side, models based on the relativistic meson-nucleon Lagrangians, especially its advanced density dependent versions, are nowadays capable of treating a wide range of properties in many regions of the nuclear chart. Our aim is to follow this theoretical course in the present work. Starting from the covariant density functional theory, for closed shell nuclei, the model is formulated within the Relativistic Mean Field Theory (RMFT), while in open shell nuclei we apply the Relativistic Hartree-Bogoliubov (RHB) model which incorporates both the mean field, and the pairing correlations in the self-consistent way. The present RMFT originates from the basic concepts of the Walecka model [12, 14]. The theory is based on the following assumptions: (i) the nucleons are treated as point particles, (ii) relativity is taken into account fully, and (iii) nucleons move as independent particles in the corresponding mean fields. The dynamics of nucleons is described by Dirac equations containing a mass operator including meson fields with different spin, parity and isospin properties. In practical calculations, a very simple combination of fields appeared to be sufficient: one isoscalar field (σ -meson), two vector fields (isoscalar ω -meson and the isovector ρ -meson), plus a photon field. The effective mesons are coupled to the nucleons by local vertices. However, the density dependence appeared to be crucial to achieve quantitative agreement with experiments. In the non-linear relativistic mean field theory, the density dependence is included via non-linear self-interactions between the scalar mesons [13]. Another way is to introduce the density dependence explicitly in the coupling constants [15]. Of course, in non-magic nuclei, pairing correlations play an important role. In particular, close to the drip-lines, one occupies levels in the continuum, leading to unstable solutions of the RMF+BCS equations. This

problem has been avoided in the RHB model with a finite range force of Gogny-type in the pairing channel [16]. Preliminary results including the relativistic pairing field have shown that there is practically no mixing of small and large components of Dirac spinors [17, 18]. If the pairing field for small components is neglected, in first approximation, we may take only the pairing field of the large components. This justifies the use of non-relativistic Gogny force in the pairing channel of the RHB model. Since this force has a finite range, it provides a natural cut-off, i.e. no pairing window is necessary.

Although nucleons in atomic nuclei have relatively small kinetic energies as compared to the rest mass, there are reasons to study the nuclear many body problem in the relativistic framework. It appears that in the relativistic theory the mean fields which determine the motion of nucleons are rather important. In the model including the exchange of Lorentz scalar and vector mesons, two mean fields appear, i.e. an attractive scalar field S and a repulsive vector field V . These two fields approximately cancel one another ($V-S$) for the large components of Dirac spinors, leading to relatively small Fermi momenta and non-relativistic kinematics. For the small components of Dirac equation, however, the two fields add up ($V+S$), leading to a large spin-orbit term in the nuclear field. This indicates that relativistic dynamics is important in the nuclear many body problem even at low energies. In the RMF models, the spin-orbit interaction arises naturally from the Dirac-Lorentz structure of the effective Lagrangian, and there is no need for an additional strength parameter. Proper description of the spin-orbit interaction is very important in exotic nuclei. As the number of neutrons increases, the effective spin-orbit potential and consequent spin-orbit splittings decrease, eventually leading to the effect of shell quenching [19]. Although the RHB model has been very successful in describing many interesting phenomena in exotic nuclei (neutron drip-line, halo phenomena, proton drip-line, skins, etc.) it is not yet clear whether the isospin dependence is properly included in the present models.

The excitation phenomena in exotic nuclei, in particular the giant resonances and the existence of low-energy soft dipole (so called pygmy) resonances have raised significant interest in recent years. Among collective modes of excitations, giant resonances have been one of very active topics in the nuclear physics in last few decades. Their widths, observed in scattering experiments, appear much wider in comparison with typical single-particle interactions, and their energies reflect the underlying collective dynamics of protons and neutrons. Two basic categories of giant resonances are distinguished: electric and magnetic, corresponding respectively to the excitations that do and do not involve the spin degree of freedom. The electric multipole resonances can be excited by a variety of different techniques, especially by inelastic scattering of α particles, proton scattering, etc. On the other side, magnetic giant resonances (e.g. spin dipole resonances) are naturally excited by a relatively restricted set of scattering processes, such as (p, n) . Among the electric multipole resonances, four angular momentum levels have so far been extracted: $L = 0, 1, 2, 3$. They correspond to the monopole (GMR), dipole (GDR), quadrupole (GQR), and octupole (GOR) modes, respectively. As one moves away from the valley of stability, the traditional image of giant resonances is strongly affected. In addition, the appearance of low-energy soft modes, decoupled from the giant resonances, have been detected in dipole and quadrupole channels.

The multipole response of unstable nuclei far from the valley of β -stability presents a very active field of research, both experimentally and theoretically. On the neutron rich side, modification of the effective nuclear potential leads to the formation of nuclei with very diffuse neutron densities, as well as to the occurrence of the neutron skin and halo structures. These phenomena may be reflected in the multipole response of unstable nuclei, and new modes of excitations are expected to arise. In neutron rich nuclei, the neutron orbitals just above the Fermi surface are slightly unbound. Therefore the excitations across the shells close to the Fermi surface may give rise to the low-lying non-collective threshold strength, or to the collective soft modes. The collectivity of the low-lying multipole strength in exotic nuclei is still an open question.

Recently, the first soft dipole resonance has been observed in helium-6, in which α particle and neutrons oscillate in opposite directions [20]. The exotic ground state properties are reflected in the onset of low-energy isovector dipole modes, in a series of experimental studies, from oxygen isotopes [21, 22], towards the medium heavy nuclei (^{56}Fe and ^{58}Ni [23], $^{116,124}\text{Sn}$ [24], ^{138}Ba [25]). A similar effect has also recently been detected in a stable heavy nucleus (^{208}Pb [26]). Most of these investigations have been followed by theoretical calculations within the quasiparticle phonon model.

The multipole response of nuclei with large neutron excess has been the subject of many theoretical studies in recent years. In particular, the giant resonances and the low-lying components of transition strength have been investigated for weakly bound neutron-rich nuclei [27, 33]. It has been shown that the neutron excess increases the fragmentation of the isovector giant dipole resonance (GDR) and that the radial separation of proton and neutron densities leads to non-vanishing isoscalar transition densities to the GDR states. The fragmentation of the isoscalar and isovector monopole strength in neutron rich isotopes has been studied in Ref. [29]. In the case of monopole excitations in the neutron drip-line nuclei, there is a clear evidence for the low-lying neutron non-collective strength in the region 4-12 MeV, far below the giant resonance.

The pygmy dipole resonance, which is also the subject of the present study, results from the excess neutrons oscillating out of phase against a core composed of the rest of the nucleons. A number of theoretical models have been applied to study the dynamics of pygmy dipole resonances. These include: the three-fluid hydrodynamical model (the protons, the neutrons of the same orbitals as protons, and the excess neutrons) [30], the two-fluid (the core fluid and the neutron excess fluid) Steinwedel-Jensen hydrodynamical model [31], density functional theory [32], and the Hartree-Fock plus random phase approximation (RPA) with Skyrme forces [33, 34]. More recently, large scale shell model calculations have been performed in studies of pygmy and dipole states in oxygen isotopes [35], and dipole and spin-dipole strength distributions in ^{11}Li [36].

A quantitative description of ground-states and properties of excited states in open shell nuclei characterized by the closeness of the Fermi surface to the particle continuum, necessitates a unified description of mean-field and pairing correlations, as for example in the framework of the Hartree-Fock-Bogoliubov (HFB) theory. In order to describe transitions to low-lying excited states in weakly bound nuclei, the two-quasiparticle configuration space must include states with both nucleons in the discrete bound levels, states with one nucleon in the bound levels and one nucleon in the continuum, and also states

with both nucleons in the continuum. This cannot be accomplished within the framework of the BCS approximation, since the BCS scheme does not provide a correct description of the scattering of nucleonic pairs from bound states to the positive energy particle continuum. However, the present knowledge of pairing correlations in exotic nuclei is still rather limited. In sophisticated models, one usually adopts for pairing, density dependent contact, or more complicated finite range interactions [1, 37, 38]. The density dependence of pairing interaction is reflected in the spatial properties of the pairing fields, adopting various versions of volume or surface type of pairing.

The low-lying excited states in weakly bound nuclei are best described by the quasiparticle random phase approximation (QRPA) based on the HFB ground state. In Ref. [39] a fully self-consistent QRPA has been formulated in the HFB canonical single-particle basis. The Hartree-Fock-Bogoliubov formalism in coordinate state representation has also been used as a basis for the continuum linear response theory [40, 38]. In Ref. [41] the HFB energy functional has been used to derive the continuum QRPA response function in coordinate space. HFB-based continuum QRPA calculations have been performed for the low-lying excited states and giant resonances, as well as for the β -decay rates in neutron rich nuclei.

In this work we formulate the relativistic quasiparticle random phase approximation (RQRPA) in the canonical single-nucleon basis of the relativistic Hartree-Bogoliubov (RHB) model. The RHB model has recently been applied in description of a variety of nuclear structure phenomena, not only in nuclei along the valley of β -stability, but also in exotic nuclei with extreme isospin values. In particular, in neutron-rich nuclei, RHB framework has been used to describe the halo phenomenon in light nuclei [42], properties of light nuclei [43], and of Ni and Sn isotopes [44] close to the neutron drip-line, the reduction of spin-orbit potential in nuclei with extreme isospin values [45], and deformation and shape coexistence phenomena [45]. On the proton-rich side, RHB model has been used to map the proton drip-line in the region $Z=31-73$, and to study the proton radioactivity [46, 47, 48]. The RQRPA model is an extension of the Relativistic Random Phase Approximation (RRPA) which has recently been employed in quantitative analyzes of collective excitations in finite nuclei [49, 50, 51, 52, 53, 54]. The RRPA model is obtained by taking the small amplitude limit of the Time Dependent Relativistic Mean Field Theory (TDRMFT). Although TDRMFT models have been successfully applied to describe the giant resonances (GMR,GDR,GQR) [55, 56, 57, 58], because of large computational requirements, it is unable to describe the fine structure like the low-lying collective phenomena. Two points are essential for successful application of RRPA to describe dynamical properties of the small amplitude vibrations in finite nuclei: (i) the use of effective Lagrangians with nonlinear self-interaction terms, and (ii) the fully consistent treatment of the Dirac sea of negative energy states.

The RRPA model with nonlinear meson interaction terms, including a configuration space with the states both from the Fermi and Dirac sea, has been successfully employed in studies of nuclear compressional modes [50, 59, 52], multipole giant resonances and of low-lying collective states in spherical nuclei [54], and evolution of the low-lying isovector dipole response in nuclei with a large neutron excess [60, 61]. In the present work, we formulate and apply for the first time the RQRPA model built on top of the canonical

RHB basis, to investigate multipole excitations in the open-shell neutron-rich nuclei [62].

Proper understanding of dipole strength distributions in exotic nuclei is especially important in calculations of the neutron capture cross sections for r-process. Namely, in the statistical model of Hauser-Feshbach, both the level densities and dipole strength distributions are the essential input. However, in the neutron-rich nuclei the existence of the pygmy resonance gives a significant contribution in the low-lying energy region. If this strength is located around the neutron threshold, it can increase the resulting neutron capture cross section by a significant factor in the nuclei close to the drip-line [63].

Among the giant resonances, the compression modes are also of a particular interest, since they are closely connected to the nuclear incompressibility. It is one of the most important quantities in nuclear physics, related to the structure of neutron stars, the dynamics of heavy-ion collisions and of supernovae explosions. Although the nuclear matter incompressibility cannot be measured directly, for low nuclear temperatures, it can be evaluated from the strength distributions of compression modes. Whereas the isoscalar giant monopole resonance (ISGMR) is well established throughout the nuclear chart, in the case of isoscalar dipole giant dipole resonances (ISGDR), theoretical predictions for the excitation energies are not consistent with experimental data. Namely, both the non-relativistic [64] and relativistic [50] models predict a strong separation of the isoscalar dipole strength in two broad structures: the high-energy strength above 20 MeV, and the low-energy peaks between 8 MeV and 14 MeV. Although the spurious center of mass motion has been carefully subtracted, the low-lying region preserved a strong contribution from the non-spurious strength. On the other side, all effective interactions, both the non-relativistic and relativistic, result with excitation energies of ISGDR that are 4 – 5 MeV higher than those obtained from experiment, although they reproduced the experimental excitation energies of the ISGMR reasonably. In Ref. [50] it has been suggested that the low-lying peaks do not correspond to a compression mode, but to another toroidal-type excitation dominated by the surface effects. Following this idea, in the present work we study ISGDR within the RHB+RQRPA model to understand why the dipole compression modes cannot be quantitatively reproduced, although the monopole compression modes in the same model correspond to the experimental data.

The last problem which we address in this work is related to the electron captures and β -decays. Namely, both processes, which played an important role in pre-supernovae phase in the core collapse of a massive star, are determined by the Gamow-Teller and Fermi transitions. In order to gain a proper description of electron captures and β -decays, a reliable description of Gamow-Teller strength distribution in nuclei is crucial [65]. Gamow-Teller strengths in exotic nuclei are of a particular importance for the r-process, since the half-lives of β -decays along r-process path are generally dominated by the tails of the Gamow-Teller resonances. Until recently [66, 67], the charge-changing excitations have not been investigated within the relativistic mean-field framework. Furthermore, in recent investigation, it has been indicated that the antinucleon degrees of freedom actually play an important role in the Gamow-Teller model independent sum rules [68]. These contributions have not so far been included in relativistic RPA models. In this work we formulate the proton-neutron relativistic QRPA to investigate the isospin-flip excitation energies and sum rules in selected nuclei.

This work is organized in the following way. The basic concepts of relativistic mean field model for finite nuclei are briefly presented in Chapter 1. In Chapter 2 we formulate and test the matrix equations of the relativistic quasiparticle random phase approximation (RQRPA) in the canonical basis of the relativistic Hartree-Bogoliubov (RHB) framework for spherical even-even nuclei. We apply the RHB+RQRPA model in Chapter 3 to explore the low-lying transition strength and soft collective modes in a series of neutron rich nuclei along the isotope and isotone chains, in comparison with available non-relativistic calculations and important experiments. In Chapter 4 we study the compression modes in nuclei, i.e. the isoscalar monopole and dipole resonances, as well as possible existence of the low-lying dipole toroidal mode. Chapter 5 contains the basic formalism of the proton-neutron RQRPA, and its applications to the charge-exchange resonances. Finally, we give a summary and conclusion of the present work.

Chapter 1

Basic Concepts of the Relativistic Mean Field Theory

In the present work, we consider the nuclear many body problem within the framework of the covariant density functional theory (DFT), by using the Kohn-Sham approach of minimization of the energy functional to determine the exact ground state of nuclear system. By neglecting the local exchange-correlation potentials, the covariant DFT is an equivalent method to the relativistic mean field theory (RMFT) which describes protons and neutrons as Dirac particles interacting in a relativistic covariant manner through the exchange of virtual mesons [12, 14]. The energy functional that describes the dynamics of nuclear system is derived from an effective Lagrangian. The nucleons are treated as point particles; although they are more complex QCD objects composed from quarks and gluons, it is not yet possible to include their degrees of freedom to obtain a consistent systematic solution of the nuclear many body problem in finite nuclei. The RMFT is based on the assumption that it is a fully Lorentz invariant theory which obeys causality. It is an effective Lagrangian theory which uses the meson masses and their coupling constants to nucleons as effective parameters which are fitted to the bulk properties of the nuclear matter and a few finite nuclei. Once the free parameters are properly adjusted, the model can be used to describe not only the ground-state properties, but also many different types of excitations on a quantitative level.

The meson degrees of freedom are selected according to their relevant quantum properties: parity, spin and isospin. Here we employ a simple $(\sigma, \omega, \rho, \gamma)$ model [14, 69]. The isoscalar-scalar field σ , with the quantum numbers $(J^\pi, T) = (0^+, 0)$, mediates the medium-range attraction between the nucleons. It is an effective field which may have its origin from many more complex effects, for example, from the two-pion resonances, or QCD combinations of quark-antiquark pairs and gluons. The isoscalar-vector field ω $(1^-, 0)$ is included to reproduce the short-range repulsion, while the dependence of the nuclear force on isospin is included by the isovector-vector field ρ $(1^-, 1)$. It is not clear so far, why a scalar field with isospin is not needed in such a description. In principle, we should also include into consideration the pion field $(0^-, 1)$, which is the basic ingredient of the microscopic nuclear force. However, it does not enter on the classical Hartree-level, because it leads to a parity breaking field, which has not been observed in actual nuclei.

On the other side, as we will show in Chapter 5, the pion plays an important role in the relativistic description of unnatural parity excitations, in particular for the spin-flip and Gamow-Teller resonances. Finally, the Coulomb interaction is also taken into account by including the photon field γ , described by the vector potential A_μ .

1.1 Relativistic Lagrangian Density

In the relativistic mean field theory, the dynamics of a nuclear system, i.e. its corresponding fields, $\psi(x)$ for nucleons, $\sigma(x), \omega^\mu(x), \vec{\rho}^\mu(x)$ for mesons and $A^\mu(x)$ for photons, is determined through the Lagrangian density[12],

$$\mathcal{L} = \mathcal{L}_N + \mathcal{L}_m + \mathcal{L}_{int} \quad (1.1)$$

where the first term describes free nucleons with the mass m ,

$$\mathcal{L}_N = \bar{\psi} (i\gamma^\mu \partial_\mu - m) \psi. \quad (1.2)$$

In the present outline, we employ the covariant notation of the four matrices $\gamma^\mu = (\gamma^0, \boldsymbol{\gamma})$,

$$\gamma^0 = \begin{pmatrix} 1 & 0 \\ 0 & -1 \end{pmatrix}, \quad \boldsymbol{\gamma} = \begin{pmatrix} 0 & \boldsymbol{\sigma} \\ -\boldsymbol{\sigma} & 0 \end{pmatrix}, \quad (1.3)$$

where $\boldsymbol{\sigma}$ corresponds to the three component Pauli spin 1/2 matrices. The meson term describes free mesons (σ , ω , and ρ) and photons,

$$\begin{aligned} \mathcal{L}_m = & \frac{1}{2} \partial_\mu \sigma \partial^\mu \sigma - \frac{1}{2} m_\sigma^2 \sigma^2 - \frac{1}{4} \Omega_{\mu\nu} \Omega^{\mu\nu} + \frac{1}{2} m_\omega^2 \omega_\mu \omega^\mu \\ & - \frac{1}{4} \vec{R}_{\mu\nu} \vec{R}^{\mu\nu} + \frac{1}{2} m_\rho^2 \vec{\rho}_\mu \vec{\rho}^\mu - \frac{1}{4} F_{\mu\nu} F^{\mu\nu} \end{aligned} \quad (1.4)$$

where the field tensors for the vector mesons (ω, ρ) and photon fields are defined as

$$\Omega_{\mu\nu} = \partial_\mu \omega_\nu - \partial_\nu \omega_\mu \quad (1.5)$$

$$\vec{R}_{\mu\nu} = \partial_\mu \vec{\rho}_\nu - \partial_\nu \vec{\rho}_\mu \quad (1.6)$$

$$F_{\mu\nu} = \partial_\mu A_\nu - \partial_\nu A_\mu. \quad (1.7)$$

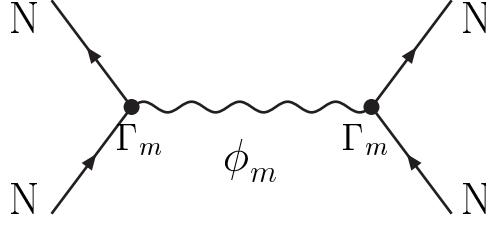
The nucleon-meson interaction is described by the minimal coupling given as a sum

$$\mathcal{L}_{int} = -\bar{\psi} \Gamma_m \phi_m \psi = -\bar{\psi} \Gamma_\sigma \sigma \psi - \bar{\psi} \Gamma_\omega \omega \psi - \bar{\psi} \vec{\Gamma}_\rho \vec{\rho} \psi - \bar{\psi} \Gamma_e A \psi, \quad (1.8)$$

where the index m runs over different mesons ϕ_m and vertices Γ_m , given by

$$\Gamma_\sigma = g_\sigma, \quad \Gamma_\omega^\mu = g_\omega \gamma^\mu, \quad \vec{\Gamma}_\rho^\mu = g_\rho \vec{\tau} \gamma^\mu, \quad \Gamma_e^m = e \frac{1 - \tau_3}{2} \gamma^\mu, \quad (1.9)$$

with the coupling constants g_σ , g_ω , g_ρ and e .



Non-linear versions of the Lagrangian include either non-linear terms in the meson couplings, i.e. the mass term of free mesons is replaced by a non-linear potential, as for instance the self-coupling for the scalar mesons of Boguta and Bodmer [13]

$$\frac{1}{2}m_\sigma^2\sigma^2 \quad \rightarrow \quad U(\sigma) = \frac{1}{2}m_\sigma^2\sigma^2 + \frac{g_2}{3}\sigma^3 + \frac{g_3}{4}\sigma^4 \quad (1.10)$$

or density dependent coupling constants $g_m(\rho)$, where ρ is either the scalar density ρ_s or the Lorentz invariant form $\sqrt{j^u j_\mu}$ of the baryon density, $j_\mu = \bar{\psi}\gamma_\mu\psi$ [15]. In the present investigation the density dependence is included in a phenomenological way by using the non-linear σ potential. The adjustment of the non-linear parameters g_2, g_3 to the surface properties of the finite nuclei gives a negative value for the parameter g_3 , leading to an unstable theory. However, in the limit of moderate densities, as in normal nuclei, the σ fields are small, and the potential $U(\sigma)$ is attractive, resulting in reasonable solutions [16, 13].

The equations of motion for the nucleon and meson fields are derived from the classical variational principle,

$$\delta \int \mathcal{L}(q_i, \partial_\mu q_i) d^4x = 0 \quad (1.11)$$

i.e. by solving the Euler-Lagrange equations for the Lagrangian density (1.1),

$$\partial_\mu \left(\frac{\partial \mathcal{L}}{\partial(\partial_\mu q_i)} \right) - \frac{\partial \mathcal{L}}{\partial q_i} = 0, \quad (1.12)$$

where $q_i = \psi$ corresponds to the nucleon, and $q_i = \sigma, \omega_\mu, \vec{\rho}_\mu$ and A_μ are meson and photon fields, respectively. Accordingly, the nucleons are described by the Dirac equation,

$$[i\gamma^\mu \partial_\mu + m + \Gamma_m \phi_m] \psi = 0, \quad (1.13)$$

leading to the conservation law

$$\partial_\mu j_B^\mu(x) = 0 \quad (1.14)$$

for the baryon density current

$$j_B^\mu(x) = \bar{\psi}(x)\gamma^\mu\psi(x). \quad (1.15)$$

By solving Eq. (1.12) for the meson and photon fields, the Klein-Gordon equations are obtained,

$$[\partial^\mu \partial_\mu + m_m^2] \phi_m = \pm \langle \bar{\psi} \Gamma_m \psi \rangle + \text{nonlinear terms} \quad (1.16)$$

where the upper sign holds for vector fields, the lower sign for scalar fields, and photon mass vanishes ($m_\gamma = 0$).

The sources of the meson fields $\langle \bar{\psi} \Gamma_m \psi \rangle$ are determined by summation over all the occupied orbits in the Slater determinant of the nucleons. In the *no-sea* approximation, the sources of the meson fields are evaluated by using only positive energy spinors. In the full relativistic description, we would also have to include the negative energy states from the Dirac sea. However, this would lead to divergent terms, which can be removed by a proper renormalization in a very complicated way, since the corresponding equations can be solved only numerically [16]. An analytical solution is possible for infinite nuclear matter [70]. In numerical studies of the vacuum polarization in spherical and deformed nuclei, the renormalization effects appeared to be of the order of 20-30%. However, if the vacuum polarization is taken into account, the parameter set of the effective Lagrangian has to be re-adjusted to the experimental data, leading to a new force with approximately the same results as in the case when the vacuum polarization is neglected [71, 72, 73]. Therefore the *no-sea* approximation is used in almost all RMFT practical applications in nuclear matter and finite nuclei.

In the case when the non-linear meson couplings are included, we have to add on the r.h.s. of the Klein-Gordon equation the term $m_m^2 \phi_m - U'$, i.e. for the σ -meson, $-g_2 \sigma^2 - g_3 \sigma^3$. For the density dependence included in the vertex functions g_σ , g_ω and g_ρ , the Klein-Gordon equations are linear, but additional rearrangement terms emerge in the Dirac equation [15]. The set of coupled Dirac (1.13) and Klein-Gordon equations (1.16) represents a consistent description of atomic nuclei, which leads in the static case to a nonlinear eigenvalue problem and in the time-dependent case to a nonlinear propagation of the Dirac spinors in time, i.e. to the time dependent relativistic mean field [55]. However, to obtain the convergent solution in practical calculations, additional approximations are necessary. We will discuss these approximations and the equations of motion for the fields in Section 1.3.

1.2 Covariant Density Functional Theory

In the previous section, the equations of motion for the nucleon and meson fields have been derived explicitly from the Lagrangian density. An alternative approach to the nuclear many body system is possible within the covariant density functional theory, based on the similar concept of widely used density functional theory (DFT) in atomic, molecular and condensed matter physics.

The basic goal of DFT is to describe an interacting system of fermions via its density and not via its many-body wave functions. In particular, for A electrons in a solid, or protons and neutrons in atomic nucleus, which obey the Pauli principle and interact with one another via a Coulomb potential or nuclear forces, the main variable of the system depends only on three spatial coordinates x , y , and z rather than on $3 \cdot A$ degrees of freedom. If we know how to derive necessary relations between density and energy, the DFT calculations would be rather simple and very accurate. Unfortunately, energy functionals that relate density to energy are unknown, and there is no general way to improve them beside trying new ones and judging their quality by the results. In a

molecular DFT, the energy functional is decomposed into three parts; a kinetic energy, a Coulomb energy due to classical electrostatic interactions among all charged particles in the system, and an additional exchange-correlation energy term that includes many-body interactions.

The basic theorems of DFT was first formulated by Hohenberg and Kohn [74]. According to the first theorem, the ground state expectation value of any observable is a unique functional of the exact ground state fermion density $\rho(\mathbf{r})$. This means that if the fermion density and the functional are known, it is possible to calculate all properties of the system, in particular, its ground state energy

$$E = E[\rho]. \quad (1.17)$$

The first Hohenberg-Kohn theorem implies the existence of a total energy functional, but it does not provide the means of solving the many-body problem. This follows from the second Hohenberg-Kohn theorem that provides a variational principle: by a minimization of the energy functional (1.17) with respect to the density we obtain the ground state energy and density of a fermionic system. For any non-negative trial density $\rho(\mathbf{r})$ that gives the correct number of fermions in the system, the true ground state energy E_0 for actual density $\rho_0(\mathbf{r})$ satisfies the relation

$$E_0[\rho_0] \leq E[\rho]. \quad (1.18)$$

The energy term corresponding to the external potential can be extracted from the energy functional,

$$E[\rho] = F[\rho] + \int V_{ext}(\mathbf{r})\rho(\mathbf{r})d\mathbf{r} \quad (1.19)$$

where Kohn and Sham separated $F[\rho]$ in the following way [75],

$$F[\rho] = T[\rho] + E_{int}[\rho] + E_{xc}[\rho]. \quad (1.20)$$

Here $T[\rho]$ corresponds to the kinetic energy of non-interacting fermions, the second term is fermion-fermion interaction, whereas $E_{xc}[\rho]$ contains exchange and correlation terms. Within the Kohn-Sham approach the ground state density of an interacting fermion system is obtained by using the single-particle wave functions from an equivalent system of non-interacting fermions whose dynamics is determined by the appropriate Kohn-Sham external potential [75]. This leads to the set of Kohn-Sham equations for independent fermions in an effective potential,

$$\left[-\frac{\hbar^2}{2m}\nabla^2 + V_{eff}(\mathbf{r}) \right] \psi_i(\mathbf{r}) = \epsilon_i \psi_i(\mathbf{r}). \quad (1.21)$$

This method provide a convenient theoretical tool to determine the ground state energy of an interacting system, assuming that the form of E_{xc} is known. However, this is usually not the case, and additional approximations for E_{xc} are needed. In fact, the Hohenberger-Kohn approach for atomic nuclei would lead to the extended Thomas-Fermi

solution without shell effects. They have to be included in a more complicated way via the Kohn-Sham energy functional of nonlocal density,

$$E[\rho] = E[\rho(\mathbf{r}, \mathbf{r}')] \quad (1.22)$$

which necessitates additional approximations. In the non-relativistic DFT for nuclear systems [32], it is assumed that the energy is a functional of proton and neutron densities,

$$E[\rho] = E_k[\rho] + E_c[\rho] + E_n[\rho] + E_\nabla[\rho] \quad (1.23)$$

where E_k corresponds to the free kinetic energy term of noninteracting nucleons, while E_c denotes the Coulomb interaction. The effects of the strong nuclear force can be represented within the local density approximation by the energy of infinite nuclear matter E_{NM}

$$E_n[\rho] = \int d\mathbf{r} \rho(\mathbf{r}) E_{NM}(\rho(\mathbf{r})), \quad (1.24)$$

where the energy per nucleon of infinite nuclear matter parameterized by Brueckner et al. [76] reads,

$$E_{NM}(\rho) = \sum_{i=1}^3 b_i (1 + a_i \alpha^2) \rho^{n_i}. \quad (1.25)$$

The set of parameters n_i , a_i , and b_i , ($i = 1, 2, 3$) obtained by the fitting to the equation of state is given in Ref. [32], while $\alpha = (\rho_p - \rho_n)/(\rho_p + \rho_n)$ is the asymmetry parameter. In local density approximation, corrections to the exchange-correlation energy due to the inhomogeneities in the density $\rho(\mathbf{r})$ around \mathbf{r} are ignored. However, in the case of the density functional $E = E_k + E_c + E_n$, the nuclei are found severely over bound and contracted. Therefore, an additional correction for the inhomogeneities in a finite nucleus, $E_\nabla[\rho]$ in the gradient form has been introduced [76]. In practical calculations parameters related to the gradient correction are fitted to reproduce the experimental binding energies in each nucleus under consideration [32].

In the following we illustrate that the covariant density functional theory is closely related to the relativistic mean field approach. This gives an alternative way to derive equations of motion of relativistic mean field theory from a density functional. Starting from the energy-momentum tensor of the system described by the Lagrangian density \mathcal{L} ,

$$T^{\mu\nu} = -g^{\mu\nu} \mathcal{L} + \frac{\partial q_i}{\partial x_\nu} \frac{\mathcal{L}}{\partial(\frac{\partial q_i}{\partial x^\nu})} \quad (1.26)$$

which obeys the continuity law $\partial_\mu T^{\mu\nu} = 0$, the four-momentum can be expressed as,

$$P^\mu = \int d^3x T^{0\mu}. \quad (1.27)$$

The Hamiltonian density can be derived from the Lagrangian density,

$$\mathcal{H} = T^{00} = \frac{\partial \mathcal{L}}{\partial \dot{q}_j} \dot{q}_j - \mathcal{L} \quad (1.28)$$

leading to the energy functional,

$$E = \int d^3r \mathcal{H}. \quad (1.29)$$

Resulting energy corresponding to the relativistic Lagrangian is

$$\begin{aligned} E_{RMF}[\hat{\rho}, \phi] &= Tr [(\boldsymbol{\alpha}\mathbf{p} + \beta m)\hat{\rho}] \\ &\pm \frac{1}{2} \int d^3r \left[\dot{\phi}_m^2 + (\nabla\phi_m)^2 + m_m^2\phi_m^2 \right] + E_{NL}[\phi] \\ &+ Tr [(\Gamma_m\phi_m)\hat{\rho}] \end{aligned} \quad (1.30)$$

where the trace operation Tr involves a sum over the Dirac indices and an integral in coordinate space. The plus sign refers to scalar and the minus sign to vector mesons, while the term

$$E_{NL} = \int \left(\frac{g_2}{3}\sigma^3 + \frac{g_3}{4}\sigma^4 \right) d^3r \quad (1.31)$$

contains the contributions of the non-linear meson couplings. E_{RMF} is a functional of the relativistic single particle density matrix

$$\hat{\rho}(\mathbf{r}, \mathbf{r}', t) = \sum_{i=1}^A |\psi_i(\mathbf{r}, t)\rangle \langle \psi_i(\mathbf{r}', t)|, \quad (1.32)$$

and of the meson fields ϕ_m . In the rotational invariant system, the Dirac spinor is composed from the large (upper) and small (lower) components,

$$|\psi_i(\mathbf{r}, t)\rangle = \begin{pmatrix} f_i(\mathbf{r}, t) \\ ig_i(\mathbf{r}, t) \end{pmatrix}, \quad (1.33)$$

leading to the density matrix in terms of the spinor components,

$$\rho(\mathbf{r}, \mathbf{r}', t) = \begin{pmatrix} \sum_{i=1}^A f_i(\mathbf{r}, t) f_i^\dagger(\mathbf{r}', t) & -i \sum_{i=1}^A f_i(\mathbf{r}, t) g_i^\dagger(\mathbf{r}', t) \\ i \sum_{i=1}^A g_i(\mathbf{r}, t) f_i^\dagger(\mathbf{r}', t) & \sum_{i=1}^A g_i(\mathbf{r}, t) g_i^\dagger(\mathbf{r}', t) \end{pmatrix}. \quad (1.34)$$

In particular case, for the $(\sigma, \omega, \rho, \gamma)$ model, the energy functional reads,

$$\begin{aligned} E_{RMF}[\psi, \bar{\psi}, \sigma, \omega^\mu, \vec{\rho}^\mu, A^\mu] &= \sum_{i=1}^A \int \psi_i^\dagger (\boldsymbol{\alpha}\mathbf{p} + \beta m) \psi_i \\ &+ \int \left[\frac{1}{2} (\nabla\sigma)^2 + U(\sigma) \right] d^3r - \frac{1}{2} \int [(\nabla\omega)^2 + m_\omega^2\omega^2] d^3r \\ &- \frac{1}{2} \int [(\nabla\rho)^2 + m_\rho^2\rho^2] d^3r - \frac{1}{2} \int (\nabla A)^2 d^3r \\ &+ \int \left[g_\sigma \rho_s \sigma + g_\omega j_\mu \omega^\mu + g_\rho \vec{j}_\mu \vec{\rho}^\mu + e j_{c\mu} A^\mu \right] d^3r. \end{aligned} \quad (1.35)$$

In the following we apply the classical time-dependent variational principle,

$$\delta \int_{t_1}^{t_2} dt \{ \langle \Phi | i\partial_t | \Phi \rangle - E[\hat{\rho}, \phi] \} = 0 \quad (1.36)$$

where $|\Phi\rangle$ is the Slater determinant of all spinors in the Fermi sea. As a result, this leads to the equations of motion (1.13) and (1.16), that can be expressed in the variables $\hat{\rho}$ and ϕ_m ,

$$i\partial_t \hat{\rho} = \left[\hat{h}(\phi), \hat{\rho} \right] \quad (1.37)$$

$$[\partial^\mu \partial_\mu + m_m^2] \phi_m = \pm Tr[\Gamma_m \hat{\rho}] + \text{nonlinear terms} \quad (1.38)$$

Due to large masses corresponding to the meson fields, leading to the short range of interaction, we neglect the retardation effects, i.e. the second derivatives in time. The single particle Hamiltonian is the functional derivative of the energy with respect to the single particle density matrix $\hat{\rho}$,

$$\hat{h} = \frac{\delta E}{\delta \hat{\rho}} = Tr[\boldsymbol{\alpha} \mathbf{p} + \beta m] + Tr[\Gamma_m \phi_m]. \quad (1.39)$$

A covariant DFT method including extensions beyond the mean field, has been recently considered for its use in the ground state calculations [77]. The energy functional within this theory includes, in addition to the E_{RMF} , an exchange-correlation energy in the limit of the local density approximation (LDA). In this approximation the density dependence of the exchange correlation energy of infinite nuclear matter is adopted to the actual inhomogeneous nuclei. Recent studies of super heavy nuclei within the relativistic DFT indicated that the implementation of the exchange correlations with LDA in the linear ($\sigma - \omega$) model has a similar effect as the inclusion of nonlinear meson self-interaction terms on the relativistic mean field level [77]. Since the role of exchange correlations is partially equivalent to the nonlinear meson contributions, this supports the interpretation of the meson self-interaction as a parameterization of many-body effects, justifying applications of the mean-field models with nonlinear σ -meson self-couplings.

1.3 Equations of Motion in the Relativistic Mean Field Approximation

The RMFT is a classical theory, which corresponds to the mean field approximation. It is based on the assumption that the meson fields can be replaced by their expectation values as classical fields, i.e. the quantum fluctuations of the the meson fields are neglected. This reduces the relativistic nuclear many body problem to the simple picture of independent nucleons moving in the self-consistent mesonic mean fields. In particular, for the ($\sigma, \omega, \rho, \gamma$) model, the time-dependent Dirac equation for the nucleon (1.13) reduces to

$$[\gamma^\mu (i\partial_\mu + V_\mu(\mathbf{r}, t)) + m - S(\mathbf{r}, t)] \psi(\mathbf{r}, t) = 0, \quad (1.40)$$

with two potentials: (i) the Lorentz scalar potential,

$$S(\mathbf{r}, t) = -g_\sigma \sigma(\mathbf{r}, t), \quad (1.41)$$

which determines the effective mass of nucleon,

$$m^*(\mathbf{r}) = m - S(\mathbf{r}), \quad (1.42)$$

and (ii) the vector potential,

$$V_\mu(\mathbf{r}, t) = g_\omega \omega_\mu(\mathbf{r}, t) + g_\rho \vec{\tau} \vec{\rho}_\mu(\mathbf{r}, t) + e A_\mu(\mathbf{r}, t) \frac{(1 - \tau_3)}{2}. \quad (1.43)$$

The time-dependent mean-field potentials (1.41) and (1.43) are evaluated in a self-consistent way from solutions of the stationary Klein-Gordon equations (1.16) at each time,

$$(-\Delta + m_\sigma)\sigma = -g_\sigma \rho_s - g_2 \sigma^2 - g_3 \sigma^3, \quad (1.44)$$

$$(-\Delta + m_\omega)\omega^\mu = g_\omega j^\mu, \quad (1.45)$$

$$(-\Delta + m_\rho)\vec{\rho}^\mu = g_\rho \vec{j}^\mu, \quad (1.46)$$

$$-\Delta A^\mu = e j_c^\mu. \quad (1.47)$$

The densities and currents in the Klein-Gordon equations are defined in the following way; the scalar density

$$\rho_s(x) = \sum_i^A \bar{\psi}_i(x) \psi_i(x), \quad (1.48)$$

the baryon current

$$j^\mu(x) = \sum_i^A \bar{\psi}_i(x) \gamma^\mu \psi_i(x), \quad (1.49)$$

the isovector current

$$\vec{j}^\mu(x) = \sum_i^A \bar{\psi}_i(x) \gamma^\mu \vec{\tau} \psi_i(x), \quad (1.50)$$

and the electromagnetic current

$$\vec{j}_c^\mu(x) = \sum_i^A \bar{\psi}_i(x) \frac{1}{2} (1 + \tau_3) \gamma^\mu \psi_i(x). \quad (1.51)$$

The densities and currents (1.48)-(1.51) are evaluated in the *no-sea* approximation, i.e. summation is performed only over occupied orbits in the Fermi sea.

The set of coupled equations (1.40) and (1.44)-(1.51) define the full time-dependent relativistic mean field (TDRMF) model describing the nonlinear propagation of Dirac spinors in time [55]. The small amplitude limit of the TDRMF model corresponds to the relativistic random phase approximation [52, 54].

In order to describe the ground state properties of nuclei, we take the static limit of the TDRMF equations of motion. Since the ground state of even-even nuclei is even under

the time-reversal and has a good parity, the space-like components of the vector fields and currents vanish. Furthermore, since the nucleon single-particle states do not mix isospin, only the third component of the rho-meson field remains. The stationary RMF equations read,

$$\{-i\boldsymbol{\alpha}\boldsymbol{\nabla} + \beta(m - S) + V\}\psi_i = \varepsilon_i\psi_i, \quad (1.52)$$

$$\{-\Delta + m_\sigma\}\sigma = -g_\sigma\rho_s - g_2\sigma^2 - g_3\sigma^3, \quad (1.53)$$

$$\{-\Delta + m_\omega\}\omega^0 = g_\omega\rho_v, \quad (1.54)$$

$$\{-\Delta + m_\rho\}\rho_3^0 = g_\rho\rho_3, \quad (1.55)$$

$$-\Delta\rho_c^0 = e\rho_c, \quad (1.56)$$

where ρ_s correspond to the scalar density,

$$\rho_s = \sum_i^A \bar{\psi}_i\psi_i, \quad (1.57)$$

whereas ρ_v is the baryon density

$$\rho_v = \sum_i^A \psi_i^\dagger\psi_i, \quad (1.58)$$

ρ_3 is the isovector density

$$\rho_3 = \sum_i^A \psi_i^\dagger\tau_3\psi_i, \quad (1.59)$$

and the charge density ρ_c

$$\rho_c = \sum_i^A \psi_i^\dagger\frac{1}{2}(1 + \tau_3)\psi_i, \quad (1.60)$$

The stationary fields from the Dirac equation (1.52) read,

$$V(\mathbf{r}) = g_\omega\omega^0(\mathbf{r}) + g_\rho\tau_3\rho_3^0(\mathbf{r}) + eA^0(\mathbf{r}), \quad (1.61)$$

for the vector field, and

$$S(\mathbf{r}) = -g_\sigma\sigma(\mathbf{r}) \quad (1.62)$$

for the scalar field, contributing to the effective Dirac mass as in Eq. (1.42). The set of equations (1.52)-(1.62) defines the static relativistic mean field (RMF) model. Starting from the initial scalar (1.62) and vector (1.61) fields, we solve the Dirac equations (1.52). By using solutions for ψ_i , we determine the densities (1.57)-(1.60), which are used to evaluate new meson fields from Klein-Gordon equations (1.53)-(1.56), as well as a new set of V, S fields. This procedure is repeated for several times, until a satisfied convergence is obtained.

There are eight free parameters in the present RMF model: meson masses m_σ , m_ω , m_ρ , and their coupling constants g_σ , g_2 , g_3 , g_ω , and g_ρ . The mass of the ρ meson is fixed to the experimental value, i.e.

$$m_\rho = 763.0\text{MeV}, \quad (1.63)$$

while for the proton and neutron nuclear masses we take the average value of empirical proton and neutron masses,

$$m = 938.0 \text{ MeV} \quad \text{or} \quad m = 939.0 \text{ MeV}. \quad (1.64)$$

This reduces the number of free parameters of RMF model to seven parameters which are

	NL1	NL-SH	NL3
m [MeV]	938.0	939.0	939.0
m_σ [MeV]	492.25	526.059	508.194
m_ω [MeV]	795.359	783.0	782.501
g_σ	10.138	10.444	10.217
g_ω	13.285	12.945	12.868
g_ρ	4.976	4.383	4.474
g_2 [fm $^{-1}$]	-12.172	-6.9099	-10.431
g_3	-36.265	-15.8337	-28.885
K_{nm} [MeV]	211.7	355.0	271.8

Table 1.1: RMF parameterizations NL1, NL-SH and NL3. K_{nm} corresponds to the incompressibility of the nuclear matter for each set of parameters.

fitted to measured ground state properties, mainly to the charge and neutron radii and the binding energies of several spherical nuclei. In the present investigation, we use three effective interactions; NL1 [78], NL-SH [79], and NL3 [80], which are given in Table 1.1. In particular, NL3 parameterization has been used very extensively to study the nuclear structure phenomena from light nuclei toward super-heavy elements, both in stable nuclei, and in nuclei away from the valley of stability. In order to obtain NL3 parameter set, the RMF model has been fitted not only to the ground state properties of stable nuclei, but also of ^{132}Sn and ^{214}Pb to obtain an improved isospin dependence of the effective interaction for unstable nuclei [80].

Another alternative to the model based on effective Lagrangian with non-linear sigma meson self-interaction, is RMF theory where the density dependence is explicitly included in the coupling constants for the meson-nucleon vertices. Recently, it has been shown that new density dependent interactions provide an improved description of asymmetric nuclear matter, neutron matter and nuclei far from stability [15].

Although it seems that many effects, which go beyond the mean field, are neglected in the RMF model, such as Fock-terms and vacuum polarization, they are implicitly included in the present RMF model. Since the coupling constants are adjusted to the actual experimental data, these, and many other effects are taken into account in an effective way.

1.4 Relativistic Hartree-Bogoliubov theory

In nuclei with open shells, the RMF picture of independent nucleons moving in an average potential is no longer a sufficient description. The nuclear pairing correlations between

the particles from open shells play an important role in various single-particle and collective aspects of nuclear structure. In general, the pairing correlations are accounted for in the quasiparticle picture by introducing an additional field, i.e. the pairing potential. They cannot be included in the classical Lagrangian, because at the classical level this Lagrangian does not contain Cooper pairs $\psi^+\psi^+$. In order to include pairing correlations in a microscopic way, the meson fields have to be quantized, such that one obtains one-meson-exchange two-body forces, which can be treated by the well known Gorkov factorization. In this way one ends up with relativistic Hartree-Bogoliubov theory [81]. It has been shown however, that the pairing correlations derived in this way with the same parameter set used in the ph -channel are unrealistically high, and that one needs different forces in the pairing channel. In fact, since we are using an effective theory, there is no reason to use the same force in the ph - as in the pp -channel.

The generalized density matrix associated with a quasiparticle vacuum $|\Phi\rangle$ was introduced by Valatin [82] in the following way,

$$\mathcal{R} = \begin{pmatrix} \rho & \kappa \\ -\kappa^* & 1 - \rho^* \end{pmatrix}, \quad (1.65)$$

where ρ is the single-particle density, and κ is pair density, defined respectively as

$$\rho_{ij} = \langle \Phi | c_i^+ c_j | \Phi \rangle \quad (1.66)$$

$$\kappa_{ij} = \langle \Phi | c_i c_j | \Phi \rangle. \quad (1.67)$$

The ground state of a nucleus, $|\Phi\rangle$ can be represented as a vacuum with respect to the independent quasiparticle operators

$$\alpha_k^+ = \sum_{m>0} U_{mk} c_m^+ + V_{mk} c_m \quad (1.68)$$

$$\alpha_k |\Phi\rangle = 0 \quad (1.69)$$

where U_{mk}, V_{mk} are the Hartree-Bogoliubov coefficients. The operators α_k, α_k^+ obey the usual anti-commutation relations for fermions,

$$\{\alpha_k, \alpha_{k'}\} = \{\alpha_k^+, \alpha_{k'}^+\} = 0 \quad (1.70)$$

$$\{\alpha_k, \alpha_{k'}^+\} = \delta_{kk'}. \quad (1.71)$$

The coefficients U_{mk}, V_{mk} determine the single particle density matrix

$$\hat{\rho}_{ab}(\mathbf{r}, \mathbf{r}') = \sum_{k>0} V_{ak}^*(\mathbf{r}) V_{bk}(\mathbf{r}'), \quad (1.72)$$

and the pairing tensor

$$\kappa_{cd}(\mathbf{r}, \mathbf{r}') = \sum_{k>0} U_{ck}^*(\mathbf{r}) V_{dk}(\mathbf{r}'). \quad (1.73)$$

i	$\mu_i [fm]$	W_i	B_i	H_i	$M_i [MeV]$
1	0.7	-1720.3	1300.0	-1813.53	1397.60
2	1.2	103.69	-163.483	162.812	-223.934

Table 1.2: Parameter set D1S for the pairing part of the effective Gogny interaction.

where the indices a, b, c, d are Dirac indices, and $\sum_{k>0}$ is a shorthand notation for the *no-sea* approximation. In DFT approach with pairing correlations, the energy functional depends not only on the density matrix and the meson fields ϕ_m , but in addition on the pairing tensor. It has the form

$$E[\hat{\rho}, \hat{\kappa}, \phi] = E_{RMF}[\hat{\rho}, \phi] + E_{pair}[\hat{\kappa}], \quad (1.74)$$

where $E_{RMF}[\hat{\rho}, \phi]$ is the *RMF*-functional defined in Eq. (1.30), only the density $\hat{\rho}$ of Eq. (1.32) is replaced by the density (1.72). The pairing energy $E_{pair}[\hat{\kappa}]$ is given by

$$E_{pair}[\hat{\kappa}] = \frac{1}{4} Tr [\hat{\kappa}^* V^{pp} \hat{\kappa}]. \quad (1.75)$$

The effective pairing force V^{pp} is the phenomenological *pp*-interaction in the pairing channel.

The simplest possibility to take for V^{pp} would be a monopole pairing force, leading to the BCS theory. It requires an additional energy cut-off, which is not very well known from experiment. The pairing correlations for nuclei in the valley of the β -stability have been in many cases included in the RMFT by the BCS approximation [83]. As we move away from the stable nuclei towards the drip-lines, the Fermi level becomes close to the particle continuum and the lowest particle-hole or particle-particle modes are often embedded in the continuum. In that case, the BCS approximation does not provide a correct description for the scattering of nucleonic pairs from bound states to the positive energy continuum [7]. In the present relativistic Hartree-Bogoliubov model, following Ref. [37], we use a realistic description of volume-type finite range pairing interaction. One appropriate selection would be the pairing part of the Gogny force [84],

$$V^{pp}(1, 2) = \sum_{i=1,2} e^{-(\mathbf{r}_1 - \mathbf{r}_2)/\mu_i} (W_i + B_i P^\sigma - H_i P^\tau - M_i P^\sigma P^\tau). \quad (1.76)$$

The set of free parameters μ_i , W_i , B_i , H_i and M_i ($i = 1, 2$) has in the past been very carefully adjusted to the pairing properties of finite nuclei over the whole periodic table. In the present work, we use the standard parameterization D1S [84], which is listed in the Table 1.2. The same interaction will also be included in the pairing channel of the relativistic quasiparticle RPA residual interaction. More details about the two-body matrix elements for the pairing part of the Gogny force are given in Appendix B.

The total energy $E[\hat{\rho}, \hat{\kappa}, \phi] = E[\mathcal{R}, \phi]$ depends on the generalized density matrix, that obeys the time-dependent Hartree-Bogoliubov equations

$$i\partial_t \mathcal{R} = [\mathcal{H}(\mathcal{R}), \mathcal{R}] \quad (1.77)$$

that are actually an extension of Eq. (1.36) after we have included the pairing correlations. \mathcal{H} is the generalized single-particle field, i.e. the Hartree-Bogoliubov Hamiltonian

$$\mathcal{H} = \frac{\delta E}{\delta \mathcal{R}} = \begin{pmatrix} \hat{h}_D - m - \lambda & \hat{\Delta} \\ -\hat{\Delta}^* & -\hat{h}_D + m + \lambda \end{pmatrix}. \quad (1.78)$$

RHB Hamiltonian contains two average potentials: the self-consistent mean field \hat{h}_D , which encloses all the long range particle-hole (ph) correlations, and the pairing field $\hat{\Delta}$, which includes the particle-particle (pp) correlations; m is the nucleon mass. The single particle potential \hat{h}_D results from the variation of the energy functional with respect to the hermitian density matrix $\hat{\rho}$

$$\hat{h}_D = \frac{\delta E}{\delta \hat{\rho}} = \boldsymbol{\alpha}(\mathbf{p} + \mathbf{V}) + V + \beta(m - S). \quad (1.79)$$

where scalar field S and vector field (V, \mathbf{V}) are defined in (1.41) and (1.43), respectively. In addition, the RHB Hamiltonian contains the pairing field

$$\Delta = \frac{\delta E}{\delta \hat{\kappa}} \quad (1.80)$$

or in detail

$$\Delta_{ab}(\mathbf{r}, \mathbf{r}') = \frac{1}{2} \sum_{c,d} V_{abcd}^{pp}(\mathbf{r}, \mathbf{r}') \kappa_{cd}(\mathbf{r}, \mathbf{r}'), \quad (1.81)$$

where a, b, c, d denote quantum numbers that specify the Dirac indices of the spinors, $V_{abcd}^{pp}(\mathbf{r}, \mathbf{r}')$ are matrix elements of a general two-body pairing interaction.

In the RHB approach [37, 43] the ground state of an open-shell nucleus $|\Phi\rangle$ is obtained in the static limit of Eq. (1.77). It is determined by the Hartree-Bogoliubov equations

$$\begin{pmatrix} \hat{h}_D - m - \lambda & \hat{\Delta} \\ -\hat{\Delta}^* & -\hat{h}_D + m + \lambda \end{pmatrix} \begin{pmatrix} U_k(\mathbf{r}) \\ V_k(\mathbf{r}) \end{pmatrix} = E_k \begin{pmatrix} U_k(\mathbf{r}) \\ V_k(\mathbf{r}) \end{pmatrix}. \quad (1.82)$$

The energy scale is selected in such a way, that the positive energy continuum starts at zero energy. The chemical potential λ is determined from the condition that the expectation value of the particle number operator in the ground state equals the number of nucleons.

The eigenvalues E_k are the quasiparticle energies and the eigenvectors are the Hartree-Bogoliubov coefficients U_k and V_k that form the RHB spinor,

$$\Phi_k(\mathbf{r}) = \begin{pmatrix} U_k(\mathbf{r}) \\ V_k(\mathbf{r}) \end{pmatrix}. \quad (1.83)$$

In the case of spherical symmetry the Dirac spinors U_k and V_k reduce to,

$$U_k(V_k)(\mathbf{r}, s, t_3) = \begin{pmatrix} g_{U(V)}(r) \Omega_{j,l,m}(\theta, \varphi, s) \\ i f_{U(V)}(r) \Omega_{j,\tilde{l},m}(\theta, \varphi, s) \end{pmatrix} \chi_\tau(t_3). \quad (1.84)$$

where $g(r)$ and $f(r)$ are radial amplitudes, and χ_τ is the isospin function. The orbital angular momenta l and \tilde{l} are determined by the corresponding j and the parity π in the following way:

$$l = \begin{cases} j + 1/2 & \text{for } \pi = (-1)^{j+1/2} \\ j - 1/2 & \text{for } \pi = (-1)^{j-1/2} \end{cases}, \quad (1.85)$$

and

$$\tilde{l} = \begin{cases} j - 1/2 & \text{for } \pi = (-1)^{j+1/2} \\ j + 1/2 & \text{for } \pi = (-1)^{j-1/2} \end{cases} \quad (1.86)$$

Finally, the term Ω_{jlm} is the tensor product of the orbital and spin functions, i.e.

$$\Omega_{j,l,m}(\theta, \varphi, s) = \sum_{m_s, m_l} \langle \frac{1}{2} m_s l m_l | j m \rangle \chi_{\frac{1}{2} m_s} Y_{l m_l}(\theta, \varphi). \quad (1.87)$$

We find twice as many eigenstates as the dimension of the Dirac equation, but for the ground state only positive quasiparticle energies are chosen. The densities $\hat{\rho}$ and the pairing tensor $\hat{\kappa}$ are calculated from these coefficients in Eqs. (1.72) and (1.73). The sum $\sum_{k>0}$ in these equations is a shorthand notation for the *no-sea* approximation. In a case without pairing, the *no-sea* approximation is well defined, as the Dirac Hamiltonian is diagonal. The eigenvalues ε_i are the single particle energies and we have a gap in the Dirac spectrum. The sum then runs over all the states above the Dirac gap, i.e. over all the states with $\varepsilon_i > -m$. In the case with pairing, the quasiparticle energies E_k are positive by definition because, from each pair $(E_k, -E_k)$ of eigenvalues of the HB-equations (1.82), we choose only the positive value (for details see [85]). The *no-sea* approximation means, in this case, that the sum runs over all the eigenvalues E_k of the Hartree-Bogoliubov matrix (1.82) below the Dirac gap. In fact the quasiparticle spectrum starts with positive values, which correspond to the lowest quasiparticle states, i.e. states just above or below the Fermi level. With increasing energy we find all the states of the Fermi sea and the states above the Fermi level. The first quasiparticle states belonging to the Dirac sea have a quasiparticle energy of the Dirac gap. Above that we have states of the Dirac sea and states very high up in the positive energy continuum. However, those states are not occupied and they do not contribute to the densities.

Since the quasiparticle wave functions in the Hartree-Bogoliubov equations (1.82) contain both the large and small components, the pairing field $\hat{\Delta}$ can be written as,

$$\begin{pmatrix} \hat{\Delta}_{++} & \hat{\Delta}_{+-} \\ \hat{\Delta}_{-+} & \hat{\Delta}_{--} \end{pmatrix}. \quad (1.88)$$

By using relativistic potentials with cut-off parameters, recent calculations of finite nuclei [86] have shown that the matrix elements of the terms $\hat{\Delta}_{-+}$ and $\hat{\Delta}_{+-}$, which couple large and small components, are orders of magnitude smaller than the matrix elements of the corresponding off-diagonal term $\boldsymbol{\sigma} \cdot \boldsymbol{\nabla}$ of the Dirac Hamiltonian h_D . Since the pairing properties are determined by correlations in an energy window of a few MeV around the Fermi surface, $\hat{\Delta}_{--}$ has no effect on pairing in finite nuclei. Therefore we neglect the fields $\hat{\Delta}_{-+}$, $\hat{\Delta}_{+-}$ and $\hat{\Delta}_{--}$ in the RHB equations, and use a non-relativistic Gogny force (1.76) in the calculation of the field $\hat{\Delta}_{++}$.

The RHB equations are solved self-consistently, with potentials determined in the mean-field approximation from solutions of static Klein-Gordon equations (1.53)-(1.56). The equation for the isoscalar scalar σ -meson field contains nonlinear terms. The inclusion of nonlinear meson self-interaction terms in meson-exchange RMF models is absolutely necessary for a quantitative description of ground-state properties of spherical and deformed nuclei [16]. The source terms in equations (1.53) to (1.56) are now sums of bilinear products of baryon amplitudes

$$\rho_s(\mathbf{r}) = \sum_{k>0} V_k^\dagger(\mathbf{r})\gamma^0 V_k(\mathbf{r}), \quad (1.89)$$

$$\rho_v(\mathbf{r}) = \sum_{k>0} V_k^\dagger(\mathbf{r})V_k(\mathbf{r}), \quad (1.90)$$

$$\rho_3(\mathbf{r}) = \sum_{k>0} V_k^\dagger(\mathbf{r})\tau_3 V_k(\mathbf{r}), \quad (1.91)$$

$$\rho_{em}(\mathbf{r}) = \sum_{k>0} V_k^\dagger(\mathbf{r})\frac{1-\tau_3}{2}V_k(\mathbf{r}), \quad (1.92)$$

The eigen-solutions of Eq. (1.82) form a set of orthonormal single quasiparticle states. In the particular implementation of the RHB model that we use in this work, the Dirac-Hartree-Bogoliubov integro-differential eigenvalue equations and Klein-Gordon equations for the meson fields are solved by expanding the nucleon spinors $U_k(\mathbf{r})$ and $V_k(\mathbf{r})$, and the meson fields in a basis of eigenfunctions of a spherical harmonic oscillator [83].

Chapter 2

Relativistic Quasiparticle Random Phase Approximation

In this chapter we derive the matrix equations of the relativistic quasiparticle random phase approximation (RQRPA) in order to describe nuclear excitations based on a two-quasiparticle configuration space. The excitations are built on the ground state formulated in the canonical basis of the relativistic Hartree-Bogoliubov model (RHB) for even-even nuclei, assuming spherical symmetry. The RQRPA approach includes only the small-amplitude oscillations around the ground state density.

2.1 Matrix Equations of Relativistic Quasi-Particle RPA

In the following, we derive the RQRPA equations from the time-dependent RHB model in the limit of small amplitude oscillations. We have considered only the ground state to date, which is described by the static solution of the RMF equations characterized by the generalized density \mathcal{R}_i and the fields $\phi_m^{(0)}$. In the next step we turn to small oscillations around this self-consistent ground state solution. So far we have used \mathcal{R} and ϕ_m as independent variables, connected only by the equations of motion. Since we want to describe the small oscillations self-consistently, we now eliminate the mesonic degrees of freedom using the Klein-Gordon equations. Then the generalized Hamiltonian \mathcal{H} depends only on the fermionic degrees of freedom, i.e. it can be expressed as a functional of the generalized density \mathcal{R} only. This elimination is possible only because we are working in the limit of small amplitudes. In this case the meson field can be written as

$$\phi_m = \phi_m^{(0)} + \delta\phi_m. \quad (2.1)$$

$\delta\phi_m$ is obtained from the linearized Klein-Gordon equations. Neglecting retardation effects, i.e. neglecting $\partial_t^2 \phi_m$ we find

$$\left[-\Delta + U''(\phi_m^{(0)}) \right] \delta\phi_m(\mathbf{r}) = \pm g_m \delta\rho_m(\mathbf{r}) \quad (2.2)$$

where $\rho_m(\mathbf{r})$ are the various densities and currents given in Eq. (1.89). In the case of linear meson couplings $U'' = m_m^2$ does not depend on $\phi_m^{(0)}(\mathbf{r})$ and therefore the propagator $G_m(\mathbf{r}, \mathbf{r}')$ can be obtained analytically. It is of Yukawa form. We find a linear connection between $\delta\phi_m$ and $\delta\hat{\rho}$,

$$\delta\phi_m(\mathbf{r}) = \pm g_m \int d^3r' G_m(\mathbf{r}, \mathbf{r}') \delta\rho_m(\mathbf{r}') \quad (2.3)$$

For non-linear meson couplings the propagator has to be calculated numerically (for details see Ref. [53]).

From now on we are left with the fermionic degrees of freedom only and therefore we have to consider only the generalized density \mathcal{R} . In the small amplitude limit we expand

$$\mathcal{R}(t) = \mathcal{R}_0 + \delta\mathcal{R}(t) \quad (2.4)$$

where \mathcal{R}_0 is the stationary ground state generalized density, while

$$\delta\mathcal{R}(t) = \sum_{\nu} \delta\mathcal{R}^{(\nu)} e^{i\Omega_{\nu}t} + h.c. \quad (2.5)$$

describes a small variation around the ground state, where ω_{ν} are the frequencies of the different eigen modes. They are admixed with the amplitudes $\delta\mathcal{R}^{(\nu)}$. Since $\mathcal{R}(t)$ is a projector at all times, in linear order

$$\mathcal{R}_0\delta\mathcal{R} + \delta\mathcal{R}\mathcal{R}_0 = \delta\mathcal{R}. \quad (2.6)$$

In the quasiparticle basis the matrices \mathcal{R}_0 and $\mathcal{H}_0 = \mathcal{H}(\mathcal{R}_0)$ are diagonal

$$\mathcal{R}_0 = \begin{pmatrix} 0 & 0 \\ 0 & 1 \end{pmatrix} \quad \text{and} \quad \mathcal{H}_0 = \begin{pmatrix} E_n & 0 \\ 0 & -E_n \end{pmatrix}. \quad (2.7)$$

From Eq. (2.6) it follows that the matrix $\delta\mathcal{R}$ has the form

$$\delta\mathcal{R} = \begin{pmatrix} 0 & \delta R \\ -\delta R^* & 0 \end{pmatrix}, \quad (2.8)$$

and the linearized equation of motion (1.77) reduces to

$$i\partial_t\mathcal{R} = [\mathcal{H}_0, \delta\mathcal{R}] + \left[\frac{\delta\mathcal{H}}{\delta\mathcal{R}}\delta\mathcal{R}, \mathcal{R}_0 \right]. \quad (2.9)$$

Since the mesonic degrees of freedom are eliminated, we have to vary only with respect to changes in the density $\delta\mathcal{R}$ to obtain the Quasiparticle Random Phase (RQRPA) equation:

$$\begin{pmatrix} A & B \\ -B^* & -A^* \end{pmatrix} \begin{pmatrix} X^v \\ Y^v \end{pmatrix} = \omega_v \begin{pmatrix} X^v \\ Y^v \end{pmatrix}, \quad (2.10)$$

where X^v and Y^v amplitudes are defined as,

$$X_{kk'}^v = \langle 0 | \alpha_k \alpha_{k'} | v \rangle \quad (2.11)$$

$$Y_{kk'}^v = \langle 0 | \alpha_k^+ \alpha_{k'}^+ | v \rangle. \quad (2.12)$$

For $k < k'$, $l < l'$ we find the following RQRPA-matrices:

$$A_{kk'l'l'} = (E_k + E_{k'}) \delta_{kl} \delta_{k'l'} + \frac{\delta^2 E}{\delta R_{kk'}^* \delta R_{ll'}} \quad \text{and} \quad B_{kk'l'l'} = \frac{\delta^2 E}{\delta R_{kk'}^* \delta R_{ll'}^*}. \quad (2.13)$$

In cases where the two-body Hamiltonian \hat{H} does not depend on the density, the matrices A and B can be found in textbooks [85]:

$$\begin{aligned} A_{kk'l'l'} &= \left\langle \Phi \left| \left[\alpha_{k'} \alpha_k, \left[\hat{H}, \alpha_l^+ \alpha_{l'}^+ \right] \right] \right| \Phi \right\rangle \\ B_{kk'l'l'} &= - \left\langle \Phi \left| \left[\alpha_{k'} \alpha_k, \left[\hat{H}, \alpha_{l'} \alpha_l \right] \right] \right| \Phi \right\rangle. \end{aligned} \quad (2.14)$$

Using the representation of the Hamiltonian in the quasiparticle basis

$$\begin{aligned} \hat{H} &= E_0 + \sum_{kk'} H_{kk'}^{11} \alpha_k^+ \alpha_{k'} + \frac{1}{4} \sum_{kk'l'l'} H_{kk'l'l'}^{22} \alpha_k^+ \alpha_{k'}^+ \alpha_{l'} \alpha_l \\ &+ \sum_{kk'l'l'} (H_{kk'l'l'}^{40} \alpha_k^+ \alpha_{k'}^+ \alpha_{l'}^+ \alpha_l^+ + h.c.) + \sum_{kk'l'l'} (H_{kk'l'l'}^{31} \alpha_k^+ \alpha_{k'}^+ \alpha_{l'}^+ \alpha_l + h.c.) \end{aligned}$$

we find

$$\begin{aligned} A_{kk'l'l'} &= H_{kl}^{11} \delta_{k'l'} - H_{k'l}^{11} \delta_{kl} - H_{kl'}^{11} \delta_{k'l} + H_{k'l'}^{11} \delta_{kl} + H_{kk'l'l'}^{22} \\ B_{kk'l'l'} &= 4H_{kk'l'l'}^{40}. \end{aligned} \quad (2.15)$$

In the quasiparticle representation the matrix H^{11} is diagonal, i.e. $H_{kl}^{11} = E_k \delta_{kl}$. The matrices H^{22} and H^{40} are rather complicated expressions containing the two-body ph - and pp -matrix elements and the coefficients U and V , the solutions of the self-consistent Hartree-Bogoliubov equations. For the general case of a density dependent Hamiltonian we can use the same expressions, but we have to take into account the rearrangement terms originating from the variation of the interaction with respect to the density $\hat{\rho}$. In the case of linear meson-couplings the interactions are of Yukawa type whereas in the case of non-linear meson couplings we have to use the numerically determined meson-propagator of the Klein-Gordon equation described in Ref. [87].

2.2 Relativistic QRPA in the RHB Canonical Basis

2.2.1 Fully Self-Consistent RQRPA equations

The practical evaluation of the matrix elements $A_{kk',ll'}$ and $B_{kk',ll'}$ is rather complicated. It is considerably simplified in BCS approximation, because in this case we only have to calculate the two-body matrix elements $V_{kk',ll'}$ in the Hartree basis. The quasiparticle transformation consists in an appropriate multiplying with BCS-occupation factors.

According to the theorem of Bloch and Messiah [88], any RHB wave function can be written either in the quasiparticle basis as a product of independent quasiparticle states, or

in the canonical basis as a highly correlated BCS-state. Using this basis, we can therefore simplify the Relativistic Quasi-particle RPA equations considerably. For systems with an even number of particles we have

$$|\Phi\rangle = \prod_{\mu>0} (u_\mu + v_\mu a_\mu^\dagger a_{\bar{\mu}}^\dagger) |-\rangle, \quad (2.16)$$

where $|-\rangle$ denotes the nucleon vacuum, the operators a_μ^\dagger and $a_{\bar{\mu}}^\dagger$ create nucleons in the canonical basis, and the occupation probabilities are given by

$$v_\mu^2 = \frac{1}{2} \left(1 - \frac{\varepsilon_\mu - m - \lambda}{\sqrt{(\varepsilon_\mu - m - \lambda)^2 + \Delta_\mu^2}} \right). \quad (2.17)$$

$\varepsilon_\mu = \langle \mu | \hat{h}_D | \mu \rangle$ and $\Delta_\mu = \langle \mu | \hat{\Delta} | \bar{\mu} \rangle$ are the diagonal elements of the Dirac single-particle Hamiltonian and the pairing field in the canonical basis, respectively. In contrast to the BCS framework, however, neither of these fields is diagonal in the canonical basis. The basis itself is specified by the requirement that it diagonalizes the single-nucleon density matrix $\hat{\rho}(\mathbf{r}, \mathbf{r}') = \sum_{k>0} V_k(\mathbf{r}) V_k^\dagger(\mathbf{r}')$. Its eigenvalues are the occupation numbers (2.17).

Many of these occupation numbers vanish, in particular those at very high energies in the continuum, but also those corresponding to the levels in the Dirac sea, which are not occupied because of the *no-sea* approximation. Because of this degeneracy the levels in the canonical basis are not uniquely determined by the numerical diagonalization of $\hat{\rho}(\mathbf{r}, \mathbf{r}')$. In fact, one obtains, in all practical applications, well defined eigenstates $|\mu\rangle$ of $\hat{\rho}$ with non-degenerate eigenvalues $0 < v_\mu^2 < 1$, but in addition arbitrary linear combinations of all the eigenstates with eigenvalues 0 and also arbitrary linear combinations of all the eigenstates with eigenvalues 1. The pairing matrix elements Δ_μ of these additional arbitrary eigenvectors vanish, however the corresponding single particle energies are arbitrary and unphysical. The reason for this arbitrariness is that the requirement of diagonalization of the matrix $\hat{\rho}$ says nothing about the treatment of the two orthogonal subspaces with eigenvalues 0 and with eigenvalues 1. Within these two subspaces the canonical basis is just not defined.

We therefore introduce the additional requirement, that the canonical basis in these subspaces diagonalizes the single particle Hamiltonian \hat{h}_D . This definition is obvious and meaningful, because it leads to the Hartree basis in the case of vanishing pairing correlations, where Hartree-Bogoliubov theory becomes simply Hartree theory. In practical applications we therefore first diagonalize the matrix $\hat{\rho}$. This gives us all the canonical basis states with $0 < v_\mu^2 < 1$ and in addition eigenstates with eigenvalues 0 and 1. Two eigenstates $|\mu\rangle$, $|\nu\rangle$ are selected as degenerated, if their eigenvalues are different less than a given parameter ϵ_d , i.e.

$$|v_\mu^2 - v_\nu^2| < \epsilon_d. \quad (2.18)$$

Furthermore we calculate the single particle Hamiltonian \hat{h}_D in the basis of all the states with eigenvalue $v_\mu^2 = 0$ and diagonalize this operator in the corresponding subspace. All the new eigenvectors obtained in this way are also eigenstates of $\hat{\rho}$ with eigenvalue 0 and

are of course orthogonal to all the other eigenvectors of $\hat{\rho}$ with non-vanishing eigenvalues. Finally we consider the subspace of eigenvectors with eigenvalue 1 (fully occupied states in the Fermi sea) and proceed in a similar way. This procedure is particularly important in relativistic calculations, where the diagonalization of $\hat{\rho}$ alone leads to linear combinations of states in the Dirac sea and unoccupied states high up in the positive energy continuum.

With this prescription to the canonical basis determines the energies ε_μ and occupation probabilities v_μ^2 of single-nucleon states, that correspond to the self-consistent solution for the ground state of the nucleus. As discussed in Ref. [7] the density matrix is localized. The canonical states $|\mu\rangle$ with $v_\mu^2 > 0$ are localized too.

In the canonical basis the matrices A and B have BCS-form. We only have to consider, that the matrix H^{11} is not diagonal in this basis. We finally obtain:

$$\begin{aligned} A_{\mu\mu'\nu\nu'} &= H_{\mu\nu}^{11}\delta_{\mu'\nu'} - H_{\mu'\nu}^{11}\delta_{\mu\nu} - H_{\mu\nu'}^{11}\delta_{\mu'\nu} + H_{\mu'\nu'}^{11}\delta_{\mu\nu} \\ &+ \frac{1}{2}V_{\mu\bar{\nu}'\bar{\mu}'\nu}^{ph} (\eta_{\mu\mu'}^+ \eta_{\nu\nu'}^+ + \eta_{\mu\mu'}^- \eta_{\nu\nu'}^-) - (\nu \leftrightarrow \nu') \\ &+ \frac{1}{2}V_{\mu\mu'\nu\nu'}^{pp} (\xi_{\mu\mu'}^+ \xi_{\nu\nu'}^+ + \xi_{\mu\mu'}^- \xi_{\nu\nu'}^-) \end{aligned} \quad (2.19)$$

and

$$\begin{aligned} B_{\mu\mu'\nu\nu'} &= \frac{1}{2}V_{\mu\nu\bar{\mu}'\bar{\nu}'}^{ph} (\eta_{\mu\mu'}^+ \eta_{\nu\nu'}^+ + \eta_{\mu\mu'}^- \eta_{\nu\nu'}^-) - (\nu \leftrightarrow \nu') \\ &+ \frac{1}{2}V_{\mu\mu'\bar{\nu}\bar{\nu}'}^{pp} (\xi_{\mu\mu'}^+ \xi_{\nu\nu'}^+ - \xi_{\mu\mu'}^- \xi_{\nu\nu'}^-) \end{aligned} \quad (2.20)$$

where

$$\eta_{\mu\mu'}^\pm = u_\mu v_{\mu'} \pm v_\mu u_{\mu'} , \quad (2.21)$$

and

$$\xi_{\mu\mu'}^\pm = u_\mu u_{\mu'} \mp v_\mu v_{\mu'} . \quad (2.22)$$

and

$$H_{\mu\nu}^{11} = (u_\mu u_\nu - v_\mu v_\nu)h_{\mu\nu} - (u_\mu v_\nu + v_\mu u_\nu)\Delta_{\mu\nu} , \quad (2.23)$$

The ph - and pp -matrix elements $V_{\mu\nu\mu'\nu'}^{ph}$ and $V_{\mu\mu'\nu\nu'}^{pp}$ can be derived as second derivatives of the energy functional with respect to the normal and anomalous densities:

$$V_{\mu\nu\mu'\nu'}^{ph} = \frac{\delta^2 E}{\delta \hat{\rho}_{\mu\mu'} \delta \hat{\rho}_{\nu\nu'}}, \quad V_{\mu\mu'\nu\nu'}^{pp} = \frac{\delta^2 E}{\delta \hat{\kappa}_{\mu\mu'} \delta \hat{\kappa}_{\nu\nu'}} \quad (2.24)$$

In spherical systems we couple to good angular momentum. In this case we find the matrix equations of the relativistic quasiparticle random phase approximation (RQRPA) read

$$\begin{pmatrix} A^J & B^J \\ B^{*J} & A^{*J} \end{pmatrix} \begin{pmatrix} X^{v, JM} \\ Y^{v, JM} \end{pmatrix} = \omega_v \begin{pmatrix} 1 & 0 \\ 0 & -1 \end{pmatrix} \begin{pmatrix} X^{v, JM} \\ Y^{v, JM} \end{pmatrix} . \quad (2.25)$$

For each RQRPA energy ω_v , (X^v) and (Y^v) denote the corresponding forward- and backward-going two-quasiparticle amplitudes, respectively. The coupled RQRPA matrices in the canonical basis read

$$\begin{aligned}
A_{\mu\mu'\nu\nu'}^J &= H_{\mu\nu}^{11(J)}\delta_{\mu'\nu'} - H_{\mu'\nu}^{11(J)}\delta_{\mu\nu} - H_{\mu\nu'}^{11(J)}\delta_{\mu'\nu} + H_{\mu'\nu'}^{11(J)}\delta_{\mu\nu} \\
&\quad + \frac{1}{2}(\xi_{\mu\mu'}^+\xi_{\nu\nu'}^+ + \xi_{\mu\mu'}^-\xi_{\nu\nu'}^-)V_{\mu\mu'\nu\nu'}^{ppJ} \\
&\quad + \zeta_{\mu\mu'\nu\nu'}V_{\mu\nu'\mu'\nu}^{phJ}
\end{aligned} \tag{2.26}$$

$$\begin{aligned}
B_{\mu\mu'\nu\nu'}^J &= \frac{1}{2}(\xi_{\mu\mu'}^+\xi_{\nu\nu'}^+ - \xi_{\mu\mu'}^-\xi_{\nu\nu'}^-)V_{\mu\mu'\nu\nu'}^{ppJ} \\
&\quad + \zeta_{\mu\mu'\nu\nu'}(-1)^{j_\nu-j_{\nu'}+J}V_{\mu\nu'\mu'\nu}^{phJ}.
\end{aligned} \tag{2.27}$$

The relativistic particle-hole interaction V^{ph} is defined by the same energy functional as the mean-field Dirac single-nucleon Hamiltonian \hat{h}_D (1.30), i.e.

$$\begin{aligned}
V^{ph}(\mathbf{r}_1, \mathbf{r}_2, s_1, s_2, \tau_1, \tau_2) &= -g_\sigma^2 G_\sigma(\mathbf{r}_1, \mathbf{r}_2) + g_\omega^2 G_\omega(\mathbf{r}_1, \mathbf{r}_2) \\
&\quad + g_\rho^2 G_\rho(\mathbf{r}_1, \mathbf{r}_2)\gamma_\mu^{(1)}\gamma^{\mu(2)}\vec{\tau}^{(1)}\vec{\tau}^{(2)} \\
&\quad + e^2 G_c(\mathbf{r}_1, \mathbf{r}_2)\gamma_\mu^{(1)}\gamma^{\mu(2)}.
\end{aligned} \tag{2.28}$$

It includes the exchange of the isoscalar scalar σ -meson, the isoscalar vector ω -meson, the isovector vector ρ -meson, and the electromagnetic interaction, where $G_m(\mathbf{r}_1, \mathbf{r}_2)$ are meson propagators. The two-body matrix elements include contributions from the spatial components of the vector fields. The single-nucleon occupation probabilities are collected within the following factors, with respect to (2.22), (2.21):

$$\zeta_{\mu\mu'\nu\nu'} = \begin{cases} \eta_{\mu\mu'}^+\eta_{\nu\nu'}^+ & \text{for } \sigma, \omega^0, \rho^0, A^0 \text{ if J is even} \\ & \text{for } \omega^i, \rho^i, A^i \text{ if J is odd} \\ \eta_{\mu\mu'}^-\eta_{\nu\nu'}^- & \text{for } \sigma, \omega^0, \rho^0, A^0 \text{ if J is odd} \\ & \text{for } \omega^i, \rho^i, A^i \text{ if J is even} \end{cases}$$

The RQRPA configuration space includes the Dirac sea of negative energy states. In addition to the configurations built from two-quasiparticle states of positive energy, the RQRPA configuration space must also contain pair-configurations formed from the fully or partially occupied states of positive energy and the empty negative-energy states from the Dirac sea. The inclusion of configurations built from occupied positive-energy states and empty negative-energy states is essential for current conservation and the decoupling of spurious states [89]. In recent applications of the relativistic RPA it has been shown that the fully consistent inclusion of the Dirac sea of negative energy states in the RQRPA configuration space is essential for a quantitative comparison with the experimental excitation energies of giant resonances [50, 53].

The dimension of the RQRPA configuration space is thus determined by two cut-off parameters: the maximum value of the sum of diagonal matrix elements of the Dirac single-nucleon Hamiltonian for the two-quasiparticle states of positive energy, and the sum of diagonal matrix elements of \hat{h}_D for the pairs built from occupied positive-energy states and empty negative-energy states.

It should be emphasized that the present RQRPA model is fully self-consistent: the same interactions, both in the particle-hole and particle-particle channels, are used in the RHB equation (1.82) that determines the canonical quasiparticle basis, and in the RQRPA equation (2.25). In both channels the same strength parameters of the interactions are used in the RHB and RQRPA calculations. The parameters of the effective interactions are completely determined in RHB calculations of ground-state properties, and no additional adjustment is needed in RQRPA calculations. This is an essential feature of our model and it ensures that RQRPA amplitudes do not contain spurious components associated with the mixing of the nucleon number in the RHB ground state (for 0^+ excitations), or with the center-of-mass translational motion (for 1^- excitations).

2.2.2 RQRPA Strength Distributions and Transition Densities

Multipole electric transitions in atomic nuclei are described by the reduced transition probability [85],

$$B^T(EJ, J_i \rightarrow J_f) = \frac{1}{2J_i + 1} |\langle f || \hat{Q}_J^T || i \rangle|^2, \quad (2.29)$$

where \hat{Q}_J^T corresponds to the electric multipole transition. The isoscalar monopole operator is defined as

$$\hat{Q}_{J=0}^{T=0} = \sum_{i=1}^A r_i^2 Y_{00}(\hat{r}_i), \quad (2.30)$$

while

$$\hat{Q}_{JM}^{T=0} = e \sum_{i=1}^A r_i^J Y_{JM}(\hat{r}_i) \quad (2.31)$$

$$\hat{Q}_{JM}^{T=1} = e \sum_{i=1}^A \tau_z^{(i)} r_i^J Y_{JM}(\hat{r}_i) \quad (2.32)$$

correspond to multipole ($J>0$) isoscalar ($T=0$) and isovector ($T=1$) operators. Since the lowest order isoscalar dipole ($J=1$) transition operator produces a spurious center-of-mass motion, in practical calculations we use the effective operator

$$\hat{Q}_{1M}^{T=0} = e \sum_{i=1}^A \gamma_0 \left(r_i^3 - \frac{5}{3} \langle r^2 \rangle_0 r_i \right) Y_{1M}(\hat{r}_i), \quad (2.33)$$

in order to ensure that the strength distribution does not contain spurious components [90]. To describe the isovector dipole excitations, we use the effective transition operator, i.e.

$$\hat{Q}_{1M}^{T=1} = e \sum_{i=1}^A \left(\tau_z^{(i)} - \frac{N-Z}{2A} \right) r_i Y_{1M}(\hat{r}_i), \quad (2.34)$$

where the center-of-mass correction term is subtracted from the original operator, leading to

$$\hat{Q}_{1M}^{T=1} = e \frac{N}{N+Z} \sum_{p=1}^Z r_p Y_{1M}(\hat{r}_p) - e \frac{Z}{N+Z} \sum_{n=1}^N r_n Y_{1M}(\hat{r}_n). \quad (2.35)$$

The reduced transition probability for each set of the RQRPA eigen-solutions (ω_v, X^v, Y^v) is defined as,

$$B^T(EJ, \omega_v) = \frac{1}{2J_i + 1} \left| \sum_{\mu\mu'} \left\{ X_{\mu\mu'}^{v,J0} \langle \mu || \hat{Q}_J^T || \mu' \rangle + (-1)^{j_\mu - j_{\mu'} + J} Y_{\mu\mu'}^{v,J0} \langle \mu' || \hat{Q}_J^T || \mu \rangle \right\} (u_\mu v_{\mu'} + (-1)^J v_\mu u_{\mu'}) \right|^2, \quad (2.36)$$

where v and u are coefficients related to the occupation probabilities of the single particle levels in the canonical basis.

The RQRPA transition density for the state $|v\rangle$ is expressed as

$$\delta\rho^v(\mathbf{r}) = \delta\rho_J^v(r) Y_{JM}^*(\hat{\mathbf{r}}), \quad (2.37)$$

where the radial part is defined by

$$\delta\rho_J^v(r) = \sum_{\mu\mu'} \left\{ \langle \mu || Y_J || \mu' \rangle f_\mu(r) f_{\mu'}(r) + \langle \hat{\mu} || Y_J || \hat{\mu}' \rangle g_\mu(r) g_{\mu'}(r) \right\} \cdot \left(X_{\mu\mu'}^{v,J0} + (-1)^J Y_{\mu\mu'}^{v,J0} \right) (u_\mu v_{\mu'} + (-1)^J v_\mu u_{\mu'}), \quad (2.38)$$

where μ and $\hat{\mu}$ denote the quantum numbers of the large and small components of the Dirac spinors, respectively. $f_\mu(r)$ and $g_\mu(r)$ are the corresponding large and small radial components.

2.2.3 Spurious Solutions of the RQRPA Equations

Whenever the generator of a continuous symmetry for a general two-body Hamiltonian ($[H, \hat{S}] = 0$), defined by a hermitian one body operator,

$$\hat{S} = \sum_{ij} \langle i | S | j \rangle a_i^\dagger a_j \quad (2.39)$$

does not commute with the original single-particle density, i.e.

$$[\hat{S}, \rho_0] \neq 0 \quad (2.40)$$

it produces a spurious zero-energy solution of RPA equations [85], i.e.

$$\begin{pmatrix} A^J & B^J \\ B^{*J} & A^{*J} \end{pmatrix} \begin{pmatrix} S \\ -S^* \end{pmatrix} = 0. \quad (2.41)$$

It corresponds to a mode which is not related to an intrinsic excitation of the system, but to a collective motion without the restoring force. The spurious state is orthogonal to all other excitation states. In practice, spurious modes can be incited by different types of the symmetry violating transformations, e.g. translation, particle number and rotation. In an ideal case, when the RPA model is built on the self-consistent wave functions and single-particle energies, the spurious excitation should decouple from the physical states, at exactly zero energy. In practical calculations, however, because of numerical inaccuracies, truncation of the ph configuration space, and inconsistencies among the ground state and RPA equations, the spurious state is separated at energies somewhat higher than zero. Then the physical states may be more or less mixed together with the spurious response, leading to the seriously overestimated strength distributions.

There are several approaches to overcome this problem. In particular, in RPA models which are not fully self-consistent, the residual interaction is adjusted with a free parameter until the spurious state is properly decoupled. In the case of isoscalar dipole excitations (ISGDR), the spurious translational motion related to the operator

$$\hat{S} = e \sum_{i=1}^A r_i Y_{1M}(\hat{r}_i). \quad (2.42)$$

has the same quantum numbers as actual ISGDR mode. It is the first order of the expansion for the dipole operator $j_1(qr_i)Y_{1M}(\hat{r}_i)$. Since the operator from the next order of expansion, which we actually use in calculations, $r^3 Y_{1M}(\hat{r}_i)$ includes both $1\hbar\omega$ and $3\hbar\omega$ $2qp$ excitations, it could also be a subject leading to significant spurious impurities. These contributions can be extracted by subtracting from the operator $r^3 Y_{1M}(\hat{r}_i)$ (2.33) a term $\eta r_i Y_{1M}(\hat{r}_i)$ which eliminates spurious contributions to the actual physical states of dipole resonance [90]. The parameter

$$\eta = \frac{5}{3} \langle r^2 \rangle_0 \quad (2.43)$$

is determined from the condition of translational invariance of a nucleus, i.e.

$$\int \delta\rho(r) r Y_{10}(\hat{r}) d^3r = 0. \quad (2.44)$$

An alternative way would be to remove the spurious contributions directly from the RPA eigenfunctions [64, 91]. Here we need the reduced transition probability defined via transition density,

$$B^T(EJ, \omega_v) = \sum_M \left| \int \delta\rho^v(\mathbf{r}) \hat{Q}_{JM}^T d^3r \right|^2. \quad (2.45)$$

Assuming that the transition density of a spurious state is proportional to $d\rho_0/dr$, where ρ_0 is the ground state density, we correct the actual ISGDR transition densities by subtracting this term multiplied by a factor which is determined from the condition that

the strength distribution via the translational operator (2.42) and corrected transition densities vanishes, i.e.

$$\int \left(\delta\rho_J^v(r) - a_v \frac{d\rho_0}{dr} \right) r^3 dr = 0. \quad (2.46)$$

This equation on a_v is solved for each RQRPA eigenvalue ω_v . By using corrected transition densities, and transition operator $r^3 Y_{1M}(\hat{r}_i)$, we can evaluate from Eq. (2.45) the strength distribution with eliminated spurious strength. We get almost the same strength distributions by using this method or by direct calculation with operator (2.33). This result is in agreement with the conclusion from the Ref. [64].

The truncation of actual RQRPA configuration space may strongly affect the behavior of spurious states. The size of 2qp space is determined by two cut-off parameters: the maximum value of the sum of diagonal matrix elements of the Dirac single-nucleon Hamiltonian for the two-quasiparticle states of positive energy (E_{Cp}), and the sum of diagonal matrix elements of \hat{h}_D for the pairs built from occupied positive-energy states and empty negative-energy states (E_{Ca} is absolute value of this quantity). The cut-off parameters E_{Cp}, E_{Ca} , as well as the degeneracy parameter ϵ_d from (2.18) are selected in a way to ensure that the following properties are fulfilled: (a) the response related to the nucleon number operator vanishes, and the corresponding Nambu-Goldstone mode has a zero excitation energy, (b) the spurious excitation corresponding to a translation of a nucleus decouples as a zero excitation mode, and (c) the excitation energies of giant resonances and low-lying states converge to stable solutions independent from the cut-off and ϵ_d parameters. The present RHB+RQRPA model is fully consistent with (a)-(c) conditions.

First we show how the RQRPA results depend on the degeneracy parameter ϵ_d (2.18) which determines if two canonical basis states have degenerated eigenvalues, i.e. occupation numbers. The isovector dipole strength distribution for $\epsilon_d = 10^{-4} - 10^{-7}$ is shown in Fig. 2.1(a). In the case when $\epsilon_d < 10^{-6}$, the dipole response slightly varies, especially the low-lying region. However, ϵ_d can be clearly determined from the conditions related to extraction of the spurious states. In particular, for $\epsilon_d < 10^{-4}$, the 1^- spurious state becomes a complex number; its imaginary part decreases until $\epsilon_d \approx 10^{-6}$, where we get a real energy of spurious excitation at 0.1 MeV. This property is also reflected in Fig. 2.1(a): for $\epsilon_d < 10^{-6}$, the spurious states are properly decoupled, and plotted strength distributions for $\epsilon_d = 10^{-6}$ and 10^{-7} are exactly the same. The same applies to other nuclei. From the number operator response, we drew the same conclusion. In the present analysis, therefore we use systematically the degeneracy parameter with a fixed value $\epsilon_d = 10^{-6}$.

In Fig. 2.1(b) we illustrate in ^{22}O how the response to the neutron number operator varies with the cut-off $E_{Cp} = 30\text{-}270$ MeV, while $E_{Ca}=1700$ MeV to include the entire negative-energy spectrum from Dirac sea. As the number of 2qp configurations increases, the response for the number operator clearly disappears. Already for $E_{Cp}=90$ MeV (84 2qp / 41 antiparticle - quasiparticle (ap-qp) pairs), the transition strength along the whole region up to 50 MeV falls down to the values less than 0.004 1/MeV, while the Nambu-Goldstone mode converges toward 0.2 MeV. In order to remove the spurious 1^- excitation, it is also necessary to include a large configuration space. In Fig. 2.1(c) we

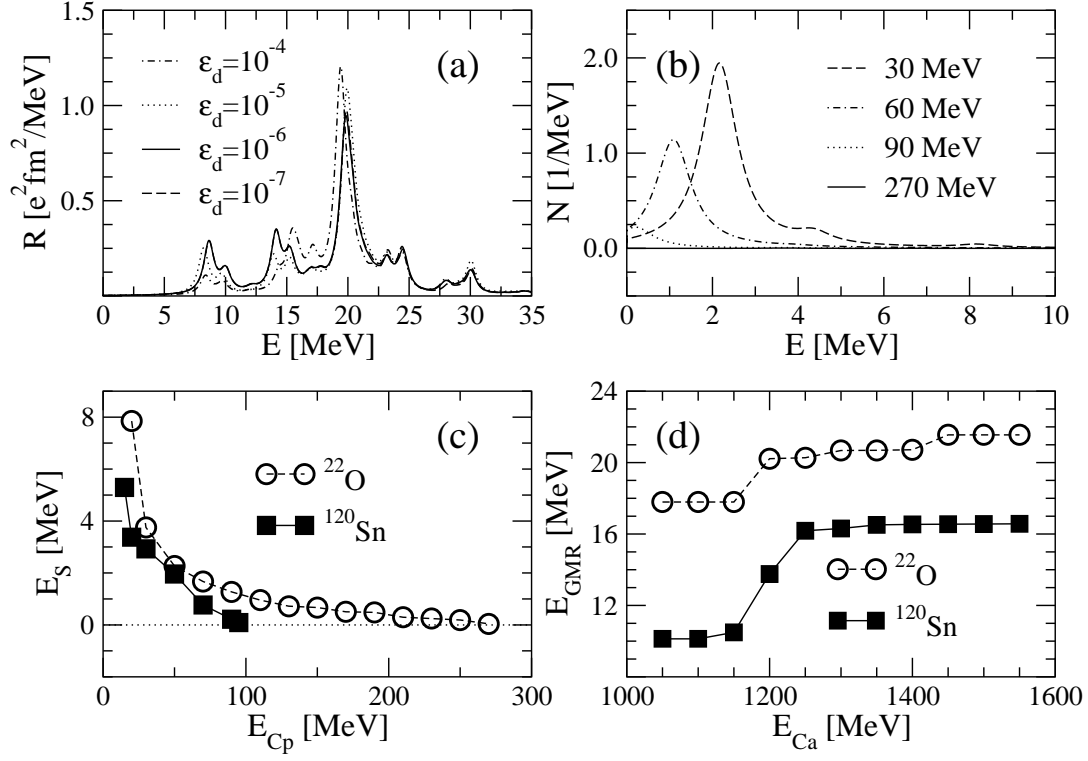


Figure 2.1: (a) Isovector dipole strength distribution for different values of ϵ_d (2.18). (b) RQRPA response for the neutron number operator in ^{22}O for 2qp cut-off energy E_{Cp} =30-270 MeV. The corresponding cut-off for configurations which include antiparticle states is fixed, E_{Ca} =1700 MeV. (c) The position of the spurious 1^- state in ^{22}O and ^{120}Sn as a function of 2qp cut-off energy; E_{Ca} =1700 MeV. (d) The ISGMR energy in ^{22}O and ^{120}Sn as a function of the cut-off energy E_{Ca} for 2qp pairs which include transitions to the negative-energy Dirac sea (E_{Cp} =270 MeV and E_{Cp} =100 MeV in ^{22}O and ^{120}Sn , respectively)

plot the energy of a 1^- spurious state in ^{22}O and ^{120}Sn as a function of the energy cut-off E_{Cp} with $E_{Ca}=1700$ MeV. In both cases, the convergence of a spurious state toward zero excitation energy is obtained, in relatively large space with 250 and 800 configurations for ^{22}O and ^{120}Sn , respectively.

The cut-off parameter E_{Ca} related to configurations which include antiparticle states, has an important role for a proper description of the multipole response in nuclei. As it was noted in Ref. [89], if these contributions are not included, the energy of the 1^- spurious state becomes imaginary, and it never approaches zero. The RHB+RQRPA model has the same property: even with incomplete set of ap-qp pairs, the diagonalization of RQRPA matrix may result with complex eigenvalues for the spurious 1^- state. When a sufficiently large configuration space is selected, this problem is avoided. Giant monopole resonances (GMR) are especially sensitive to the inclusion of ap-qp configurations. In Fig. 2.1(d) we show how the corresponding energy cut-off E_{Ca} can be selected. The GMR peak in both ^{22}O and ^{120}Sn for $E_{Ca} \leq 1150$ MeV is built from the usual 2qp pairs only. However, as E_{Ca} increases to include the effects from the negative energy states, the GMR energy becomes larger and it saturates for $E_{Ca} > 1500$ MeV.

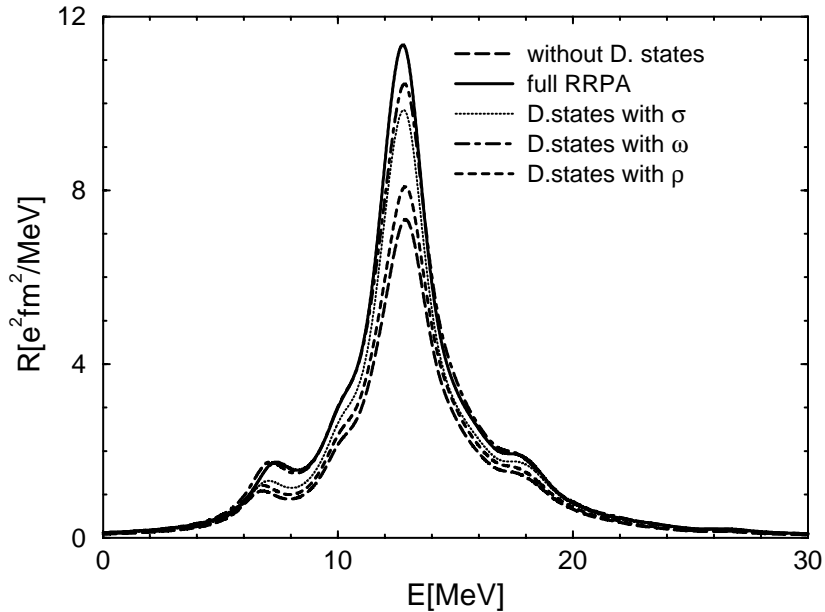


Figure 2.2: Isovector dipole strength distributions in ^{208}Pb calculated with the NL3 effective interaction. The solid and long-dashed curves are the RRPA strengths with and without the inclusion of Dirac sea states, respectively. The dotted, dot-dashed and short-dashed curves correspond to calculations in which only the σ , the ω and the ρ meson field are included in the coupling between the Fermi sea and Dirac sea states, respectively.

In the following, we illustrate the impact of the Dirac sea states in the case of isovector giant dipole resonances (IVGDR). In Fig. 2.2 we plot the isovector dipole strength dis-

tribution for ^{208}Pb . The solid and long-dashed curves are the RRPA strengths with and without the inclusion of Dirac sea states, respectively. The dotted, dot-dashed and short-dashed curves correspond to calculations in which only the σ , the ω and the ρ meson field are included in the coupling between the Fermi sea and Dirac sea states, respectively. We notice that, although the position of the peak is not sensitive to the inclusion of negative energy states, these configurations affect the total intensity, i.e. the values of the calculated energy weighted moments. In particular, if the negative energy Dirac sea states are not included in the RRPA configuration space, only 72.8% of the energy weighted sum rule is exhausted, as compared with the full RRPA calculation with both positive and negative energy states. When only the σ , the ω , or the ρ meson couple the particle-hole states with negative energy Dirac sea states, 89.4%, 98.3% and 79.2% of the full RRPA energy weighted sum rule is exhausted, respectively. However, in the case of isoscalar excitations more serious effects have been observed. Without the inclusion of the Dirac sea states, the position of an isoscalar giant resonances is lowered in energy by several MeV [51]. The self-consistent RQRPA framework used in the present work includes configurations built from both occupied positive-energy states and negative-energy states.

In the left panel of Fig. 2.3 we display the monopole strength function of the neutron number operator in ^{22}O . There should be no response to the number operator since it is a conserved quantity, i.e. the Nambu-Goldstone mode associated with the nucleon number conservation should have zero excitation energy. The dashed curve (no dynamical pairing) represents the strength function obtained when the pairing interaction is included only in the RHB calculation of the ground state, but not in the residual interaction of the RQRPA. The solid line (zero response) corresponds to the full RHB+RQRPA calculation, with the pairing interaction included both in the RHB ground state, and in the RQRPA residual interaction. The same result was also obtained in the HFB+QRPA calculation for ^{24}O in Ref. [38]: the spurious strength of the number operator appears when the pairing interaction is included only in the stationary solution for the ground state, i.e. when the dynamical QRPA pairing correlations are neglected.

The isoscalar strength functions of the monopole operator (2.30) in ^{22}O , shown in the right panel of Fig. 2.3, correspond to three different calculations: a) the RMF+RRPA calculation without pairing, b) pairing correlations are included in the RHB calculation of the ground state, but not in the RRPA residual interaction (no dynamical pairing), and c) the fully self-consistent RHB+RQRPA calculation. Just as in the case of the number operator, by including pairing correlations only in the RHB ground state a strong spurious response is generated below 10 MeV. The Nambu-Goldstone mode is found at zero excitation energy (in this particular calculation it was located below 0.2 MeV) only when pairing correlations are consistently included also in the residual RQRPA interaction. When the result of the full RHB+RQRPA is compared with the response calculated without pairing, one notices that, as expected, pairing correlations have relatively little influence on the response in the region of giant resonances above 20 MeV. A more pronounced effect is found at lower energies. The fragmentation of the single peak at ≈ 12.5 MeV reflects the broadening of the Fermi surface by the pairing correlations.

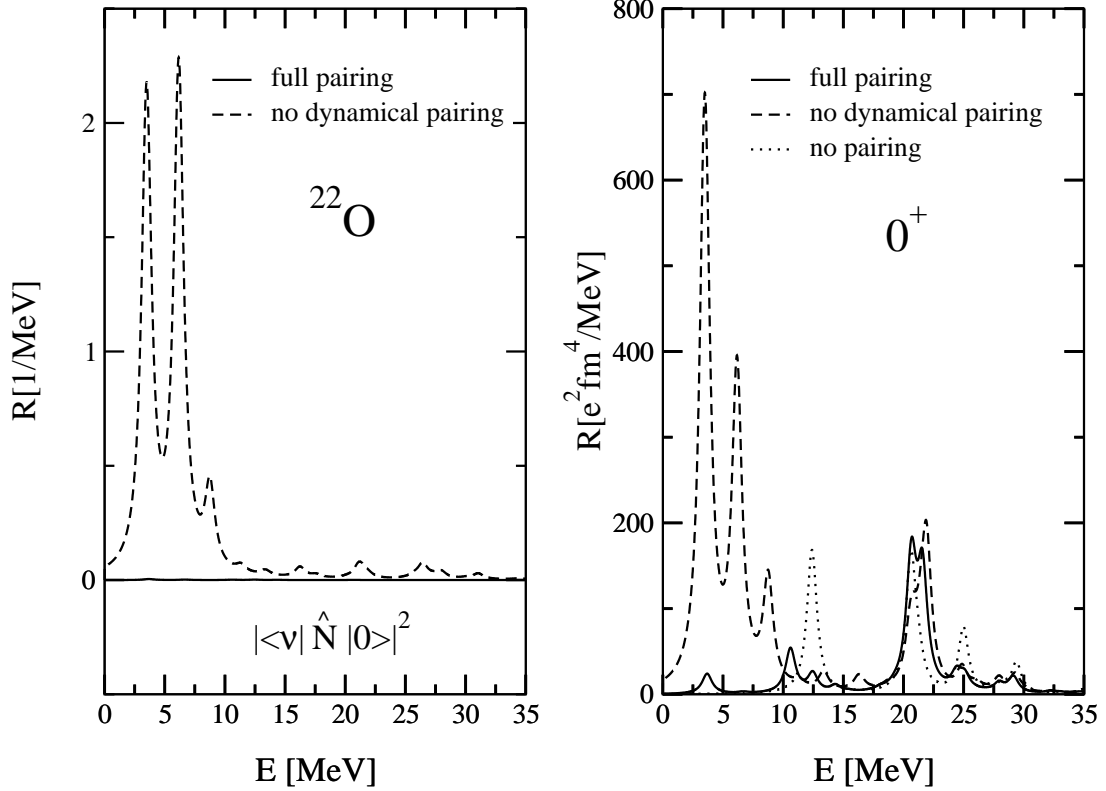


Figure 2.3: The strength function for the neutron number operator (left), and the isoscalar strength function for the monopole operator (right) in ^{22}O . The curves correspond to the RMF+RRPA calculation without pairing (dotted), with pairing correlations included in the RHB calculation of the ground state, but not in the RRPA residual interaction (dashed), and to the fully self-consistent RHB+RQRPA calculation (solid).

2.2.4 Sum Rules of the Multipole Strength in Relativistic QRPA

The discrete RQRPA strength distributions for given multipole operator we average with a Lorentzian function, resulting with the continuous strength function,

$$R(E) = \sum_v B^T(J, \omega_v) \frac{1}{\pi} \frac{\Gamma/2}{(E - \omega_v)^2 + (\Gamma/2)^2}. \quad (2.47)$$

The reduced transition probability $B^T(J, \omega_v)$ is defined in Eq.(2.36), while the arbitrary width of the Lorentzian distribution, Γ is fixed in this work to the value 1 MeV. The Lorentzian function (2.47) is defined in a way to fulfill the condition that the energy weighted summed response (EWSR) of a discrete distribution equals the EWSR of the corresponding continuous strength function, i.e.

$$S_{EW}(EJ) = \sum_{v>0} E_v B^T(EJ, \omega_v) = \int ER(E)dE. \quad (2.48)$$

In the present work the EWSR (2.48) is evaluated in the interval below 50 MeV excitation energy. The knowledge of the sum rules is of special interest, since it represent a useful test of the models describing collective excitations [85]. The energy weighted sum(2.48) for a transition operator \hat{Q}_{JM} can be expressed in a double commutator form,

$$S_{EW}(EJ) = \frac{1}{2} \sum_{\phi \leq F} \langle \phi | [\hat{Q}, [H, \hat{Q}]] | \phi \rangle, \quad (2.49)$$

where $|\phi\rangle$ runs over all occupied single-particle states. If only contributions from the kinetic term are taken into account,

$$S_{EW}(EJ) = \frac{\hbar^2}{2m} \frac{(2\lambda + 1)^2}{4\pi} Z \langle r^{2\lambda-2} \rangle. \quad (2.50)$$

For the dipole operator (2.35) this reduces to the well known Thomas-Reiche-Kuhn (TRK) sum rule [85],

$$S_{EW}(E1) = \frac{\hbar^2}{2m} \frac{9}{4\pi} \frac{NZ}{A} e^2. \quad (2.51)$$

The isoscalar quadrupole energy weighted sum rule reads,

$$S_{EW}(E2) = \frac{25\hbar^2 e^2}{4\pi m} (N \langle r_n^2 \rangle + Z \langle r_p^2 \rangle) \quad (2.52)$$

and for the isoscalar monopole excitations,

$$S_{EW}(E0) = \frac{2\hbar^2 e^2}{m} (N \langle r_n^2 \rangle + Z \langle r_p^2 \rangle). \quad (2.53)$$

The classical sum rules (2.51)-(2.53) are only approximative quantities. In practical calculations they are usually enlarged by an enhancement factor due to the nucleon-nucleon potential term in the nuclear Hamiltonian [92].

However, in the relativistic approach, the sum over v in Eq.(2.48) runs not only over the positive excitation energies, but it also includes transitions from the occupied levels to the empty negative energy Dirac sea. The 2qp pairs which include the states from Dirac sea, contribute with negative definite terms in the EWSR. As it was pointed out in Refs. [93, 94, 95], in the RMFT approach, the double commutator in Eq.(2.49) vanishes, and summed EWSR is zero. It means that in RRPA the ordinary particle-hole contributions are exactly canceled by the response of vacuum due to excitation from an occupied state to the Dirac sea. The condition

$$\sum_v E_v B^T(EJ, \omega_v) = 0 \quad (2.54)$$

provide an excellent numerical test of the completeness for selected configurational space. In any relativistic RPA calculations built on the finite space of particle-hole and antiparticle-hole configurations, only the full EWSR rule should be exactly satisfied. If the configurational space is restricted by exclusion of antiparticle-hole pairs, negative contributions to

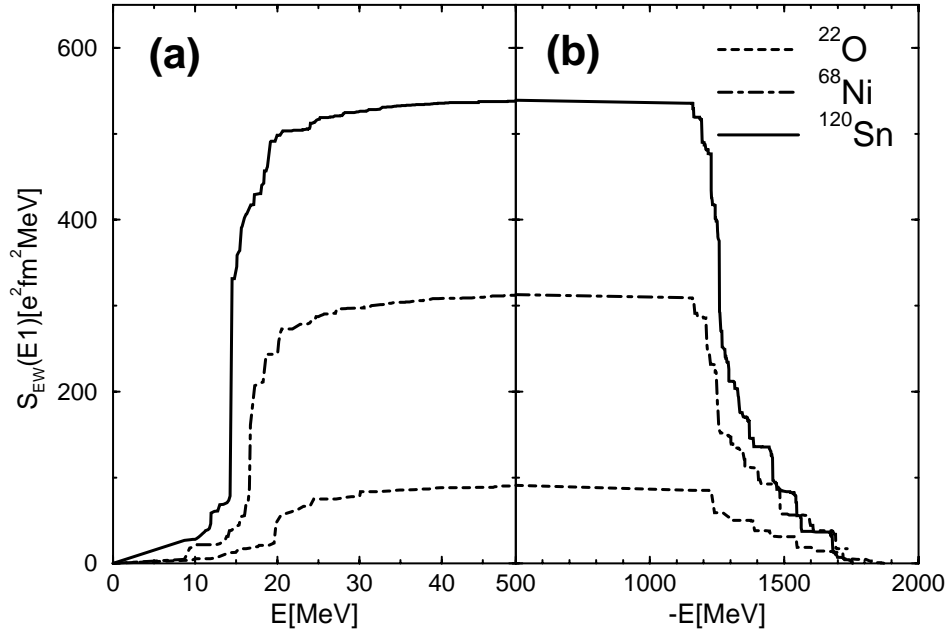


Figure 2.4: RQRPA energy weighted running sum for E1 excitations in the open-shell nuclei with (a) only the usual 2qp configurations, and (b) configurations with transitions to the Dirac sea are included. The energy on the E axis corresponds to the upper limit of energy in the summation of energy weighted transition strength(2.48)

(2.48) are dropped out. In this particular case, the nonrelativistic sum rules (2.51)-(2.53) should be only approximately recovered.

It is of a particular interest to see whether the RHB+RQRPA sum rules are well satisfied. In Fig. 2.4 we plot the running energy weighted sum (2.48) up to a given energy E in a selection of the open shell nuclei ^{22}O , ^{68}Ni and ^{120}Sn . When we restrict the summation of energy weighted transition strength (2.48) to the positive energies from usual 2qp excitations only, the sum quickly converges beyond 40 MeV to the final EWSR value (Fig. 2.4(a)). This value should be compared with the classical TRK sum rule (2.51). As expected, in the case of isovector dipole excitations, the EWSR exhausts somewhat more strength: between 110%-125% of TRK sum rule. However, as the negative energies related to the excitations in Dirac sea are included, the maximal EWSR drops very precisely to the zero value (Fig. 2.4(b)). Accordingly, we can conclude that the completeness properties are very accurately fulfilled in the present RHB+RQRPA calculations. In order to achieve this property, the self-consistent implementation of interactions in the RHB and RQRPA plays an important role. If the self-consistency is broken, as in the case when the pairing interactions are included in RHB, but not in the RQRPA, the relativistic sum rule (2.54) is not fulfilled. This is illustrated in Fig. 2.5, where for both the RHPA and RQRPA the energy weighted sum vanishes, in contrast to RQRPA without pairing in the residual

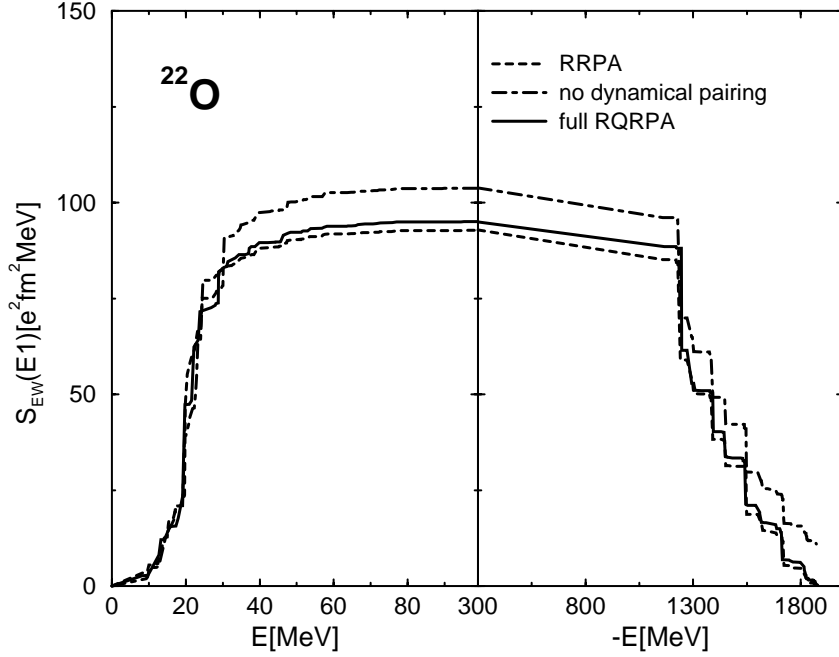


Figure 2.5: The running sum (the same like in Fig.2.4) in RRPA, RQRPA without dynamical pairing, and full RQRPA calculations for ^{22}O .

interaction, which results with an amount of $10.91 e^2 fm^2 MeV$ in total EWSR. Of course, the same conclusion applies to the excitations with other multiplicities.

The excitation energies of giant resonances are defined via energy moments of discrete transition strength distribution (2.36),

$$m_k = \sum_v E_v^k B^T(EJ, \omega_v), \quad (2.55)$$

or by using the continuous strength distribution function (2.47),

$$m_k = \int E^k R(E) dE. \quad (2.56)$$

In the case $k = 1$ this equation defines the energy weighted sum rule (2.48). If the strength distribution of a particular excitation mode has a well pronounced and symmetric resonance shape, its energy is well described by centroid energy,

$$\bar{E} = \frac{m_1}{m_0}. \quad (2.57)$$

Alternatively, mean energies are defined as

$$\bar{E}_k = \sqrt{\frac{m_k}{m_{k-2}}}, \quad (2.58)$$

where the difference between the values \bar{E}_1 and \bar{E}_3 can be used as an indication of how much the strength distribution corresponding to an excitation mode is actually fragmented [91]. If the multipole response is characterized by a single dominant peak, two moments are equal, i.e. $\bar{E}_1 = \bar{E}_3$.

Chapter 3

Nature of the Multipole Excitations in Exotic Nuclei

In recent years, the multipole response in neutron-rich oxygen isotopes have become an attractive topic of interest, since it is directly related to many interesting phenomena in nuclei away from the valley of β stability. Weak binding of the outermost neutrons, leading to increase of the neutron radii, may form exotic ground-state structures, e.g. the halo and skin, and loosely bound nucleons could imply the appearance of the low-lying transition strength and soft collective modes of excitations, very different from the giant resonances in stable nuclei.

The neutron rich oxygen isotopes are good candidates for a possible identification of the low-lying collective soft mode, that corresponds to the oscillations of the mantle composed from excess neutrons, out of the phase with the core formed from the rest of neutrons and protons. The isovector dipole (E1) excitations in neutron rich oxygen isotopes have recently been very extensively discussed, both experimentally and theoretically.

The first systematic experimental effort, based on the electromagnetic excitations in the heavy-ion collisions, indicated the appearance of low-lying dipole strength in oxygen isotopes ^{17}O - ^{22}O [21, 96, 22]. Therein, the soft dipole excitation has been detected in all investigated neutron-rich oxygen isotopes, exhausting up to 12 % of the TRK sum rule at excitation energies below 15 MeV. More recent investigation indicated the existence of new low-lying E1 levels at 5.35 and 6.85 MeV in ^{20}O , in contrast to ^{18}O , where comparable dipole strengths in the same region have not been observed [97]. The quadrupole (E2) and octupole (E3) modes in ^{20}O , have also been studied, using elastic or inelastic proton scattering [98, 99].

There are a variety of new theoretical investigations on the subject of multipole excitations in oxygen isotopes: the large scale shell model calculations [35, 100], the self-consistent RPA with Skyrme forces [101, 102], the QRPA plus phonon coupling model [103], the time-dependent density-matrix theory [104] and the continuum RPA in coordinate-space HFB [40, 38]. In our previous investigation, we have analyzed the evolution of dipole strength distribution in a sequence ^{16}O - ^{28}O , within the relativistic RPA model with the simple filling approximation, without pairing interactions [61]. However, to study systematically the excitations in open shell nuclei, we have extended our theory

to include the pairing correlations in a self-consistent way [62].

3.1 Evolution of the Low-lying Isovector Dipole Response in Oxygen Isotopes

In the present section, we apply the RHB+RQRPA model to describe the evolution of the isovector dipole response (E1) in oxygen isotopes, when moving from ^{16}O toward the neutron drip-line, i.e. ^{24}O . The possible stability of the double magic nucleus ^{28}O is still an open question, although the isotopes ^{25}O and ^{26}O appeared experimentally unstable [105, 106]. Many theoretical investigations, as well as RHB model, predicted that the doubly magic ^{28}O is bound, in contrast to the recent measurements which demonstrated its instability [107, 108]. The shell-model calculations suggest both ^{26}O and ^{28}O to be unbound nuclei (e.g. [106]).

In the following, we compare RHB+RQRPA results on E1 excitations in oxygen isotopes with the only available systematic experimental data [22] and with the recent non-relativistic models, in particular with the continuum linear response theory based on the Hartree-Fock-Bogoliubov formalism in the coordinate space representation [40, 38]. In the model in Ref. [40] a Woods-Saxon parameterization is used to describe the single-particle potential, and a Skyrme-type density dependent delta force is adopted for the residual interaction in the ph -channel of the QRPA. Since the HFB calculation of the single-particle potential and QRPA ph -interaction is not self-consistent in Ref. [40], the interaction strength of the residual interaction was renormalized for each nuclei in order to obtain for a dipole response a zero-energy mode corresponding to the spurious center of mass motion. In the same model, the pairing interaction is included in a consistent way via a density-dependent delta force, both in the HFB pairing field for the ground state, and in the linear response equations.

On the other side, the studies based on the RHB+RQRPA calculations are fully self-consistent, i.e. the same combination of effective interactions, NL3, NL1, or NL-SH in the ph -channel and a more realistic finite range Gogny D1S interaction in the pp -channel, are used both in the RHB calculation of the ground state and as RQRPA residual interactions. The multipole strength distributions may slightly depend on the choice of the effective RMF Lagrangian in the ph -channel.

As an example to illustrate how RHB+RQRPA model depend on the RMF effective interaction, we select the neutron rich isotope ^{22}O . In Fig. 3.1 the RQRPA strength distribution function for the isovector dipole operator (2.35) is displayed. The results are plotted for three different parameterizations of the mean field Lagrangian, listed in Table(1.1): NL-SH, NL1 and NL3. The set of parameters for the pairing correlations D1S is fixed to the values from Table(1.2). Although there are some variations in the response for different effective forces, it is important to notice that the main excitation properties, i.e. the energy of the giant resonance (around 20 MeV) and the low-lying structure (below 10 MeV) are well preserved. This issue is carefully checked throughout the chart of nuclides. Therefore, in the following investigation we restrict our calculations mainly to a single, presumably the best effective force. An appropriate choice would be the NL3

effective interaction. In most applications of the RHB model, the NL3 effective interaction [80] has been used for the RMF effective Lagrangian. Properties calculated with NL3 indicate that this is probably the best nonlinear effective interaction so far, not only for the stable nuclei, but also in the regions away from the line of β -stability [80, 43, 44, 47]. Unless it is specifically stated, we adopt only the NL3+D1S parameterization in the following calculations.

The importance of a consistent treatment of pairing correlations in the HFB+QRPA framework has been emphasized in Refs. [40, 38]. In general, the residual pairing interaction in the QRPA generates pronounced dynamical correlation effects in the response through pair density fluctuations. Moreover, as we have shown in the previous chapter, the energy weighted sum rules are only satisfied if the pairing interaction is consistently included both in the static HFB and in the dynamical linear response.

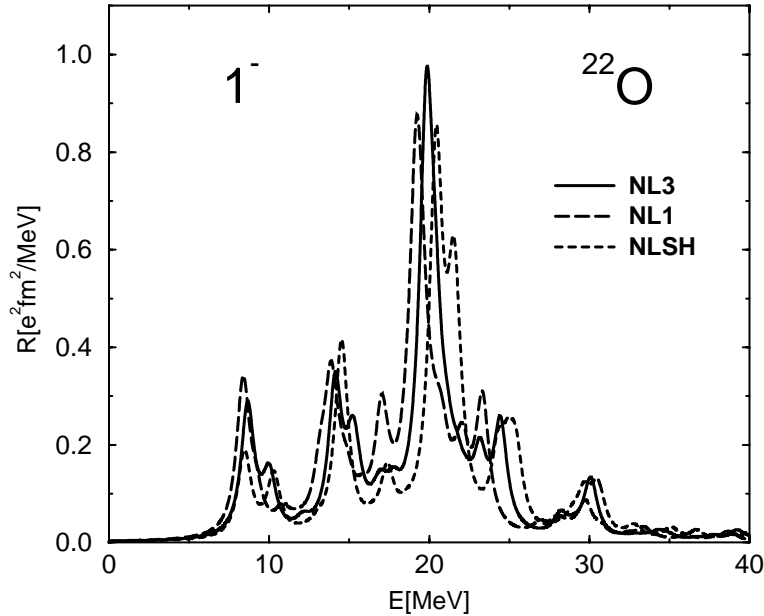


Figure 3.1: Isovector dipole strength distributions in ^{22}O calculated with the NL3 (solid), NL1 (long-dashed) and NL-SH (dashed) effective interactions

The strength distributions in Fig. 3.1 are obtained in a fully self-consistent calculation. When this condition is fulfilled, a large configuration space enables the separation of the zero-energy mode that corresponds to the spurious center of mass motion. In the present calculation with NL3+D1S parameterization, for ^{22}O this mode, orthogonal to other physical states, is located at $E = 0.04$ MeV. In many nonrelativistic QRPA models (e.g. Refs. [40, 38, 103]) which do not have this property, the spurious center of mass state was projected out by renormalizing a few percent the matrix elements of the residual interaction. With this method, the spurious state can be pushed toward the zero energy. On the other hand, in the self-consistent RHB+RQRPA model the residual interaction

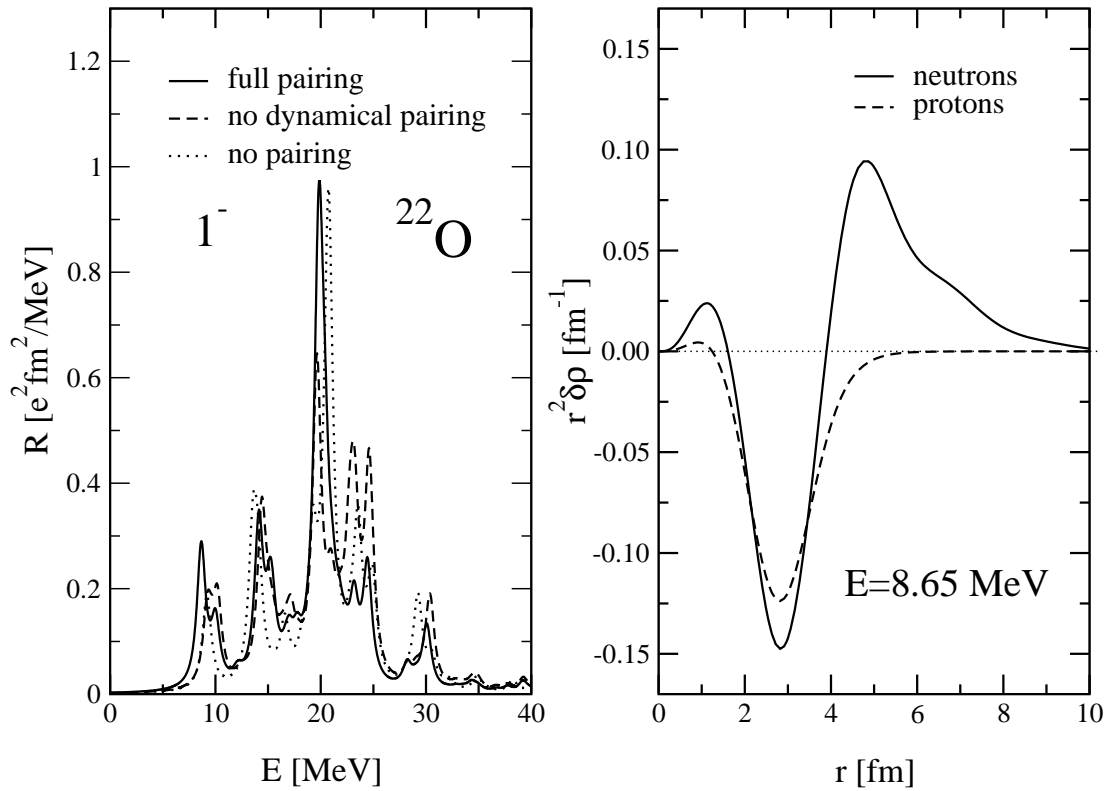


Figure 3.2: The isovector strength function of the dipole operator in ^{22}O (left). The fully self-consistent RHB+RQRPA response (solid line) is compared with the RMF+RRPA calculation without pairing (dotted line), and with the RHB+RRPA calculation that includes pairing correlations only in the ground state (dashed line). The proton and neutron transition densities for the peak at $E = 8.65 \text{ MeV}$ are shown in the right panel.

is strictly fixed throughout the periodic chart; in the case when the configuration space is large enough, the spurious center of mass state clearly separates (see Fig. 2.1). This is not the case if the pairing correlations are not included in the residual interaction in a consistent way.

The pairing effects to the isovector dipole response in ^{22}O are displayed in the left panel of Fig. 3.2. In this example we also compare the results of the RMF+RRPA calculations without pairing, with pairing correlations included only in the RHB ground state (no dynamical pairing), and with the fully self-consistent RHB+RQRPA response. The strength functions shown in Fig. 3.2 illustrate the importance of including pairing correlations in the calculation of the isovector dipole response. Pairing is, of course, particularly important for the low-lying strength below 10 MeV. The inclusion of pairing correlations in the full RHB+RQRPA calculation enhances the low-energy dipole strength near the threshold.

To study the low-lying strength in more details, we display in the right panel of Fig. 3.2 the proton and neutron transition densities (2.38) for the main peak in the low-energy region ($E = 8.65 \text{ MeV}$). In contrast to the well known radial dependence of the IVGDR transition densities (proton and neutron densities oscillate with opposite phases), the proton and neutron transition densities for the main low-energy peak are in

phase in the nuclear interior. Furthermore, there is no contribution from the protons in the surface region, and the strong neutron transition density displays a long tail in the radial coordinate. A similar behavior has been predicted for the light neutron halo nuclei ${}^6\text{He}$, ${}^{11}\text{Li}$ and ${}^{12}\text{Be}$ in Ref. [109], where it has been shown that the long tails of the wave functions of the loosely-bound neutrons are responsible for the different radial dependence of the transition densities that correspond to the soft low-energy states as compared to those of the giant resonances.

The effect of pairing correlations on the isovector dipole response in ${}^{22}\text{O}$ is very similar to the one obtained in the HFB+QRPA framework (Fig. 8 of Ref. [38]). In the low-energy region below 10 MeV, however, the pairing interaction used in the QRPA calculation produces a much stronger enhancement of the dipole strength, as compared to the results shown in Fig. 3.2. The reason probably lies in the choice of the pairing interaction. While we use the volume Gogny pairing, in Ref. [38] a density-dependent delta force was used in the pp channel. This interaction is surface peaked and therefore produces a stronger effect on the low-energy dipole strength near the threshold.

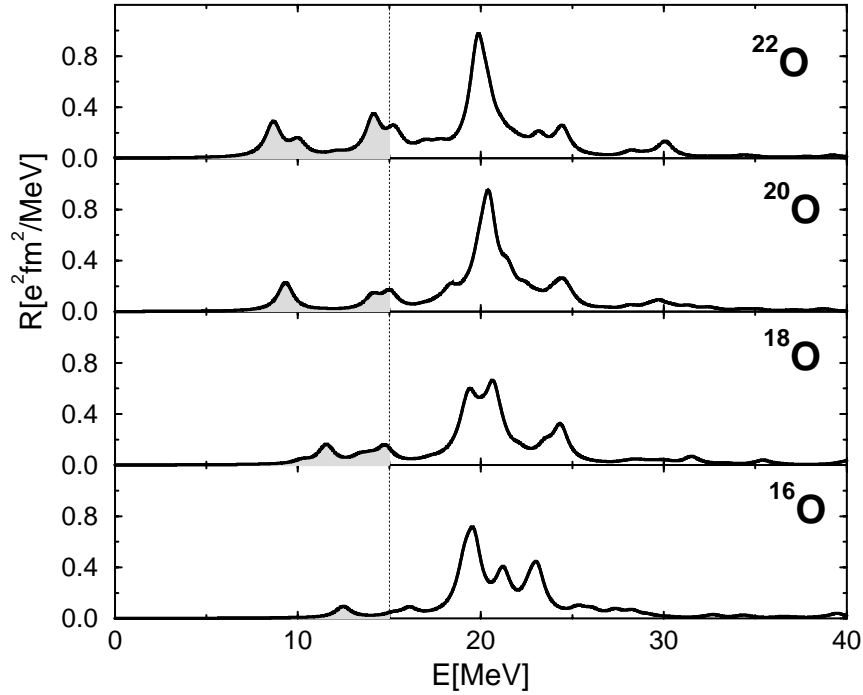


Figure 3.3: Evolution of the isovector dipole strength distribution in oxygen isotopes, calculated with the NL3 effective interaction. The low-lying region is separated by the dashed line at $E=15$ MeV in order to compare results with Ref. [22]

In the following, we use the self-consistent RHB+RQRPA model to study how the isovector 1^- response evolve as a function of a neutron number in oxygen isotopes. The corresponding strength distributions for ${}^{16}\text{O}$, ${}^{18}\text{O}$, ${}^{20}\text{O}$ and ${}^{22}\text{O}$ are displayed in Fig. 3.3. Already for the ${}^{16}\text{O}$ the isovector dipole strength distribution is strongly fragmented with

the centroid energy (2.57) at $\bar{E}=21.8$ MeV. The thin dashed line tentatively separates the region of giant resonances from the low-energy region below 15 MeV to compare the properties of the low-lying strength with the experimental results in Ref. [22]. As the number of neutrons increases, two main effects are observed: a) an increased fragmentation of the dipole strength, and b) the appearance of low-lying strength below 15 MeV. The relative contribution of the low-energy region increases with the neutron excess (shaded area in Fig. 3.3), exhausting 12, 10, 17 and 22 % of the TRK sum rule in ^{18}O , ^{20}O , ^{22}O and ^{24}O , respectively.

A similar result was also obtained with the non-relativistic models. In the Hartree-Fock plus RPA framework with Skyrme effective interactions [33] for ^{28}O , several peaks appeared in the region between 6 and 10 MeV. The Woods-Saxon + continuum Skyrme QRPA showed also significant development of the dipole strength below 15 MeV, exhausting 7,11,16,21 % of the TRK sum rule value for ^{18}O - ^{24}O [38]. The same dipole strengths calculated in the large scale shell model exhaust about 10% TRK in oxygen isotopes heavier than ^{18}O [35]. In the recent QRPA plus phonon coupling model, the important role of the coupling with phonons has been pointed out and its role to increase the low-lying strength, exhausting between 5 and 10% of the TRK sum rule [103]. The summary

Oxygen isotope A =	18	20	22	24
RHB+RQRPA(NL3)	0.12	0.10	0.17	0.22
continuum QRPA [38]	0.07	0.11	0.16	0.21
Shell model [100]	0.06	0.11	0.10	0.09
QRPA + phonon coupling (large gap) [103]	0.07	0.09	0.07	
Experiment GSI [22]	0.08	0.12	0.07	
Experiment [110]	0.11			

Table 3.1: Integrated dipole strength up to 15 MeV excitation energy, given in units of the classical TRK sum rule, in oxygen isotopes A=18-24. The results of RHB+RQRPA model are compared with the recent theoretical and experimental studies.

of recent results on the low-lying dipole strength below 15 MeV for oxygen isotopes in different models are shown in Table 3.1.

The first systematic experimental study of giant resonances and soft modes in exotic oxygen nuclei has been recently completed at GSI, where the dipole response of neutron rich oxygen isotopes is measured up to ^{22}O [22]. The experimental approach is based on the electromagnetic excitation of fast projectiles by Pb target, where the radioactive oxygen beams are produced in fragment separation of a primary ^{40}Ar beam. The dipole strength function is extracted from a measurement of the differential electromagnetic dissociation cross section. Since the energy of a secondary beam amounts up to 600 MeV/nucleon, dipole transitions up to 30 MeV in excitation energy have been reached in exotic nuclei. In this experimental investigation, the low-lying dipole strength exhausting up to 12% of the TRK sum rule, was observed for ^{18}O , ^{20}O and ^{22}O . Further experimental study of the drip line nucleus ^{24}O is planned in the near future. The theoretical predictions are in reasonable agreement with experiment (Table 3.1). Although all models agree on the overall effect on the 1^- transition strength, as the number of neutrons increases,

some quantitative differences have been noted. In Fig. 3.4 we display the RHB+RQRPA

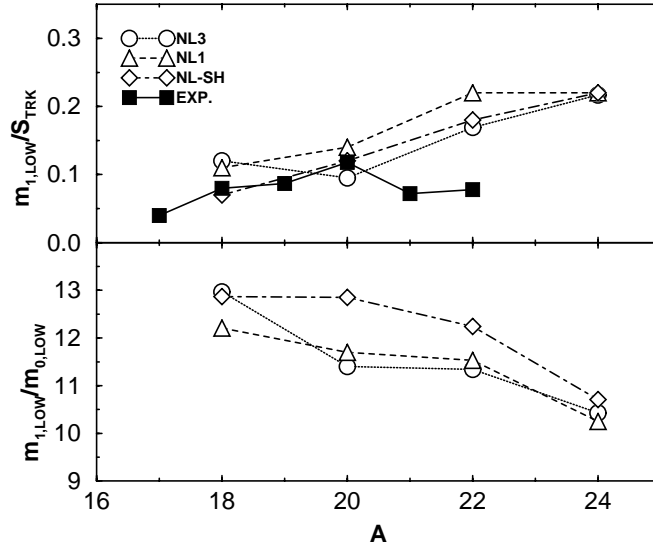


Figure 3.4: The properties of the low-lying 1^- strength distribution: evolution of the low-lying energy weighted sum up to 15 MeV divided by the classical TRK sum rule (upper panel) is compared to the experimental results from Ref. [22]. The centroid energy (2.57) of the low-lying dipole strength is plotted in the lower panel.

low-lying EWSR ($E < 15$ MeV) in the bound oxygen isotopes, compared with the GSI experimental results [22]. Accordingly we emphasize that the RHB+RQRPA results for the low-lying dipole strength distribution in ^{18}O and ^{20}O are in good agreement with the experimental data. The RHB+RQRPA model, as well as the continuum QRPA [38] slightly overestimate the experimental and other theoretical low-lying EWSR in ^{22}O . For better understanding of this discrepancy, it would be very helpful to have the experimental study of the drip line nucleus ^{24}O . In the lower panel of Fig. 3.4 we plot the centroid energy (2.57) of the low-lying strength (up to 15 MeV) in ^{18}O - ^{24}O . As we move toward the neutron drip line, the corresponding centroid energy lowers its position.

What is the nature of the low-lying isovector dipole states? The question of whether the soft, i.e. low-lying dipole excitations are collective or single-particle has been addressed, for example, in Ref. [111] for the light neutron halo nuclei ^{11}Li and ^{11}Be . It has been shown that the soft modes, which result from the large spatial extension of the bound single-particle states, represent a new type of non-resonant independent single-particle excitations. The narrow width and the large transition strength, which characterize these excitations, are not caused by a coherent superposition of particle-hole (ph) configurations like in collective states.

In the present investigation of the oxygen isotopes, we analyze in more detail the structure of the main peaks in the low-energy region of the isovector dipole strength distribution. For a simplicity, we consider here only the closed shell nucleus ^{28}O , where the RQRPA limit is the relativistic RPA (RRPA), built on the simple particle (and antiparticle)-hole configuration space. For a state at energy ω_ν , the contribution of a particular proton

or neutron ph configuration is determined by the RHPA amplitude

$$\xi_{\bar{p}h} = |X_{\bar{p}h}^v|^2 - |Y_{\bar{p}h}^v|^2, \quad (3.1)$$

where X^v and Y^v are the eigenvectors of the RHPA equation, for which the normalization condition holds,

$$\sum_{\bar{p}h} \xi_{\bar{p}h} = 1. \quad (3.2)$$

In the low-energy region of IV dipole strength for ^{28}O , the neutron ph excitations have

E[MeV]	EWSR[%]	neutron $p - h$ configuration
4.2	0.9	(92% $1d_{3/2} \rightarrow 2p_{3/2}$)
4.9	1.4	(91% $1d_{3/2} \rightarrow 2p_{1/2}$) (6% $1d_{3/2} \rightarrow 2p_{3/2}$)
7.3	1.9	(92% $2s_{1/2} \rightarrow 2p_{3/2}$)
8.9	6.3	(71% $1d_{3/2} \rightarrow 1f_{5/2}$) (16% $1d_{5/2} \rightarrow 1f_{7/2}$) (3% $1d_{5/2} \rightarrow 2p_{3/2}$)

Table 3.2: The structure of the main peaks in the low-energy region of the isovector dipole strength distribution in ^{28}O . For each energy below 10 MeV (left column), which exhausts a certain percentage of EWSR integrated up to 50 MeV, the neutron particle-hole configurations with largest amplitudes are displayed in the right column. The percentage of EWSR assigned to a particular $p - h$ configuration refers to the normalization of the RHPA amplitudes (3.2).

dominant contributions. The strength function below 10 MeV is slightly fragmented into several different peaks. The main neutron ph components in the RHPA wave function of the states at 4.2 MeV, 4.9 MeV, 7.3 MeV and 8.9 MeV, are displayed in Table 3.2. The isovector dipole response in the low-energy region below 10 MeV is mainly characterized by one dominating single particle transition, with an additional or a few other transitions with small contributions, in contrast to the coherent superposition of many ph configurations, which characterizes the excitations in the region of the collective modes, i.e. the giant resonances. Similar property remains in the open shell nuclei; although the pairing effects increase the collectivity of the low-lying states, a single 2qp configuration dominates in their RQRPA wave function.

The nature of the low-lying isovector dipole states, and of the states in the region of giant resonances changes considerably as one moves away from the valley of the β -stability towards the drip-lines. On the left side of Fig. 3.5 we display the transition densities (2.38) for the GDR states 19.6 MeV in ^{16}O and 19.3 MeV in ^{24}O . The transition densities for the low-lying states 8.7 MeV in ^{22}O and 7.3 MeV in ^{24}O are plotted on the right side of Fig. 3.5. The proton $\delta\rho_p$ (dashed) and neutron $\delta\rho_n$ (dot-dashed) transition densities are shown separately. The isovector and isoscalar transition densities, defined as

$$\delta\rho_{IV} = \delta\rho_p - \delta\rho_n \quad (3.3)$$

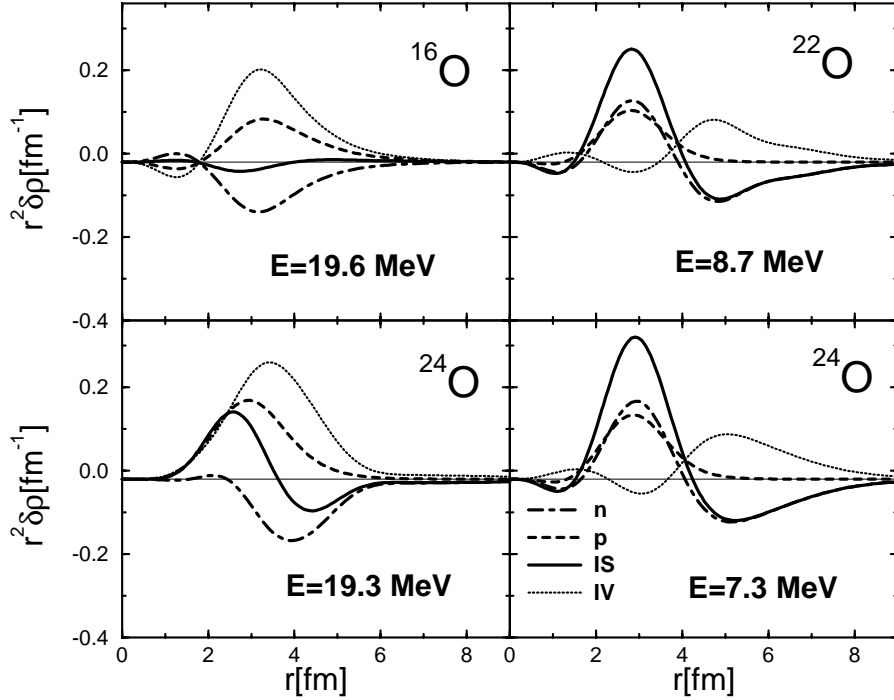


Figure 3.5: Transition densities for the GDR peaks at 19.6 MeV in ^{16}O , 19.3 MeV in ^{24}O , and for the low-lying states at 8.7 MeV in ^{22}O , 7.3 MeV in ^{24}O . Both the isoscalar and isovector transition densities are displayed, as well as the separate proton and neutron contributions.

$$\delta\rho_{IS} = \delta\rho_p + \delta\rho_n \quad (3.4)$$

are plotted with the dotted and solid lines, respectively. The transition densities of the GDR state at 19.6 MeV in ^{16}O display the radial dependence characteristic for the isovector giant dipole resonance: the proton and neutron densities oscillate with opposite phases; the amplitude of the isovector transition density is much larger than that of the isoscalar component. In the stable $N=Z=8$ nucleus, the isoscalar transition density almost completely vanishes [112]. Very small RHPA isoscalar contributions, obtained in ^{16}O , are due to the isospin symmetry breaking. On the other side, the transition densities in the drip line nuclei display a different behavior. Although the transition densities of the GDR state at 19.3 MeV in ^{24}O have the usual IVGDR radial dependence, there is an important difference with respect to the stable nuclei: the isoscalar transition density increases progressively, and at large radii both the isovector and isoscalar transition densities have a similar radial dependence. We notice that the large neutron component in the surface region contributes to the formation of a node for the isoscalar transition density. In Ref. [33, 112] it has been shown that this effect is characteristic for neutron rich nuclei. However, the most important effects on dipole excitations in exotic nuclei are identified in the low-lying states. The transition densities for the peaks at 8.7 MeV in ^{22}O and

at 7.3 MeV in ^{24}O are displayed on the right side of Fig. 3.5. These states exhibit a rather different radial dependence to the GDR: the proton and neutron densities in the interior region are not out of phase; there is almost no contribution from the protons in the surface region. The isoscalar transition density dominates over the isovector one in the interior region of nuclei, while the neutron transition density is much more extended in the radial coordinate as compared to the transition densities of the giant resonance states. We notice that a similar behavior of transition densities have been predicted for excitations in halo nuclei ^6He , ^{11}Li and ^{12}Be in Ref. [109]. It has been shown that the long tails of the wave functions of the loosely-bound neutrons are responsible for the different radial dependence of the soft low-energy states and the giant resonances.

The studies of possible low-lying excitation modes in neutron rich nuclei might help in the future to get a better insight in the new structural phenomena in exotic nuclei. In particular, recently it has been suggested that the magic numbers are different in light drip-line nuclei, in comparison to the nuclei within the valley of β stability. The creation of a new magic number $N = 16$ was reported for nuclei with $Z \leq 8$, close to the neutron drip-line [113]. Recent investigation with inelastic proton scattering on $^{10,12}\text{Be}$ indicated that the $N=8$ Be isotope cannot be treated as a singly closed-shell nucleus, i.e. possible existence of an intruder orbital $2s_{1/2}$ would imply new magicity [114]. As was pointed out in Ref. [100], the melting of the shell structure in exotic nuclei would create very low-energy E1 strength, which would reflect the possible onset of new magic numbers.

3.2 Pairing Effects on the Quadrupole Response in Drip-line Nuclei

The giant quadrupole resonances (GQR) are rather well established collective modes in atomic nuclei. In particular, the isoscalar ($T = 0$) giant quadrupole resonance $J^\pi = 2^+$ (ISGQR) has been extensively studied in the last decades, resulting in an excellent agreement amongst different experimental (e.g. electron and hadron scattering, particle capture reactions) and theoretical (time-dependent Hartree Fock, RPA, time dependent RMFT, RRPA, etc.) investigations. The mass number dependence of the excitation energy for the ISGQR, extracted from experiment, is given by the approximative law $E(A) \approx 65A^{-1/3} \text{ MeV}$ [115]. Some experimental data are also available for the isovector ($T = 1$) GQR.

However, in nuclei far away from the valley of β stability, the exotic nuclear structure of loosely bound nucleons may strongly affect the overall quadrupole response. In recent studies, the low-lying 2^+ states in the neutron rich oxygen isotopes have been investigated in the self-consistent Skyrme Hartree-Fock-BCS + QRPA, showing that the neutron to proton transition amplitudes for low-lying states differ noticeably from the simple N/Z estimate [102, 99]. The actual experiments constrained the position of the first 2^+ state in ^{22}O at 3.2 MeV [116]. Since this is higher than the corresponding energy in ^{20}O , and for nuclei close to the stability there is no strong variation in the energy of the first 2^+ state, it has been suggested in Ref. [102] that the latest result might also be a fingerprint of the shell structure changes in exotic nuclei. In the continuum QRPA

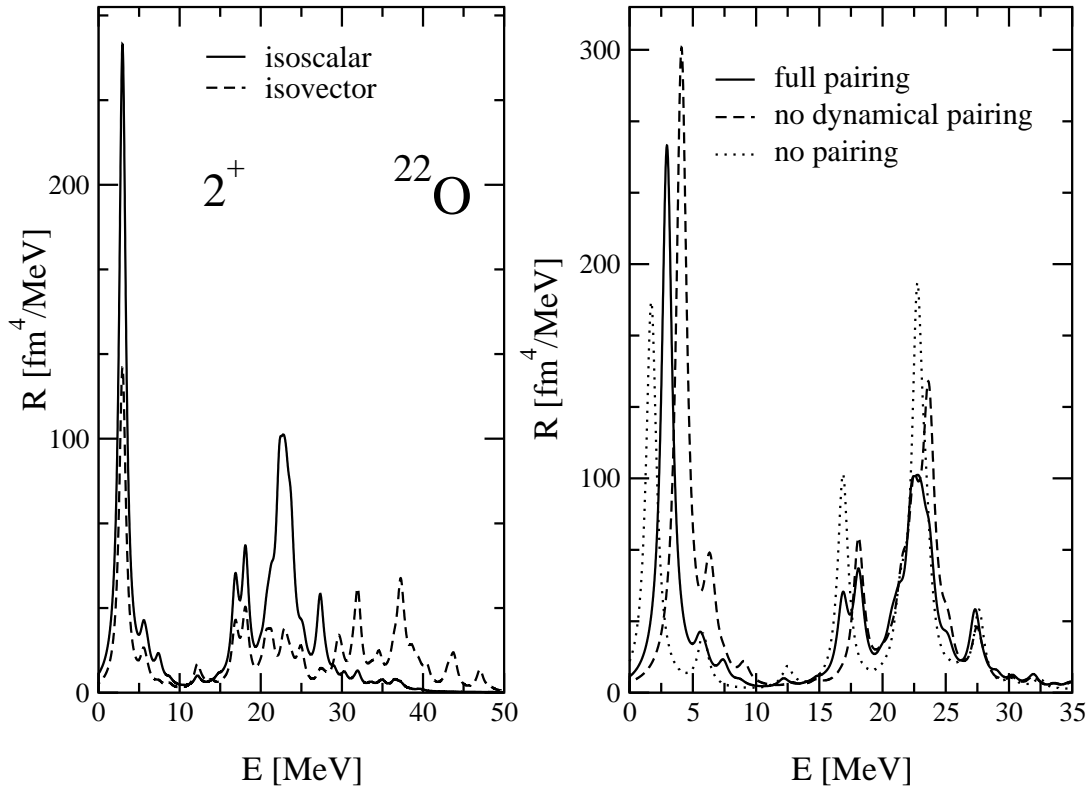


Figure 3.6: Isoscalar and isovector quadrupole strength distribution in ^{22}O (left panel). In the right panel the full RHB+RQRPA isoscalar strength function (solid) is compared to the RMF+RRPA calculation without pairing (dotted), and with the response obtained when the pairing interaction is included only in the RHB ground state (dashed).

calculations, the quadrupole response in oxygen isotopes has been examined with respect to the self-consistency of the density-dependent delta force in the pairing channel of HFB+QRPA model [40, 38]. Following this investigation, we study the pairing effects on the 2^+ response in RHB+RQRPA model. In order to evaluate the quadrupole strength distributions, the multipole transition operators (2.31) and (2.32) for $J=2$ are used to describe the isoscalar and isovector quadrupole excitations, respectively. In the left panel of Fig. 3.6 we display the RHB+RQRPA isoscalar and isovector quadrupole ($J^\pi = 2^+$) strength distributions in ^{22}O . The low-lying $J^\pi = 2^+$ state is located at $E = 2.95$ MeV, and this value should be compared with the experimental excitation energy of the first 2^+ state: 3.2 MeV [116]. The strong peak at $E = 22.3$ MeV in the isoscalar strength function corresponds to the isoscalar giant quadrupole resonance (IS GQR). The isovector response, on the other hand, is strongly fragmented, and distributed over the large region of excitation energies $E \simeq 18 - 38$ MeV.

The effect of pairing correlations on the isoscalar response is illustrated in the right

panel of Fig. 3.6, where the full RHB+RQRPA strength function is compared to the RMF+RRPA calculation without pairing, and with the response obtained when the pairing interaction is included only in the RHB ground state (no dynamical pairing). As one would expect, the effect of pairing correlations is not especially pronounced in the giant resonance region. The inclusion of pairing correlations, however, has a relatively strong

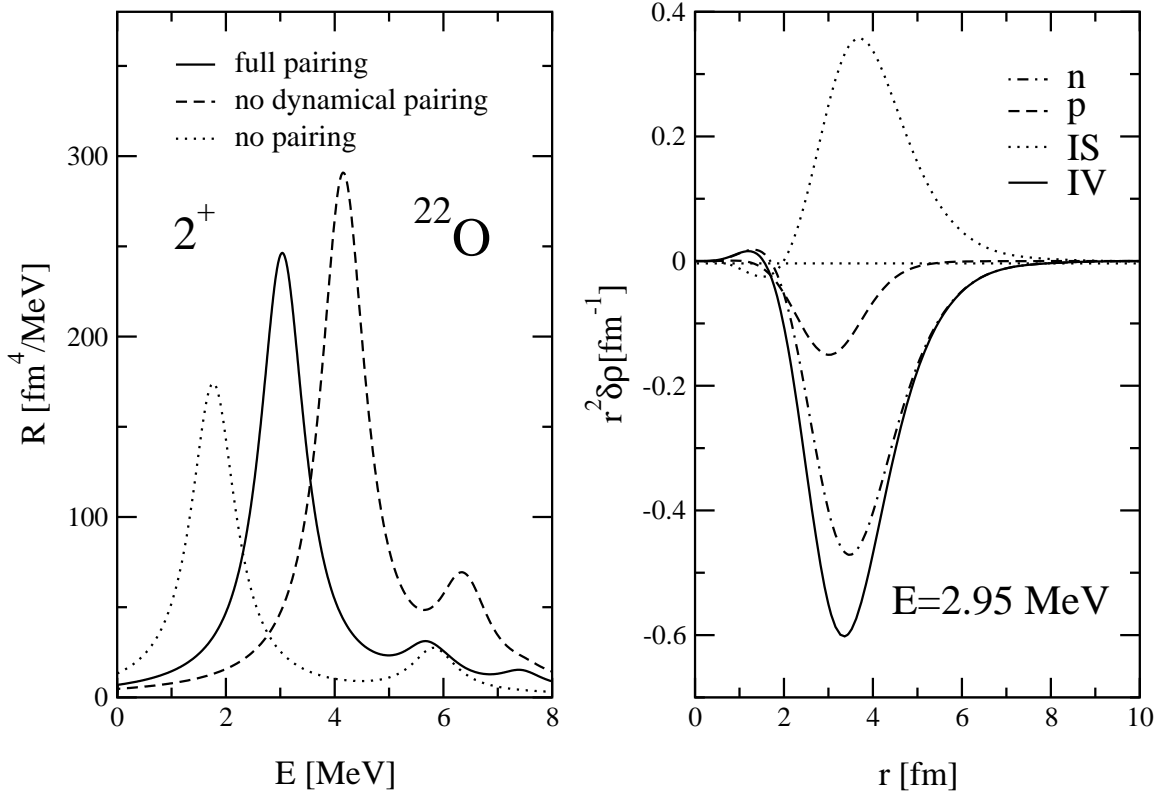


Figure 3.7: Low-energy portion of the isoscalar quadrupole strength distribution in ^{22}O (left). Radial neutron, proton, isoscalar (IS), and isovector (IV) transition densities for the $J^\pi = 2^+$ state at $E = 2.95$ MeV (right).

effect on the low-lying 2^+ state. This is seen more clearly in the left panel of Fig. 3.7, where only the low-energy portion of the isoscalar strength distributions in ^{22}O is shown. With respect to the RRPA calculation, the inclusion of the pairing interaction in the static solution for the ground state increases the excitation energy of the lowest 2^+ state by ≈ 3 MeV. The fully self-consistent RHB+RQRPA calculation lowers the excitation energy from ≈ 4.5 MeV to $E = 2.95$ MeV. Therefore, we conclude that the pairing effects are of a particular importance for complete understanding of the low-lying quadrupole modes in exotic nuclei. The inclusion of pairing correlations increases the collectivity of the low-lying 2^+ state. A very similar result for the low-lying quadrupole state in ^{24}O has

been obtained in the HFB+QRPA calculations. [38].

The structure of the low-lying 2^+ states can be identified by analyzing the corresponding transition densities. The proton, neutron, isoscalar and isovector transition densities for 2^+ state at $E = 2.95$ MeV are shown in the right panel of Fig. 3.7. Both the neutron and proton transition densities are peaked in the surface region, but the neutron transition density is more pronounced, and radially extended. Since the neutron contribution to transition densities dominates, both the isoscalar and isovector transition densities increase in neutron rich nuclei. Due to the presence of the neutron skin, the isovector and isoscalar modes are mixed and participate in all excited states [33]. To

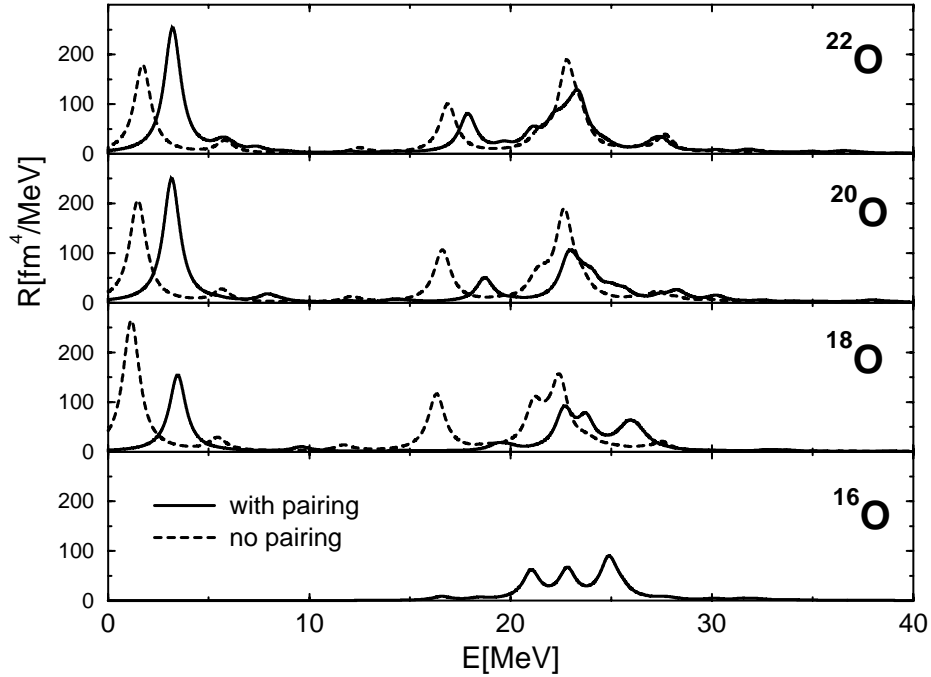


Figure 3.8: Isoscalar quadrupole strength distribution in oxygen isotopes, with self-consistent pairing (solid) and without pairing (dashed).

investigate the effect of the neutron excess on the ISGQR in the isotope chain, in Fig. 3.8 we display the evolution of the quadrupole strength distributions in ^{16}O - ^{22}O . We evaluate separately the response within the RMFT+RRPA model without pairing interaction, in comparison with the RHB+RQRPA framework which includes the pairing in a consistent way. Obviously, in the limit $N=Z=8$, the RHB+RQRPA corresponds exactly to the RMFT+RRPA scheme. In this case, the isovector and isoscalar strength distributions are well separated, describing pure isoscalar or isovector excitations [28]. As the number of neutrons increases, the isoscalar strength becomes more fragmented, and the isovector strength gains strong contribution exactly in the same low-lying region with a strong isoscalar strength (left panel in Fig. 3.6). Of course, the pairing correlations in all open-shell oxygen isotopes play an important role; although they have small influence to the GQR peaks, the low-lying modes are in general strongly affected. In Table 3.3 we

Oxygen isotope A =	18	20	22	24
RHB + RQRPA(NL3)	3.45	3.16	2.95	3.55
continuum QRPA [38]	4.2	4.1	4.5	5.0
HF-BCS + QRPA (SGII) [102]	≈ 4.1	≈ 3.7	≈ 4.9	
continuum QRPA [41]	3.2	2.3	1.9	4.0
SM-USD [117]			3.38	
Experiment [118, 116]	≈ 2.0	≈ 1.7	3.2	

Table 3.3: Energies of the low-lying 2^+ state in oxygen isotopes (in MeV). The results of RHB+RQRPA model are compared with other recent investigations.

compare the RHB+RQRPA energies of the low-lying mode with available theoretical and experimental results. The experimental data originate from the electromagnetic processes based on Coulomb excitation and γ decay life-time measurements. Recently, the structure of neutron rich light nuclei around $N=20$ has been investigated by using in-beam γ spectroscopy for fragmentation reactions [116]. For the first time, the γ spectra has been obtained in ^{22}O , indicating that the line at 3.2 MeV represents 2^+ to 0^+ transition. Theoretical predictions in general slightly overestimate the measured excitation energies of the first 2^+ state. The RHB+RQRPA results for the 2^+ excitations are in agreement with non-relativistic QRPA calculations of the quadrupole response in neutron rich oxygen isotopes [102, 99, 38, 41]. The existence of a spherical shell effect at $N=14$, i.e. a rapid increase of the 2^+ energy which has been experimentally confirmed (Table 3.3), however, is not yet fully understood within the theoretical descriptions.

3.3 Giant Resonances in Medium Light Neutron Rich Nuclei

Next we move to the calcium isotope chain, to investigate the effects of neutron excess to the electric multipole response that have been recently studied in high resolution nuclear resonance fluorescence (NRF) [119] and in heavy ion scattering experiments [120]. Starting from ^{40}Ca five stable even-even isotopes exist; they are different only on the number of neutrons in the $1f_{7/2}$ orbital. By subsequent filling of $2p_{3/2}$, $2p_{1/2}$, and $1f_{5/2}$ orbitals, we get the isotope ^{60}Ca which may be experimentally accessible in the future. It appears to be located inside the neutron drip line, presenting a good example of a nucleus with a very large proton-neutron asymmetry, leading to interesting nuclear structure phenomena.

The isovector dipole strength distributions for ^{40}Ca , ^{48}Ca , ^{54}Ca and ^{60}Ca nuclei are plotted in Fig. 3.9. As the neutron excess increases, the spectra become more fragmented, and already beyond ^{50}Ca , the onset of low-lying dipole strength is observed in the region of excitation energies below 10 MeV. This result is in agreement with the non-relativistic HF+RPA calculations of Ref. [33]. Although no dipole strength is found below 10 MeV for ^{48}Ca , the strength distribution is slightly more fragmented than in ^{40}Ca , with small contributions from neutrons in $1f_{7/2}$ orbital. In the strength function of the extremely neutron rich nucleus ^{60}Ca , the low-energy region is strongly fragmented, with many peaks

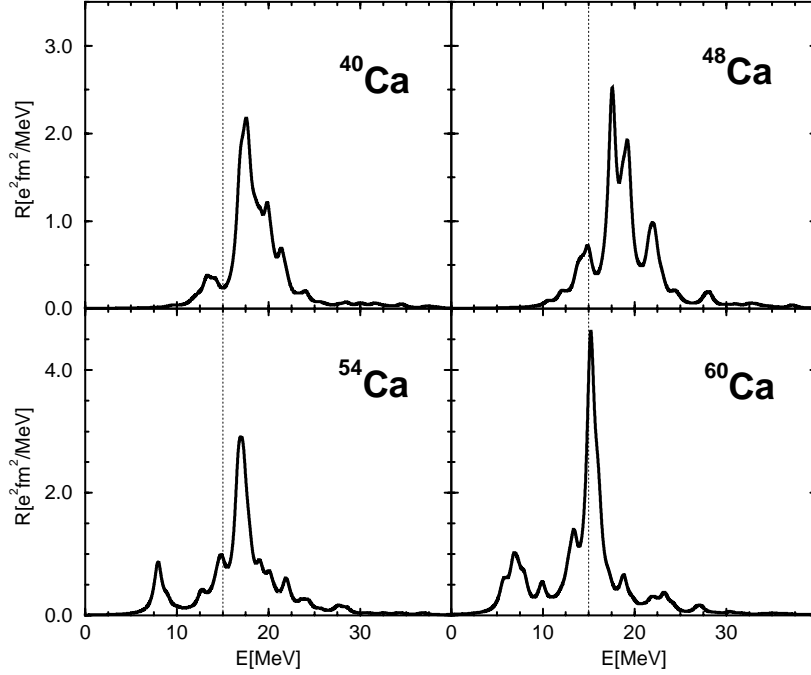


Figure 3.9: Isovector dipole strength distribution in calcium isotopes.

of similar intensity. Together, they exhaust 10% of the EWSR (integrated up to 50 MeV), compared to the 40% of the EWSR exhausted by the main IV GDR peak at 15.2 MeV. The neutron ph configurations with the largest amplitudes in the RPA wave functions of several low-lying dipole states in ^{60}Ca are listed in Table 3.4. We notice that one, or at most two neutron ph configurations determine the structure of the low-energy peaks. There is practically no contribution from proton ph excitations. This structure is very different from that of the GDR peak, which is characterized by a coherent superposition of many, both proton and neutron ph configurations. The largest single neutron ph configuration contributes less than 20% of the total intensity, and the ratio of the neutron to proton contribution $61.8\%/36.7\%=1.7$ is close to the value N/Z , as expected for an IV GDR state.

The RQRPA transition densities for the state at 7.3 MeV (illustrative for the low-energy region) and for the GDR state at 15.2 MeV, are compared in Fig. 3.10. The transition densities display similar radial dependence to the one already discussed for the oxygen isotopes. In particular, we notice the long tail of the neutron transition density for the low-lying state at 7.3 MeV.

Our result for ^{48}Ca , i.e. no dipole strength below 10 MeV, is at variance with the onset of soft dipole resonances in Ca isotopes, calculated in the framework of density functional theory [32]. For $^{42,44,46,48}\text{Ca}$, in addition to several narrow peaks which are derived from single particle dipole transitions, a broad resonance was found in the energy range between 5 MeV and 10 MeV. It was interpreted as evidence of a collective excitation:

Table 3.4: Same as in Table 3.2, but for the main peaks in the low-energy region of the isovector dipole strength distribution in ^{60}Ca .

E[MeV]	EWSR[%]	neutron $p - h$ configuration
5.7	1.2	(93.1% $2p_{1/2} \rightarrow 3s_{1/2}$) (3.6% $1f_{5/2} \rightarrow 2d_{5/2}$)
6.8	2.6	(82.8% $1f_{5/2} \rightarrow 2d_{3/2}$) (6.1% $1f_{5/2} \rightarrow 2d_{5/2}$) (3.1% $1f_{7/2} \rightarrow 1g_{9/2}$) (2.3% $2p_{3/2} \rightarrow 2d_{5/2}$) (1.1% $2p_{3/2} \rightarrow 3s_{1/2}$)
7.3	1.6	(49.3% $2p_{1/2} \rightarrow 2d_{3/2}$) (41.3% $2p_{3/2} \rightarrow 3s_{1/2}$) (3.2% $1f_{5/2} \rightarrow 2d_{3/2}$) (1.5% $2p_{3/2} \rightarrow 2d_{5/2}$)
7.9	2.0	(83.8% $2p_{3/2} \rightarrow 2d_{5/2}$) (5.7% $1f_{5/2} \rightarrow 2d_{3/2}$) (3.5% $1f_{7/2} \rightarrow 1g_{9/2}$) (2.4% $1f_{5/2} \rightarrow 1g_{7/2}$)
9.9	2.1	(57.7% $1f_{5/2} \rightarrow 1g_{7/2}$) (22.0% $1f_{7/2} \rightarrow 1g_{9/2}$) (3.3% $1f_{7/2} \rightarrow 2d_{5/2}$)

surface neutron density oscillating against a stable ^{40}Ca core.

There is also recent experimental evidence on low-energy dipole strength in ^{48}Ca . Although in experiments with heavy ion reactions $^{40,48}\text{Ca}(^{86}\text{Kr}, ^{86}\text{Kr}')^{40,48}\text{Ca}^*$ non-negligible E1 strength in the low-energy region was detected, no difference in low-lying strength was found in the comparison of ^{40}Ca and ^{48}Ca spectra [120]. The energy resolution of this experiment was insufficient to detect precisely if the measured low-lying strength in ^{48}Ca have some collective properties that could be related to the pygmy resonance, i.e. the soft E1 mode composed from the $1f_{7/2}$ neutrons oscillating out of phase with the ^{40}Ca core, as it was suggested in Ref. [32]. In contrast to experiment in Ref. [120], recent results [119] of high resolution photon scattering experiments indicate significant onset of low-lying dipole strength in ^{48}Ca . It was found that the sum of the B(E1) strength in the energy region between 5 MeV and 10 MeV is about 10 times larger than in ^{40}Ca . In the same region the E1 strength in ^{48}Ca exhausted 0.3 % of the EWSR, in contrast to Ref. [120] where the exhausted energy weighted strength between 6 and 10 MeV is a factor 20 larger. The low-lying E1 excitation measured around 7 MeV, which originates from a two-phonon structure $2^+ \otimes 3^-$, is beyond the scope of the present RQRPA model which is built only on the 2qp configuration space.

In the following we proceed with the RQRPA analysis of the evolution of the isovector dipole response towards medium heavy nuclei. In Fig. 3.11 the self-consistent ground-

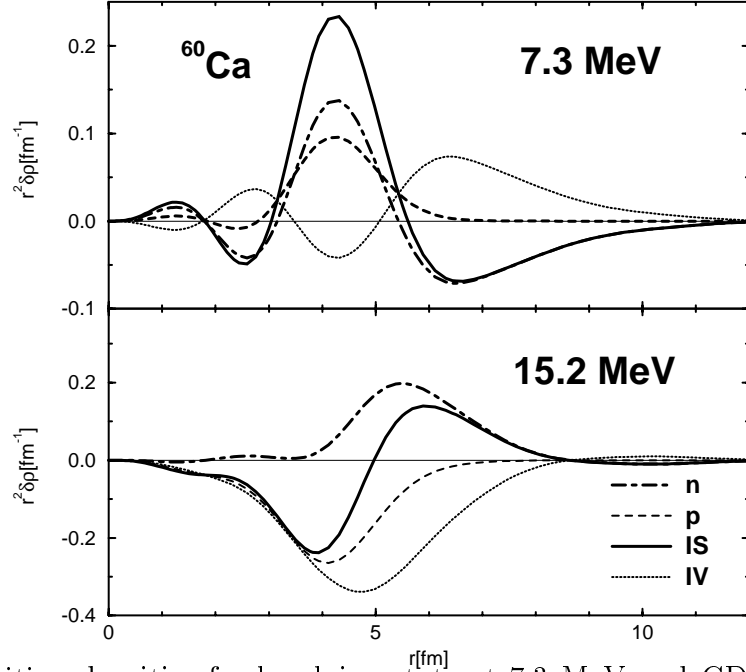


Figure 3.10: Transition densities for low-lying state at 7.3 MeV and GDR state at 15.2 MeV for ^{60}Ca .

state neutron densities for Ni nuclei are plotted. The density profiles display shell effects in the bulk and a gradual increase of neutron radii. In the insert of Fig. 3.11, the corresponding values for the surface thickness and diffuseness parameter have been included. The surface thickness t is defined to be the change in radius required to reduce $\rho(r)/\rho_0$ from 0.9 to 0.1 (ρ_0 is the maximal value of the neutron density; because of shell effects one could not use for ρ_0 the density in the center of the nucleus). The diffuseness parameter α is determined by fitting the neutron density profiles to the Fermi distribution

$$\rho(r) = \rho_0 \left(1 + \exp\left(\frac{r - R_0}{\alpha}\right) \right)^{-1}, \quad (3.5)$$

where R_0 is the half-density radius. By adding more units of isospin the value of the neutron surface thickness increases and the surface becomes more diffuse. The RHB model predicts a uniform increase of *rms* radii with the number of neutrons. The neutron skin $r_n - r_p$ increases to approximately 0.4 fm at the closed shell $N = 50$. The diffuseness parameter is essentially a step function: $\alpha \approx 0.45$ fm for $N < 40$ and $\alpha \approx 0.50$ fm for neutrons in the $1g_{9/2}$ orbital.

In the following we investigate how the formation of neutron skin is related to the properties of the low-lying E1 excitations in Ni isotopes. The isovector strength distributions for ^{48}Ni , ^{58}Ni , ^{68}Ni and ^{78}Ni are shown in Fig. 3.12. Already for ^{48}Ni a peak is found in the low-energy region below 10 MeV. This state is characterized by a single proton ph excitation (96% $1f_{7/2} \rightarrow 2d_{5/2}$), and it is not found in the spectra of heavier Ni isotopes.

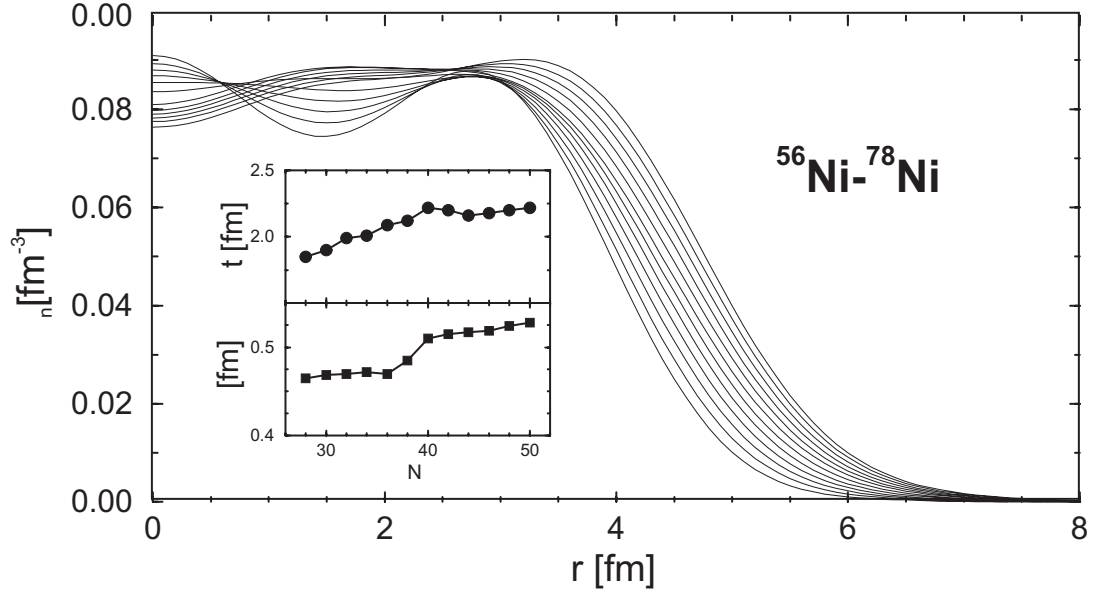


Figure 3.11: Self-consistent RHB single-neutron density distributions for Ni isotopes ($28 \leq N \leq 50$). The surface thickness t and diffuseness parameter α are displayed as a function of neutron number.

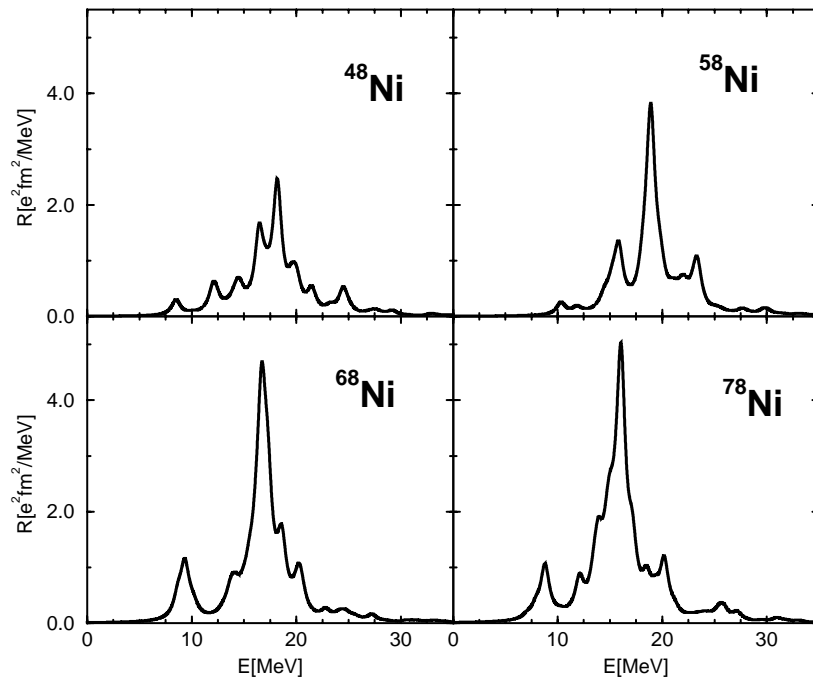


Figure 3.12: Isovector dipole strength distribution in Ni isotopes.

The low-energy dipole states built on valence neutron ph configurations appear only in ^{62}Ni and heavier isotopes. The relative contribution of the low-energy region $E \leq 10$ MeV to the dipole strength distribution increases with the neutron excess. The ratio of energy weighted moments $m_{1,low}/m_{1,high}$ increases from 0.01 in ^{62}Ni to 0.06 in ^{78}Ni . Similar to the light nuclei, the low-energy spectra are dominated by the single particle transitions. There is an important difference, however. For the heavier Ni isotopes we find one dipole state in the low-energy region, which displays a more complex structure of the RQRPA amplitude, i.e. a coherent superposition of more than just a few neutron ph configurations. In the case of ^{68}Ni , this is the state at 9 MeV (4.3% EWSR). A dipole state with a similar structure in ^{78}Ni is found at 8.9 MeV (4.0% EWSR). The state at 8.9 MeV is characterized by a strong isoscalar transition density and a long tail of the neutron transition density which extends almost to 10 fm.

3.4 Evolution of the Low-lying Isovector Dipole Strength in $N=82$ Isotones

In this section we focus more on the multipole response in exotic medium-heavy nuclei to investigate how the presence of a pronounced neutron skin affects the giant resonances and collective properties of the low-energy excitations. This region of the periodic chart is especially interesting, since heavier nuclei are presently beyond the computational reach of many other available theoretical models. The dipole response of very neutron-rich isotopes is characterized by the fragmentation of the strength distribution and its spreading into the low-energy region, and by the mixing of isoscalar and isovector modes. In the last sections, it appeared that in most relatively light nuclei the onset of dipole strength in the low-energy region is due to non-resonant independent single particle excitations of the loosely bound neutrons.

However, the structure of the low-lying dipole strength changes with mass. We have already shown that the low-lying dipole states are characterized by a more distributed structure of the RQRPA amplitude. Among several peaks characterized by single particle transitions, a single collective dipole state is identified below 10 MeV, and its amplitude represents a superposition of several neutron particle-hole configurations.

Very recently experimental data have been reported on the concentration of electric dipole strength below the neutron separation energy in $N = 82$ semi-magic nuclei. The distribution of the electric dipole strength in ^{138}Ba , ^{140}Ce , and ^{144}Sm displays a resonant structure between 5.5 MeV and 8 MeV, exhausting $\approx 1\%$ of the isovector E1 EWSR [121]. In ^{138}Ba negative parity quantum numbers have been assigned to 18 dipole excitations between 5.5 MeV and 6.5 MeV [122]. The electromagnetic dipole response in ^{138}Ba has been also studied in another photon scattering experiment, but only up to 6.7 MeV [25].

In Figs. 3.13 and 3.14 we display the isovector dipole strength distributions in eight $N = 82$ isotones, calculated in the RHB+RQRPA framework with the NL3+D1S combination of effective interactions. The calculation is again fully self-consistent, with the Gogny finite-range pairing included both in the RHB ground state, and in the RQRPA residual interaction. The isovector dipole response is shown for even- Z nuclei from ^{146}Gd to the doubly magic ^{132}Sn . In addition to the characteristic peak of the isovector giant dipole resonance (IVGDR) at ≈ 15 MeV, the evolution of the low-lying dipole strength with decreasing proton number is clearly observed below 10 MeV. The strength of the low-lying dipole response increases with the relative increase of the neutron contribution, i.e. with reducing the number of protons. For the main peaks in the low-energy region below 10 MeV, in the panels on the right side of Figs. 3.13 and 3.14 we display the corresponding neutron and proton transition densities. The radial dependence is very different from that of the transition densities of the IVGDR peak. For all eight nuclei the main peak below 10 MeV does not correspond to an isovector excitation, i.e. the proton and neutron transition densities have the same sign. The relative contribution of the protons in the surface region decreases with reducing the proton number. In particular, for the nuclei shown in Fig. 3.14: ^{138}Ba , ^{136}Xe , ^{134}Te and ^{132}Sn , there is practically no proton contribution to the transition density beyond 6 fm. The dynamics is that of a pygmy resonance: the neutron skin oscillates against the core. In Ref. [121] it was emphasized

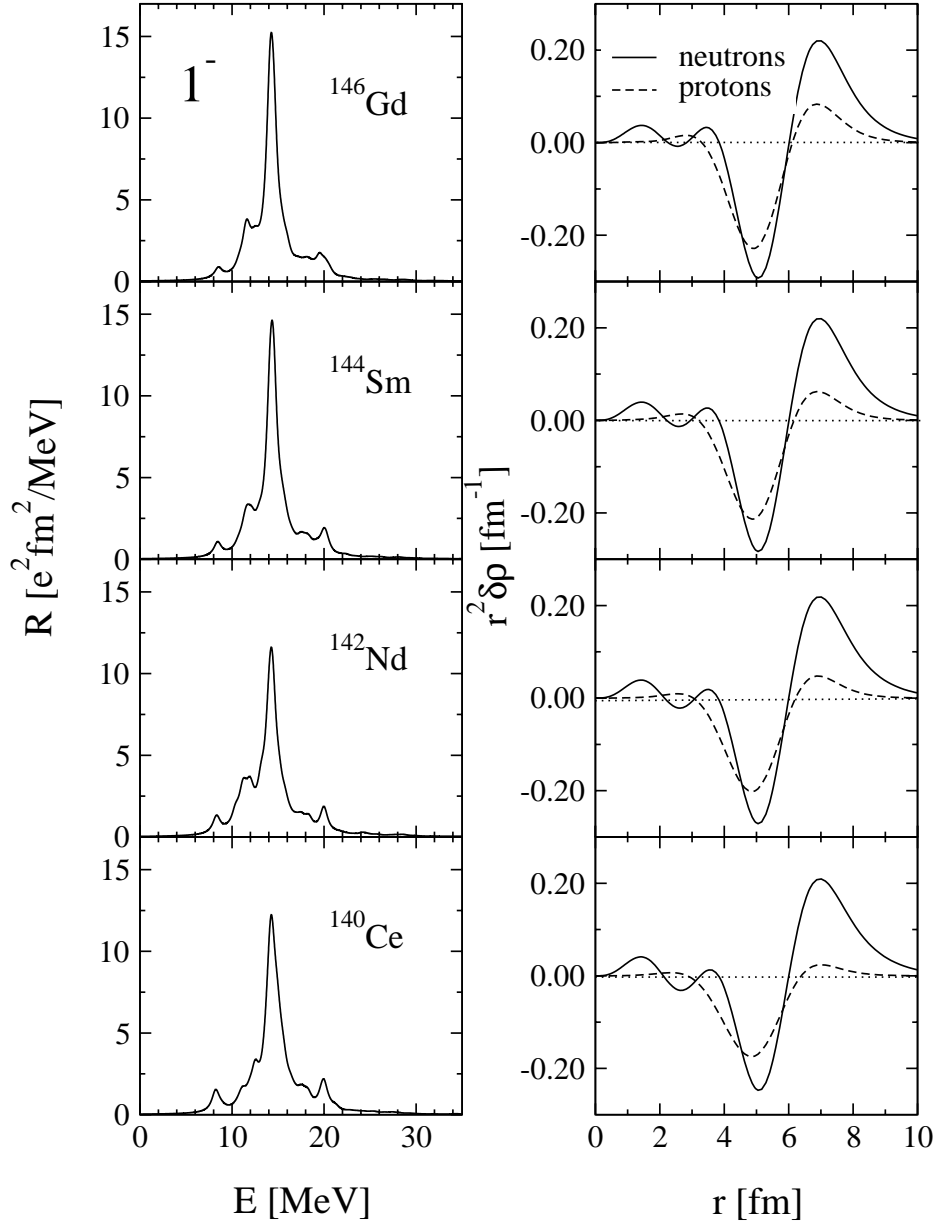


Figure 3.13: RHB+RQRPA isovector dipole strength distributions in ^{146}Gd , ^{144}Sm , ^{142}Nd and ^{140}Ce , calculated with the NL3+D1S effective interaction. The corresponding proton and neutron transition densities for the main peak in the low-energy region below 10 MeV are displayed in the panels on the right side.

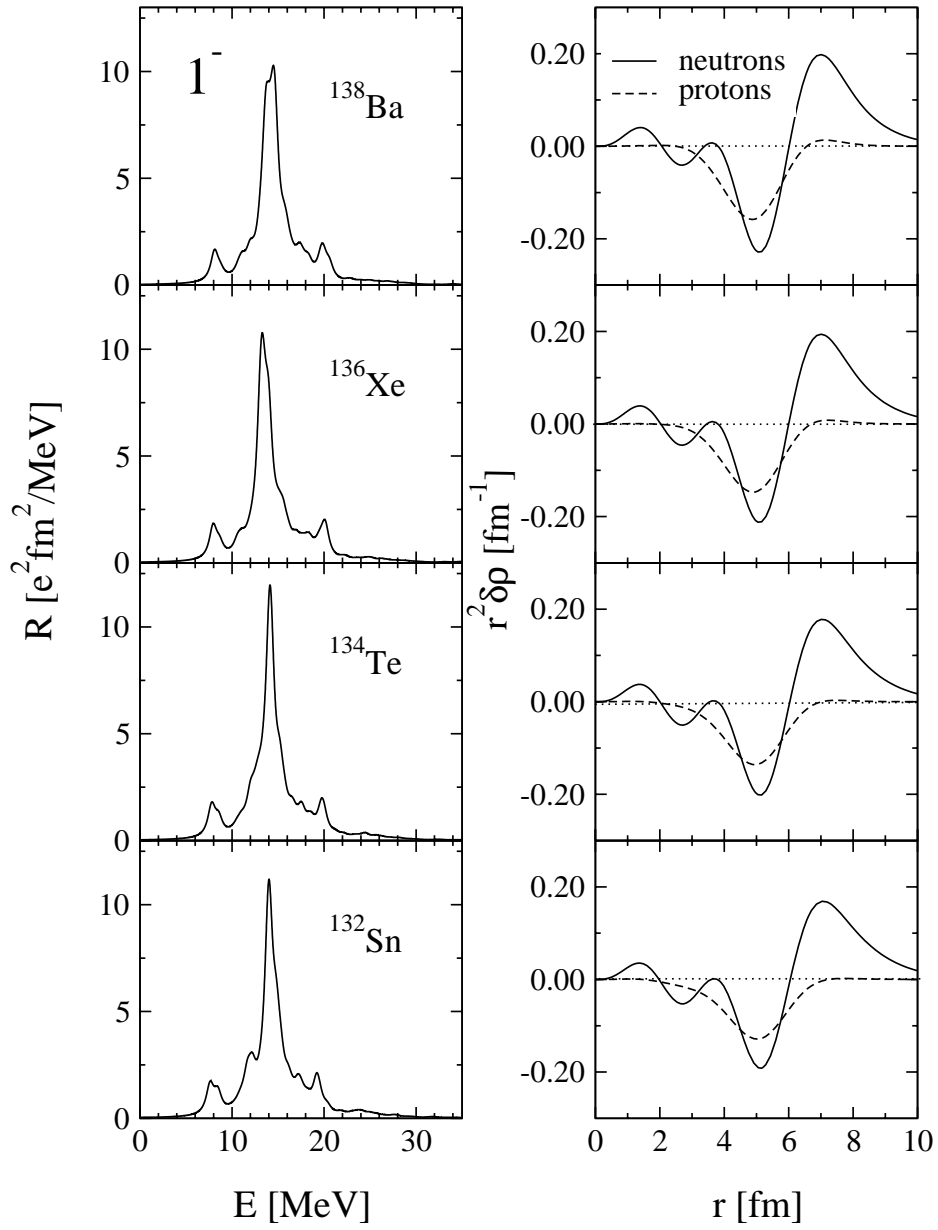


Figure 3.14: Same as in Fig. 3.13, but for the $N = 82$ isotones: ^{138}Ba , ^{136}Xe , ^{134}Te and ^{132}Sn .

that the observed low-lying dipole states in the N=82 isotones are not just statistical E1 excitations sitting on the tail of the GDR, but represent a fundamental structure effect. In

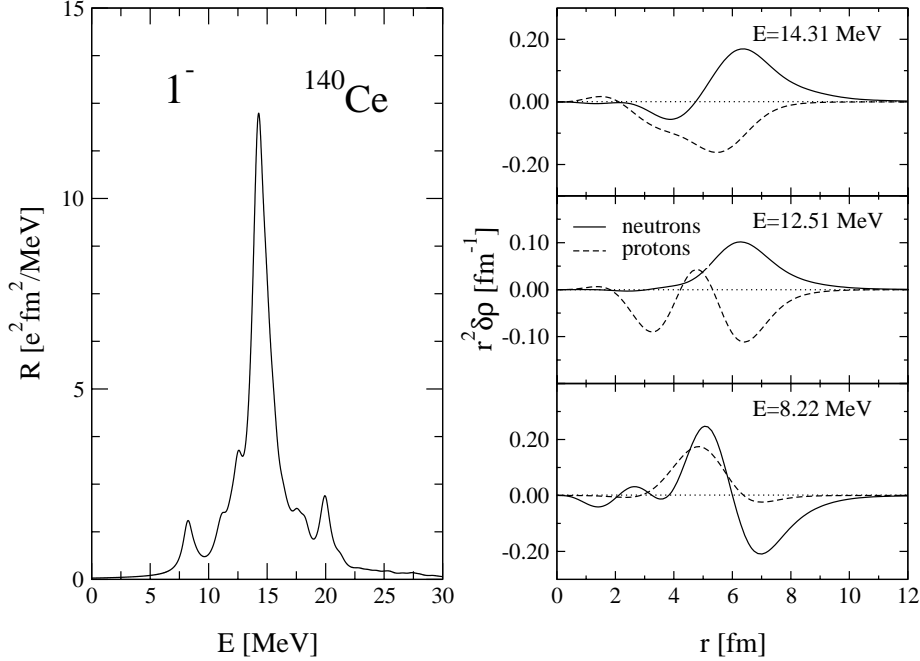


Figure 3.15: The isovector dipole strength distribution in ^{140}Ce (left panel). The neutron and proton transition densities for the IVGDR peaks at 14.31 MeV, 12.51 MeV, and for the main peak in the low-energy region at 8.22 MeV (right).

Fig. 3.15 we show that this is also the case for the RHB+RQRPA results. For the dipole strength distribution of ^{140}Ce , shown in the left panel, in the right column we compare the neutron and proton transition densities for the IVGDR peak at 14.31 MeV, for the peak at 12.51 MeV, and for the main peak in the low-energy region at 8.22 MeV. The peak at 12.51 MeV, as well as other peaks in the interval 10-14 MeV, displays transition densities very similar to those of the GDR peak, i.e. these states belong to the tail of the GDR. The dynamics of the low-energy mode at 8.22 MeV, on the other hand, is very different: the proton and neutron transition densities are in phase in the nuclear interior, there is almost no contribution from the protons in the surface region, the isoscalar transition density dominates over the isovector one, and the peak of the strong neutron transition density in the surface region is shifted toward larger radii.

In Table 3.5 we list the centroid energies of the low-lying E1 strength and the summed $B(E1)$ strength in the region below 10 MeV in N=82 isotones. On a quantitative level, the present RHB+RQRPA calculation does not compare too well with the experimental data. First, while the observed low-energy dipole states in ^{138}Ba , ^{140}Ce , and ^{144}Sm are concentrated between 5.5 MeV and 8 MeV, the calculated pygmy states in these nuclei

N=82 ISOTONE	m_1/m_0 [MeV]	m_0 [$e^2 fm^2$]
^{134}Te	8.05	3.37
^{136}Xe	8.12	2.97
^{138}Ba	8.20	2.64
^{140}Ce	8.28	2.24
^{142}Nd	8.36	1.75
^{144}Sm	8.45	1.33
^{146}Gd	8.55	1.03

Table 3.5: Low-lying centroid energies (m_1/m_0) and B(E1) strength (m_0) summed within the energy interval $0 < E < 10$ MeV in a selection of N=82 isotones.

are above 8 MeV. This can be partly explained by the low effective nucleon mass of the NL3 mean-field interaction [123]. On the other hand, the excitation energies of the IV GDR are, as will be shown below in the example of Sn isotopes, rather well reproduced by the NL3 interaction. The fact that NL3 reproduces the IV GDR, but not the centroid of the low-energy dipole strength, might indicate that the isovector channel of this force needs a better parameterization. Second, the number of RQRPA peaks below 10 MeV, for the operator (2.35), is much smaller than the number of observed dipole states in the low-energy region [122, 121]. Again, this is partly due to the low effective mass of the relativistic mean-field interaction. A higher effective mass would, generally, produce more fragmentation. The observed low-lying E1 strength could, however, be of different origin. This has been discussed in Ref. [121]. In addition to the two-phonon $2^+ \otimes 3^-$ state, and the soft pygmy state, in this energy region one could also expect some compressional low-lying isoscalar dipole strength [124], maybe mixed with toroidal states [125], as well as the E1 strength generated by the breaking of the isospin symmetry due to a clustering mechanism [126]. A detailed investigation of the nature of all observed low-lying dipole states in N=82 nuclei is, of course, beyond the reach of the present analysis. For one thing, it would require an interaction with higher effective mass, that would bring the calculated low-lying dipole strength below 8 MeV. Such a mean-field relativistic effective interaction is presently not available.

3.5 Soft Collective Oscillations in Tin Isotopes

In the following, we investigate the structure of the low-lying dipole strength within the tin isotope chain. The RHB neutron-density distributions for Sn isotopes ($50 \leq N \leq 82$) are displayed in Fig. 3.16. In addition, we plot the diffuseness parameter α and surface thickness t , defined in Eq. (3.5). As the number of neutrons increases, the neutron surface thickness becomes larger, and the surface is more diffuse. Similar to the case of Ni isotopes, the RHB model here also predicts a uniform increase of *rms* radii with the number of neutrons. Both diffuseness parameters and surface thickness increase by approximately 40% from ^{100}Sn to ^{132}Sn . The unique excitation phenomena in neutron

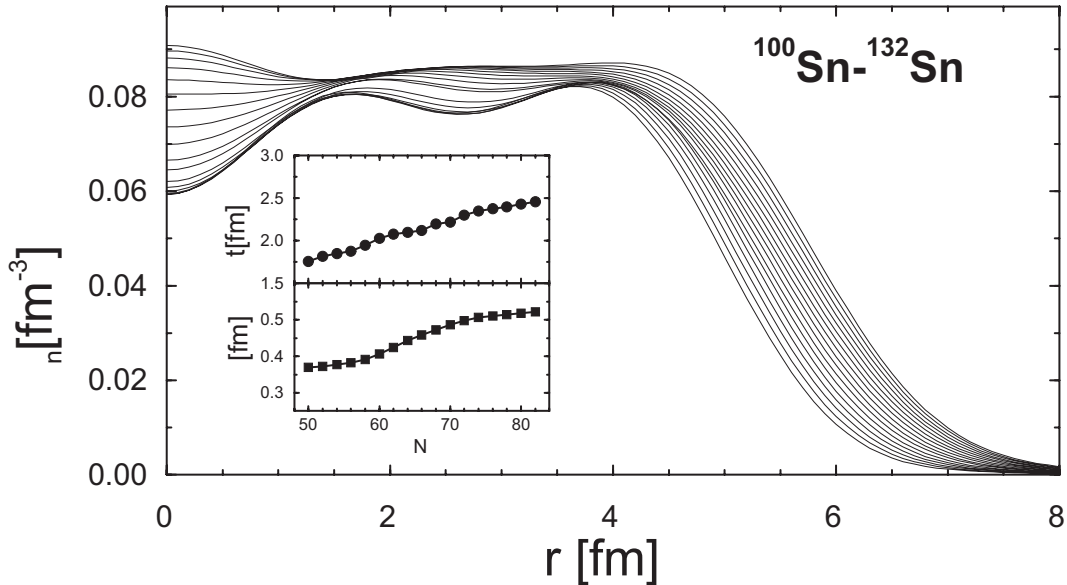


Figure 3.16: Self-consistent RHB single-neutron density distributions, diffuseness parameter α and surface thickness t for Sn ($50 \leq N \leq 82$) isotopes.

rich isotopes are closely related to the properties of the neutron skin.

The results of the fully self-consistent RHB+RQRPA calculation, with the NL3+D1S combination of effective interactions, are shown in Figs. 3.17 and 3.18: the isovector dipole strength functions of the Sn isotopes (left panels), and the corresponding proton and neutron transition densities for the main peaks in the low-energy region (right panels).

With the increase of the number of neutrons, the onset of low-lying strength below 10 MeV is observed. The low-energy strength is most pronounced in ^{124}Sn . It does not become stronger by further increasing the neutron number, and additional fragmentation of the low-lying strength is observed in ^{132}Sn . The dipole states in this energy region exhibit a structure different to that observed in the neutron rich oxygen isotopes: among several peaks characterized by single particle transitions, between 7 MeV and 9 MeV a state is found with a more distributed structure of the RRPA amplitude, exhausting approximately 2% of the EWSR. In ^{132}Sn , for example, this state is calculated at 8.6 MeV and it exhausts 1.4% of the EWSR.

The distribution of neutron ph configurations for this soft mode is displayed in Table 3.5. Nine neutron ph configurations contribute with more than 0.1% to the total RRPA intensity, but there are also many other configurations with smaller contributions to the overall strength distribution function. The total contribution of proton ph excitations is only 10.4%, well below the ratio Z/N expected for a GDR state. We notice also that in the Hartree-Fock + RPA analysis of the E1 resonances in ^{208}Pb [34], it was found that for the pygmy states the neutron response is a factor 10 larger than the proton response, whereas at energies corresponding to the GDR this ratio is around 1.6, or roughly equal to N/Z . The low-energy pygmy peak is most pronounced in ^{124}Sn . It does not become stronger by further increasing the neutron number, and additional fragmen-

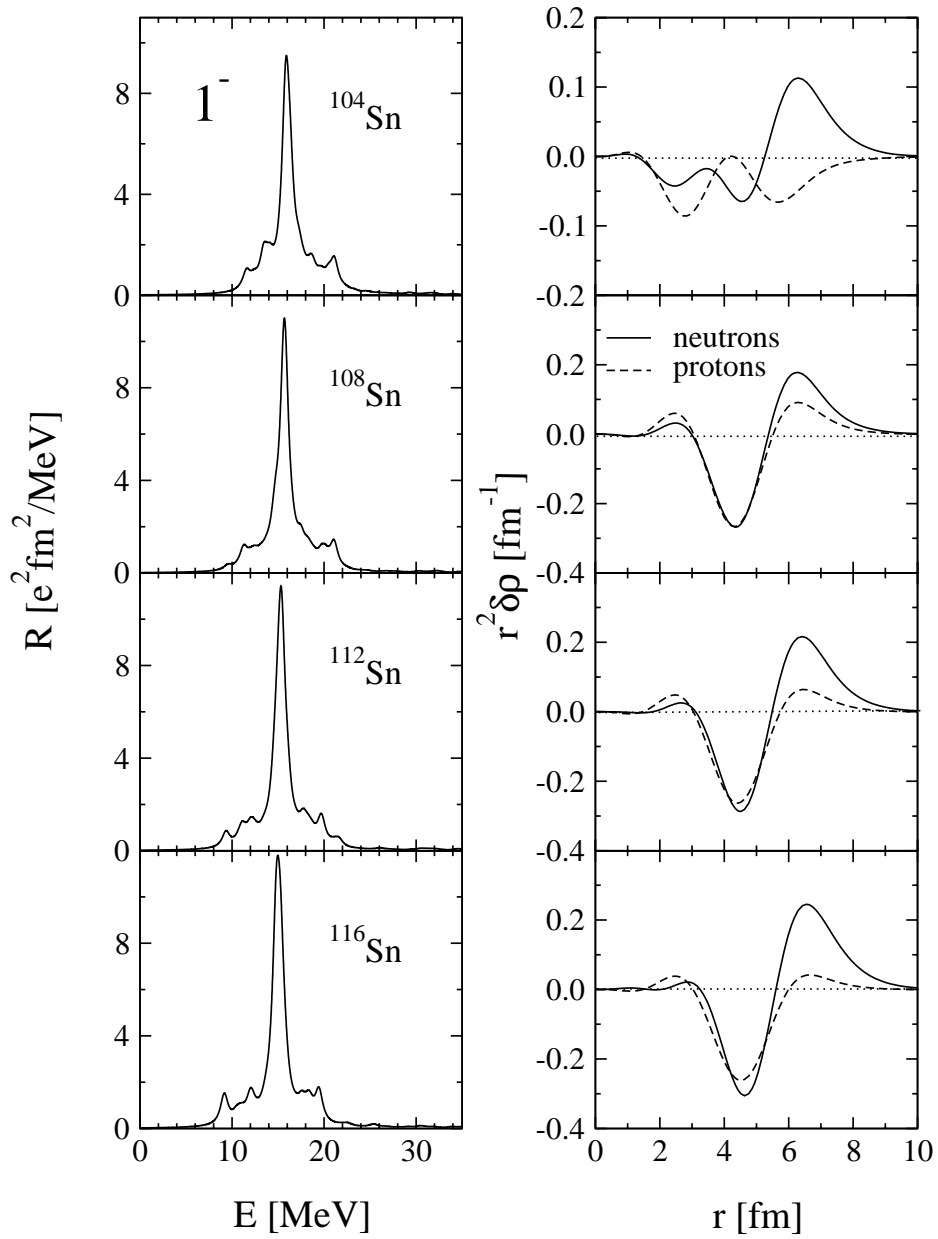


Figure 3.17: RHB+RQRPA isovector dipole strength distributions in Sn isotopes, calculated with the NL3+D1S effective interaction. The corresponding proton and neutron transition densities for the main peak below the IVGDR are displayed in the panels on the right side.

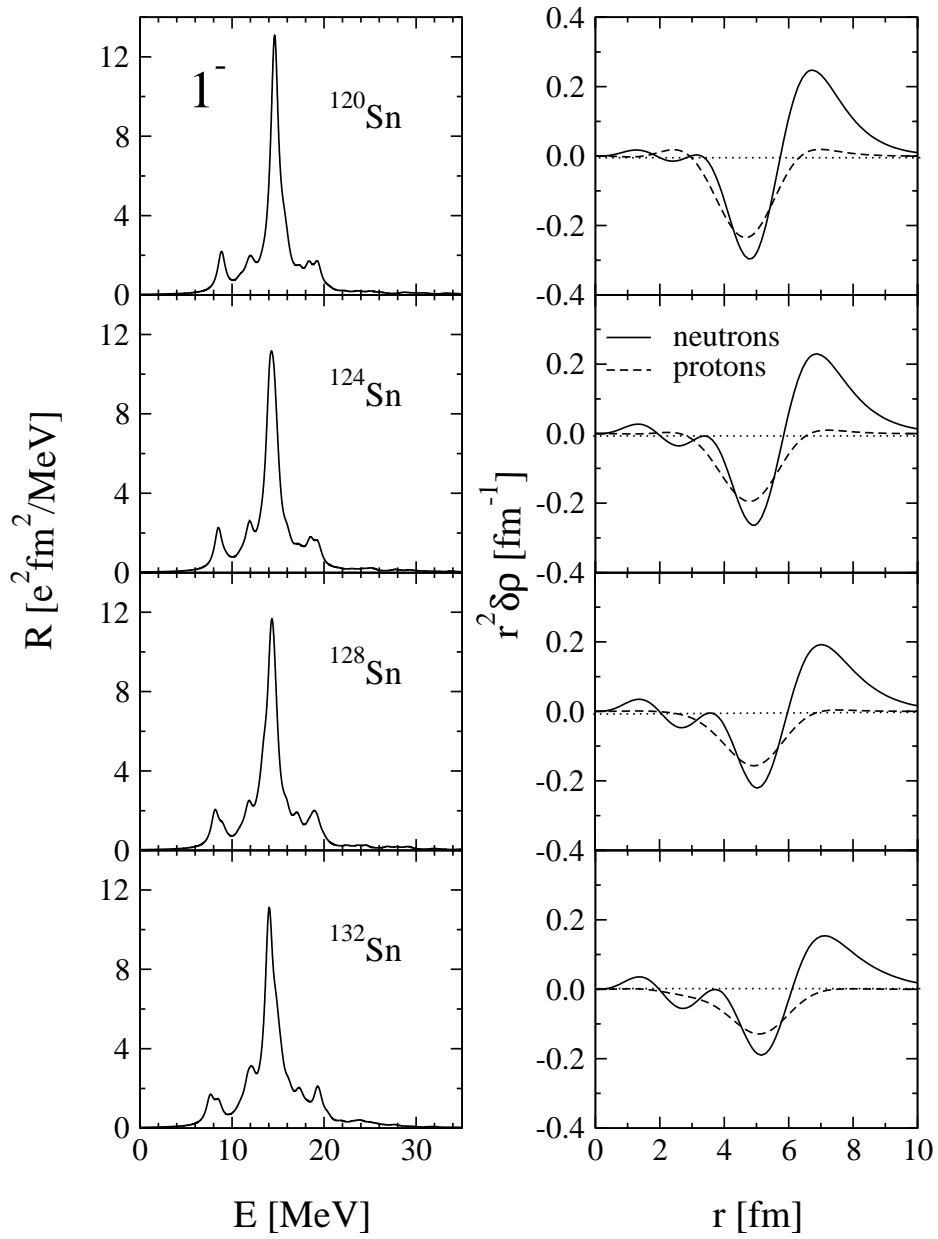


Figure 3.18: Same as in Fig. 3.17, but for the heavier Sn isotopes.

28.2%	$2d_{3/2} \rightarrow 2f_{5/2}$
21.9%	$2d_{5/2} \rightarrow 2f_{7/2}$
19.7%	$2d_{3/2} \rightarrow 3p_{1/2}$
10.5%	$1h_{11/2} \rightarrow 1i_{13/2}$
3.5%	$2d_{5/2} \rightarrow 3p_{3/2}$
1.9%	$1g_{7/2} \rightarrow 2f_{5/2}$
1.5%	$1g_{7/2} \rightarrow 1h_{9/2}$
0.6%	$1g_{7/2} \rightarrow 2f_{7/2}$
0.6%	$2d_{3/2} \rightarrow 3p_{3/2}$

Table 3.6: Distribution of neutron particle-hole configurations for the state at 8.6 MeV (1.4% EWSR) in ^{132}Sn . The percentage of a $p-h$ configuration refers to the normalization of the RRPA amplitudes (3.2). Only configurations which contribute more than 0.1% are displayed.

tation of the low-lying strength is observed in ^{132}Sn . In Fig. 3.19 we plot the RQRPA transition densities to the two states at 8.6 MeV and 14.8 MeV in ^{132}Sn . In the upper panel the proton, neutron, isoscalar and isovector components are displayed. The radial dependence of transition densities clearly demonstrate the differences between the pygmy dipole and GDR states, which are similar to our previous results for lighter nuclei. In the lower panel, for the pygmy state at 8.6 MeV (c) and for the GDR state at 14.8 MeV (d), the contributions of the excess neutrons ($50 < N \leq 82$) (solid), and of the proton-neutron core ($Z, N \leq 50$) (dashed) are displayed separately. By comparing with the transition densities shown in the upper panel of Fig. 3.19, we notice that there is practically no contribution from the core neutrons ($N \leq 50$). The ph excitations of core neutrons are, of course, at much higher energies. For the GDR state, therefore, the transition densities of the core nucleons and of the excess neutrons have opposite phases (isovector mode). The absolute radial dependence is similar, with the amplitude strongly peaked in the surface region. The two transition densities have the same sign for the pygmy state at 8.6 MeV. The core contribution, however, vanishes for large r and only oscillations of the excess neutrons are observed on the surface of ^{132}Sn .

For the Sn isotopes we can compare the RHB+RQRPA results with available experimental data on IV GDR. In the upper panel of Fig. 3.20 the experimental IVGDR excitation energies [127] are shown in comparison with the calculated E_{GDR} . All excitation modes are calculated with NL1, NL-SH, and NL3 relativistic mean-field interactions. The energy of the resonance is defined as the centroid energy 2.57. The calculated energies of the IV GDR for NL3+D1S effective interaction, are in excellent agreement with experimental data, and the mass dependence of the excitation energies is reproduced in detail. In the middle panel of Fig. 3.20 we plot the calculated energies of the pygmy states. In comparison with the IV GDR, the excitation energies of the pygmy states decrease more steeply with the mass number. The mass dependence of the energy of pygmy mode (PDR) has been derived in the two-fluid hydrodynamical model as a function of

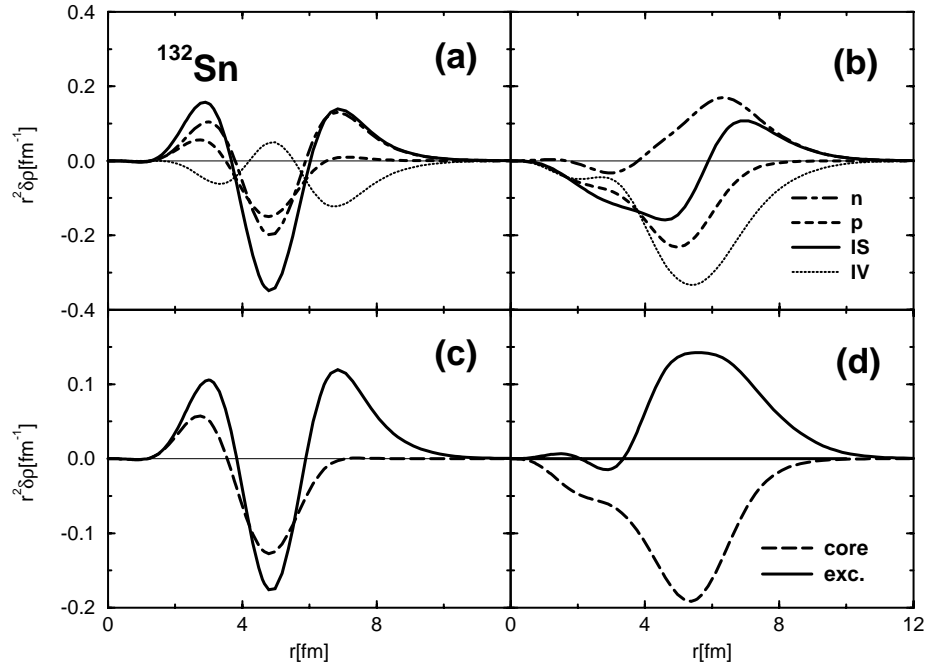


Figure 3.19: Isovector (IV) and isoscalar (IS) dipole transition densities for the states at 8.6 MeV (a) and 14.8 MeV in ^{132}Sn . The separate proton and neutron contributions to the transition densities are also shown. In the lower part of the figure the contributions of the excess neutrons ($50 < N \leq 82$) (solid), and of the proton-neutron core ($Z, N \leq 50$) (dashed) are displayed separately for the state at 8.6 MeV (c), and 14.8 MeV (d). The transition densities are multiplied by r^2 .

the GDR energy [31], in particular for the neutron rich nuclei,

$$E_{PDR} = \sqrt{\frac{Z(N - N_c)}{N(Z + N_c)}} E_{GDR}. \quad (3.6)$$

The number of neutrons in the core, N_c is determined from the condition to get the maximal binding energy per particle, for fixed number of protons [31]. However, this formula predicts increase of the pygmy excitation energy with neutron excess in contrast to the RQRPA centroid energies which decrease with the number of neutrons. The RQRPA mass dependence of the pygmy mode is qualitatively in agreement with the density functional calculations for calcium isotopes in Ref. [32]. This effect can also be illustrated within the simple harmonic oscillator model, where the resonance frequency is determined by the restoring force per particle. The restoring force is related to the neutron separation energy, as a measure of how tightly the neutron excess is bound. Therefore, in this simple model, the frequency of the pygmy mode should decrease as one moves toward the neutron drip-line. The dipole strength of the pygmy mode from the hydrodynamical

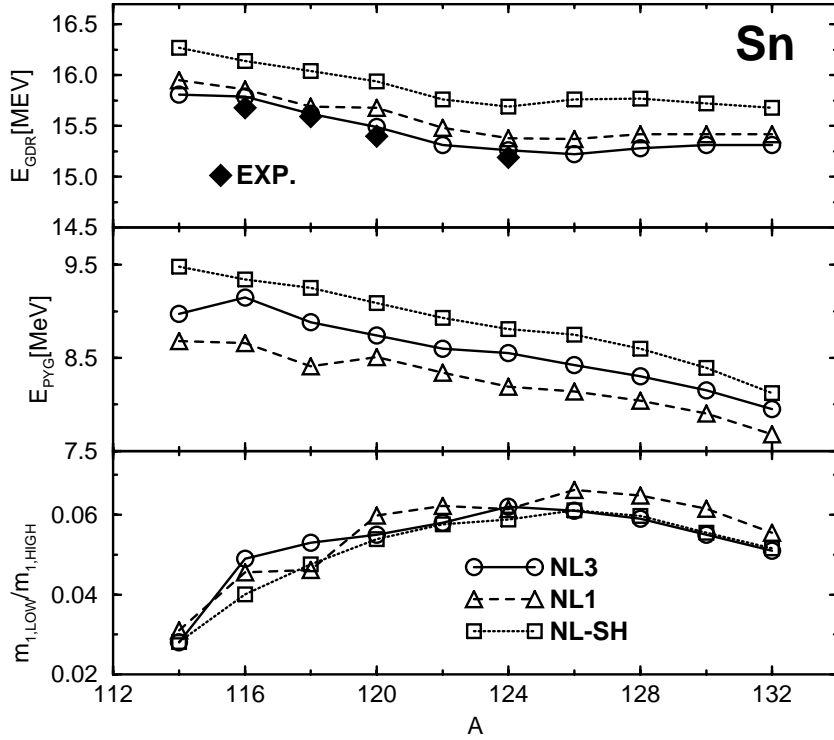


Figure 3.20: In the upper panel the experimental IV GDR excitation energies of the Sn isotopes are compared with the RHB+RQRPA results calculated with the NL1, NL-SH and NL3 relativistic effective interaction, and D1S parameterization is implemented in the pairing channel. The calculated energies of the pygmy states are shown in the middle panel. The values of the ratio $m_{1,\text{LOW}}/m_{1,\text{HIGH}}$, of the energy weighted moments m_1 in the low-energy region ($E \leq 10$ MeV) and in the region of giant resonances ($E > 10$ MeV), are plotted in the lower panel.

model in Ref. [31] reads,

$$S_{PDR} = 0.857 \frac{Z(N - N_c)}{N(Z + N_c)} S_{TRK} \quad (3.7)$$

where S_{TRK} is the classical TRK dipole sum-rule. Accordingly, the low-lying dipole strength increases as the neutron number becomes larger. This is in agreement with the RHB+RQRPA model.

The ratio of the energy weighted m_1 moments calculated in the low ($E \leq 10$ MeV) and high ($E > 10$ MeV) energy regions, as a function of the mass number, is plotted in the lower panel of Fig. 3.20 for NL3, NL1, and NL-SH effective interaction. The relative contribution of the low-energy region increases with the neutron excess. The ratio $m_{1,LOW}/m_{1,HIGH}$ reaches a maximum ≈ 0.06 for ^{124}Sn , and it slowly decreases to ≈ 0.05 for ^{132}Sn . This behavior may be a consequence of the shell effects. Namely, as the neutron number approaches a magic number $N = 82$, where the collectivity of giant resonance is strongly pronounced, the pygmy mode becomes depleted. Electric dipole transitions up to the particle threshold at about 9 MeV have been recently investigated in ^{116}Sn and ^{124}Sn using the high resolution nuclear resonance fluorescence technique [24]. The measured strength distributions for both isotopes show the existence of a pronounced concentration of low-lying states (around 6.5 MeV), related to the pygmy dipole resonance. These results have been also successfully described within the quasiparticle phonon model calculations taking into account the coupling up to three phonons [24].

3.6 Pygmy Dipole Resonances in Stable Nuclei

In the preceding sections, we have mainly focused our attention on the possible occurrence of skin resonances in the nuclei away from the valley of β stability. However, exotic collective modes of excitation in principle could be excited in stable heavy nuclei also, where the neutron to proton asymmetry is sufficiently large. It is of a particular interest to see if the neutron excess may rise, in addition to the usual giant resonance, also in some decoupled low energy excitation phenomena. We take ^{208}Pb as a typical example of a heavy neutron rich nucleus from the valley of stability, with neutron emission threshold at 7.4 MeV. There is also experimental evidence for possible pygmy dipole states in ^{208}Pb . Studies of the low energy spectrum by elastic photon scattering [128], photoneutron [129], and electron scattering [130] have detected fragmented E1 strength in the energy region between 8 and 11 MeV. The fine structure exhausts between 3 and 6% of the E1 sum rule. A very recent nuclear resonance fluorescence experiment reported the existence of a resonance E1 structure, centered around the neutron emission threshold, which was identified by the quasiparticle phonon model calculations as the surface density oscillations of the neutron skin relative to an isospin saturated core [26]. The relationship between coherent neutron particle-hole (p-h) excitations and the onset of dipole pygmy resonances in ^{208}Pb has been investigated in the Hartree-Fock plus RPA model [34]. A concentration of strength has been found around 9 MeV exhausting 2.4% of the E1 sum rule. In particular, two pronounced peaks have been calculated at 8.7 MeV and 9.5 MeV, which appear as likely candidates to be identified as pygmy resonances. The exact location of the calculated pygmy states will, of course, depend on the effective nuclear interaction. Therefore, it would be important to compare the predictions of various nuclear effective forces with experimental data. ^{208}Pb is a particularly good example, since all nuclear structure models have been tested in the description of ground and excited state properties of this doubly magic spherical nucleus. The pygmy dipole resonance can be directly related to the neutron excess, and therefore the splitting between the GDR and the pygmy resonance represents a measure of the neutron skin. Precise information on the neutron skin in heavy nuclei is essential for the quantification of the isovector channel of effective nuclear forces.

In the present study the isovector dipole response in ^{208}Pb is described in the framework of a fully self-consistent relativistic random phase approximation (RRPA), which is a limit of RHB+RQRPA model for the closed shell configuration. The same effective Lagrangian generates the Dirac-Hartree single-particle spectrum and the residual particle-hole interaction. In Fig. 3.21 we display the isovector dipole strength distribution in ^{208}Pb (left panel), and the corresponding transition densities to the two states at 7.29 MeV and 12.95 MeV (right panel). The calculations have been performed within the framework of self-consistent Dirac-Hartree plus relativistic RPA. The effective mean-field Lagrangian contains nonlinear meson self-interaction terms, and the configuration space includes both particle-hole pairs and pairs formed from hole states and negative-energy states. The discrete spectrum of RRPA states has been folded with a Lorentzian distribution with a width of 1.0 MeV. The strength distribution has been calculated with the NL3 [80] parameter set for the effective mean-field Lagrangian. The calculated energy of the main

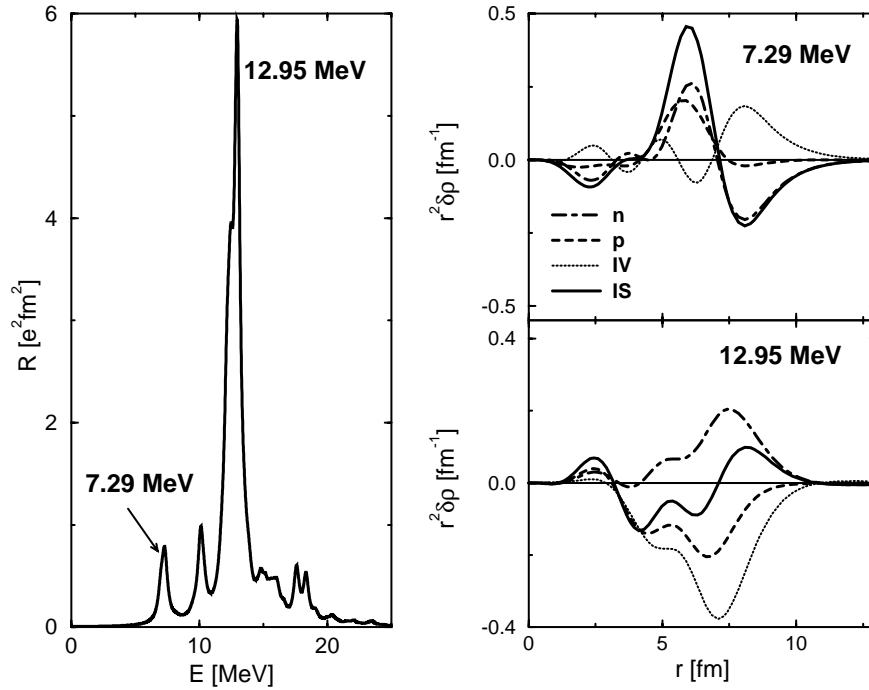


Figure 3.21: Isovector dipole strength distribution in ^{208}Pb (left panel), and transition densities for the two peaks at 7.29 MeV and 12.95 MeV (right panel). Both isoscalar and isovector transition densities are displayed, as well as the separate proton and neutron contributions. All transition densities are multiplied by r^2 .

peak in Fig. 3.21 $E_p = 12.95$ MeV has to be compared with the experimental value of the excitation energy of the isovector giant dipole resonance: 13.3 ± 0.1 MeV [131]. In the energy region between 5 and 11 MeV two prominent peaks are calculated: at 7.29 MeV and 10.10 MeV. In the following we will show that the lower peak can be identified as the pygmy dipole resonance.

The transition densities to the states at 7.29 MeV and at 12.95 MeV are displayed in the right panel of Fig. 3.21. The proton and neutron contributions are shown separately; the dotted line denotes the isovector transition density and the solid line has been used for the isoscalar transition density. As it has been also shown in Ref. [33], although the isoscalar $B(E1)$ to all states must vanish identically, the corresponding isoscalar transition densities to different states need not to be identically zero. The transition densities for the main peak at 12.95 MeV display a radial dependence characteristic for the isovector giant dipole resonance: the proton and neutron densities oscillate with opposite phases; the total isovector transition density is much larger than the isoscalar component; at large radii they both have a similar radial dependence. A very different behavior is observed for the transition densities to the state at 7.29 MeV: the proton and neutron densities in the interior region are not out of phase; there is almost no contribution from the protons in the surface region; the isoscalar transition density dominates over the isovector one in the interior; the large neutron component in the surface region contributes to the formation

of a node in the isoscalar transition density. In Ref. [33] it has been shown that this last effect is also characteristic for very neutron-rich systems. The transition densities to the state at 10.10 MeV display a radial behavior which is intermediate between those shown in Fig. 3.21, but closer to the isovector giant dipole at 12.95 MeV. We have also analyzed the RRPA amplitudes of the three states: the neutron p-h excitations contribute 65%, and the proton 35% to the total intensity of the isovector giant dipole at 12.95 MeV, while the neutron contribution is 86% for the state at 7.29 MeV. The proton p-h excitations contribute only 14% to the total RPA intensity of this state. For the state at 10.10 MeV, on the other hand, we find 68% of proton excitations and only 32% is the contribution from neutron p-h configurations. However, 31% of the total intensity comes from a single proton p-h state: $g7/2^{-1} h9/2$. We notice that in the study of neutron halos and E1 resonances in ^{208}Pb [34], performed in the HF+RPA model with the SGII interaction, it was found that for the pygmy states the neutron response is a factor 10 larger than the proton response, whereas at energies corresponding to the GDR this ratio is about 1.6 or roughly N/Z .

The phenomenon of low-lying isovector dipole strength was already studied almost thirty years ago in the framework of the three-fluid hydrodynamical model [30]. By using a generalization of the Steinwedel-Jensen model [132] to three fluids: the protons, the neutrons in the same orbitals as protons, and the excess neutrons, two normal modes of dipole vibrations were identified: (i) vibrations of the protons against the two types of neutrons, and (ii) the vibration of the excess neutrons against the proton-neutron core. In the case of neutron-rich nuclei, the later mode corresponds to pygmy resonances. For ^{208}Pb , in addition to the GDR state at 13.3 MeV, a low-lying pygmy state at 4.4 MeV excitation energy was found in the analysis of Ref. [30]. The dipole strength of this state, however, was negligible (2 orders of magnitude) compared to the GDR state.

In Fig. 3.22 we plot the transition densities to the two states at 7.29 MeV and 10.10 MeV. The contributions of the excess neutrons ($82 < N \leq 126$) (solid), and of the proton-neutron core ($Z, N \leq 82$) (dashed) are displayed separately. By comparing with the transition densities shown in Fig. 3.21, we notice that there is practically no contribution from the core neutrons ($N \leq 82$). The reason is, of course, that the p-h configurations which involve core neutrons have much higher excitation energies. For the GDR state at 12.95 MeV the transition densities of the excess neutrons and the core have the same sign in the interior ($r < 3fm$), and opposite phases in the surface region. The overall radial dependence is, however, very similar. The two transition densities have the same sign for the state at 7.29 MeV. The core contribution, however, vanishes for large r and only oscillations of the excess neutrons are observed on the surface of ^{208}Pb .

The difference in the collective dynamics of the two modes is also exemplified in the study of transition currents. In Figs. 3.23 and 3.24 we plot the velocity fields for the peaks at 7.29 MeV and 12.95 MeV, respectively. The velocity distributions are derived from the corresponding transition currents, following the procedure described in Ref. [155]. In both figures the velocity field of the proton-neutron core ($Z, N \leq 82$) (left panel), is separated from the contribution of the excess neutrons ($82 < N \leq 126$) (right panel). To the largest velocity in Figs. 3.23 and 3.24 a vector of unit length is assigned. All the other velocity vectors are normalized accordingly. We notice that both the core and the

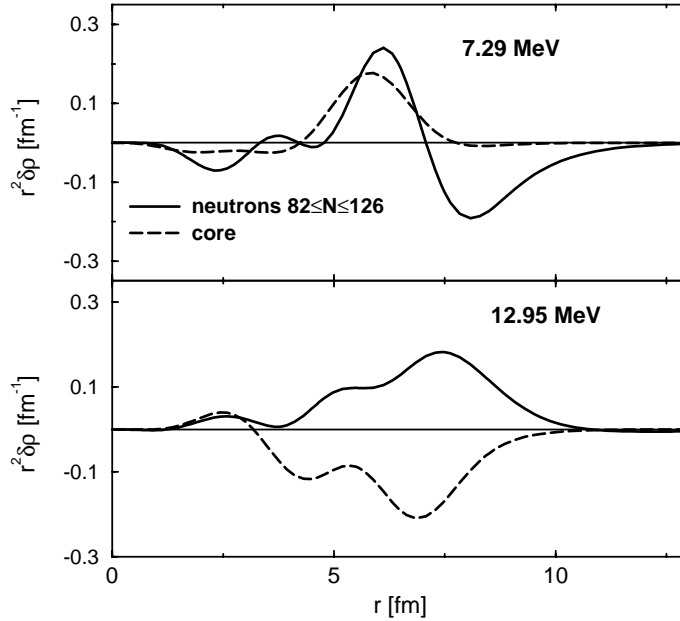


Figure 3.22: Isovector dipole transition densities to the 7.29 MeV and 12.95 MeV RRPAs in ^{208}Pb . The contributions of the excess neutrons ($82 < N \leq 126$) (solid), and of the proton-neutron core ($Z, N \leq 82$) (dashed) are displayed separately. The transition densities are multiplied by r^2 .

excess neutrons contribute to the velocity field of the giant resonance state (Fig. 3.24), though the largest velocities correspond to the vibrations of the excess neutrons in the surface region. For the state at 7.29 MeV, on the other hand, the core velocities are much smaller than those of the excess neutrons on the surface. The velocity fields in Fig. 3.23 corroborate the picture of dipole pygmy resonances as oscillations of the excess neutrons against the inert core of protons and neutrons in the same shell model orbitals. Therefore, the present RRPAs clearly demonstrate existence of a low-lying E1 collective mode at 7.29 MeV in ^{208}Pb , which has a characteristic structure of a pygmy resonance.

At the time of our RRPAs investigation in ^{208}Pb [60] the only experimental data on the fragmentation of E1 strength in ^{208}Pb was available in the limited energy window 8 – 11 MeV [128, 129, 130] and in the region below 6.5 MeV [133]. The comparison of the experimental results from Ref. [133] with the available models, suggested that the low-lying dipole strength below 6.5 MeV cannot be attributed to the pygmy mode describing oscillation of a neutron skin against the remaining core. However, in a recent nuclear resonance fluorescence experiment in Ref. [26], the E1 strength distribution is studied in more details, in particular in the region up to 8 MeV. It resulted with a series of transitions below 6 MeV, and a resonance-like structure centered approximately at the neutron emission threshold at 7.37 MeV. The RRPAs results, obtained by a self-consistent Dirac-Hartree + RRPAs calculation, are in a very good agreement with this data. The related quasiparticle phonon model (QPM) study are also close to the experimental prediction. However, to obtain this result with QPM, the energies of single-particle states

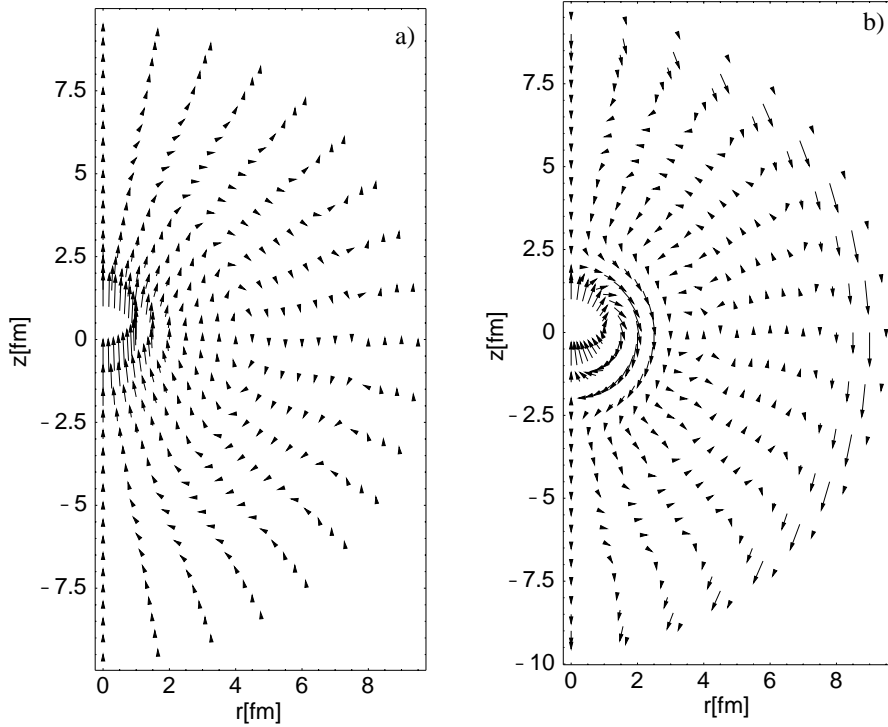


Figure 3.23: Velocity distributions for the RRP A state at 7.29 MeV in ^{208}Pb . The velocity field of the proton-neutron core ($Z, N \leq 82$) (left panel), is separated from the contribution of the excess neutrons ($82 < N \leq 126$) (right panel).

near the Fermi level have been varied, to obtain a reasonable fit of the energies of the strongest low-lying excitations below 8 MeV [26]. In the QPM model, the configuration space is more complicated than the one in RRP A, i.e. it includes two and three phonon states up to excitation energies of 13 and 16 MeV, respectively. It suggested that the mixing of 2p2h configurations, which are beyond our present model, may also have a relevant role for E1 transitions above 6.5 MeV.

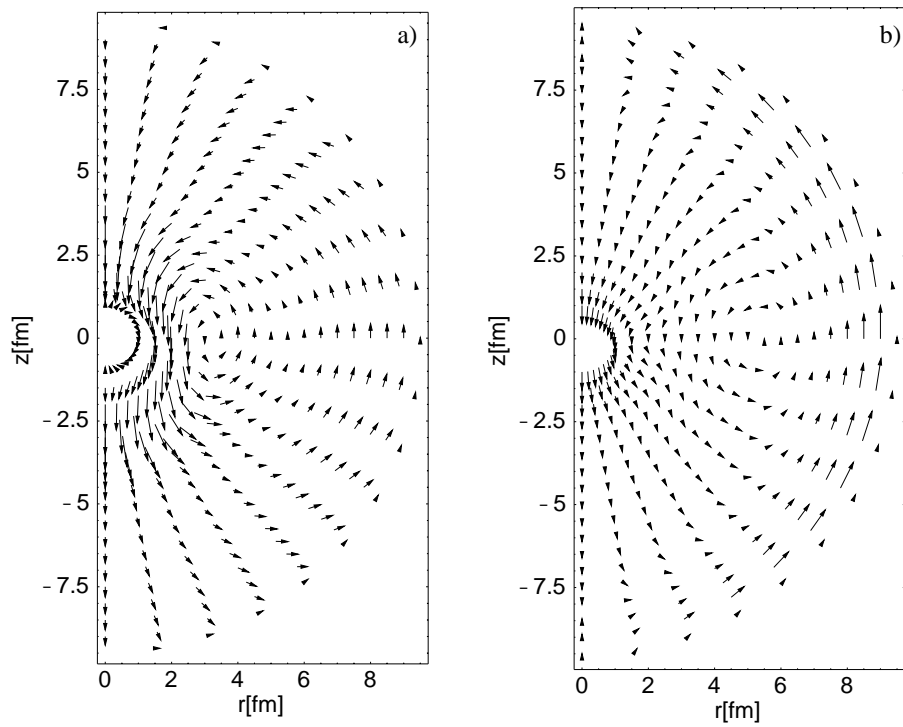


Figure 3.24: Same as in Fig. 3.23, but for the RRPA state at 12.95 MeV in ^{208}Pb .

Chapter 4

Compression Modes in Finite Nuclei

4.1 Isoscalar Giant Monopole Resonance

The nuclear matter incompressibility K_{nm} is one of the important quantities in nuclear physics. It is directly involved in the description of properties of nuclei, supernovae explosions, heavy-ion collisions and of the evolution of neutron stars at early stages. The breathing mode of atomic nuclei, i.e. the isoscalar giant monopole resonance (ISGMR) has been extensively studied in the last decades, since the compression properties of nuclei and nuclear matter incompressibility K_{nm} can be extracted from ISGMR. From the nuclear incompressibility of a finite nucleus, K_A , that is directly related to the ISGMR energy,

$$E(ISGMR) = \sqrt{\frac{\hbar^2 AK_A}{m \langle r^2 \rangle}}, \quad (4.1)$$

the nuclear matter incompressibility can be evaluated by using the extrapolation of K_A for infinitely large number of nucleons through an expansion formula in powers of $A^{-1/3}$ derived from the liquid drop model. However, because of the correlations among the parameters entering in that formula, and since there are large uncertainties in some of these parameters, another procedure to extract K_{nm} has been preferred. Basically, the excitation energy of ISGMR has to be evaluated from the self-consistent calculation for different parameterizations of the effective force. The correct value of nuclear matter incompressibility is selected from the effective force which reproduces the experimental values of the ISGMR excitation energies [134]. The ISGMR energies are usually obtained from the self-consistent RPA. Both the nonrelativistic models based on the Skyrme or Gogny interactions, and relativistic approaches with advanced effective Lagrangians reasonably reproduced the ISGMR modes [135, 134, 136, 52]. However, it appeared that the nuclear matter incompressibility is model dependent; $K_{nm}=231\pm 5$ MeV for the Gogny interaction, and $K_{nm}=205-212$ MeV for Skyrme forces. The values of K_{nm} evaluated from different relativistic effective interactions, listed in Table 1.1, are within a higher interval from 240 to 270 MeV.

Here we use the RHB+RQRPA model to evaluate ISGMR excitation energies. In the open shell nuclei, the pairing effects are included in a self consistent way with a finite range Gogny-type force. In magic nuclei, the RHB+RQRPA model limits to RMF+RRPA. Since

for the superfluid system, enhanced quasiparticle energies enter in RQRPA A matrix, already without residual interaction, the pairing correlations should increase the energy of giant resonances when compared with the RMF+RRPA approach. However, in practical calculations, pairing correlations have very small effect to the position of ISGMR energy (shift of the order 0.1 MeV, as compared with a case without pairing) [137, 136]. The isoscalar resonances in general are less sensitive to the pairing effects than the isovector ones. As it was pointed out in Ref. [137], a larger shift in the isovector case originates from two reasons, a) 2qp energies in superfluid nuclei are larger than the corresponding ph energies obtained without pairing, and b) pp and ph pairs in QRPA produce an enhanced collectivity when compared to the case with only ph configurations. In isovector case residual interaction is repulsive, and both effects contribute to the shift to higher energies. On the other side, for isoscalar excitations with attractive residual interaction, enlarged collectivity lowers the peak energy, canceling the upward shift due to enhanced 2qp energies. Therefore, the shift of the ISGMR energy caused by pairing correlations in superfluid nuclei have very small influence to the extraction of K_{nm} . Much more important effect to ISGMR in RQRPA model is due to the inclusion of Dirac sea states [52, 53]. In the case when the contributions from the Dirac sea are not included in 2qp pairs, ISGMR strength distribution results with a significant shift to lower energies.

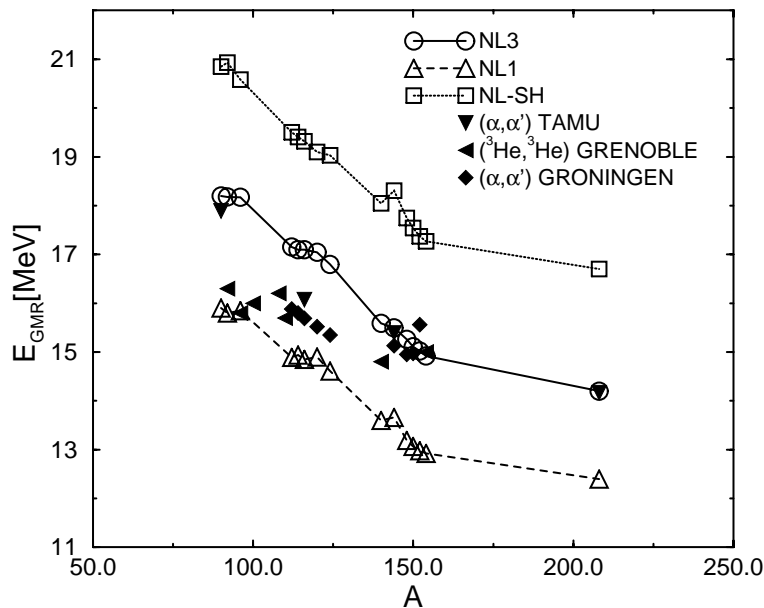


Figure 4.1: Isoscalar monopole strength distributions for NL3, NL1 and NL-SH parameterizations. RHB+RQRPA results are compared with experimental ISGMR energies in ^{90}Zr , ^{116}Sn , ^{144}Sm and ^{208}Pb (TAMU) [138], ^{92}Mo , ^{96}Mo , ^{100}Mo , ^{108}Pd , ^{110}Pd (GRENOBLE) [139], and in a series of Sn and Sm isotopes (GRONINGEN) [140].

In Fig. 4.1 we display the ISGMR centroid energy as a function of mass number for a

series of mostly open-shell nuclei in interval ^{90}Zr - ^{208}Pb . We compare the RQRPA results with measured ISGMR energies, extracted from ($^3\text{He}, ^3\text{He}$) [139] and (α, α') [140] scattering. Systematic overview of different experimental studies on ISGMR is given in Ref. [139]. In our investigation, we focus mainly to Mo, Sn and Sm isotopes. In addition, we compare the data also with a recent experiment, based on the inelastic scattering of 240 MeV α particles, resulting with accurate ISGMR strength distributions in ^{90}Zr , ^{116}Sn , ^{144}Sm and ^{208}Pb [138]. We notice that the NL-SH excitation energies are systematically higher, while NL3 results are in an excellent agreement with experiment in heavier nuclei. In nuclei with $A \leq 124$, NL1 and NL3 have similar agreement with measured values, except in Mo isotopes which lie on the NL1 mass dependence curve. It is important to note that the energies recently obtained as centroids of E0 strength distributions from α scattering [138] are somewhat higher than the ones from previous investigations [139]. For example, in the case of ^{90}Zr , identification of previously unknown tail of the GMR increased the centroid energy by more than 1 MeV [138]. This experiment is in a very good agreement with RQRPA for NL3 effective interaction, also in the lightest nucleus under consideration, ^{90}Zr . It would be important to investigate whether similar effect of energy shift from Ref. [138] could also be expected in the case of Sn isotopes, to increase their centroid energies closer to RQRPA results with NL3 parameterization. The ISGMR energies, com-

Nucleus	RQRPA	QRPA [136]	RPA [29]	EXP [138]
^{90}Zr	18.2	18.6	18.5	17.89±0.20
^{116}Sn	17.5	17.1		16.07±0.12
^{144}Sm	16.3	16.0		15.39±0.28
^{208}Pb	14.2	14.4	14.1	14.17±0.28

Table 4.1: ISGMR centroid energies in MeV, compared with non-relativistic self-consistent RPA(SkM*) [29], QRPA(SGII) and with experimental data from Ref. [138]. NL3 effective interaction has been adopted in RHB+RQRPA calculations.

pared with the non-relativistic (Q)RPA models from Ref. [136, 29], are listed in Table 4.1. RQRPA results on ISGMR seem to be in reasonable agreement with other reports. Since the experimental excitation energies of the ISGMR are best reproduced by the NL3 effective interaction within the RQRPA model, this would imply the value $K_{nm}=271.8$ MeV as the nuclear matter incompressibility. This result is in agreement with another relativistic model, the TDRMFT calculations on a limited number of doubly closed-shell nuclei [56]. The K_{nm} value from our relativistic models is somewhat higher than the results from non-relativistic models based on Gogny force, $K_{nm}=231\pm 5$ MeV [135], and models with generalized Skyrme interaction implying $K_{nm}=240$ MeV [141]. On the other side, recent RRPA analysis with density dependent coupling constants has shown that the experimental excitation energy of the GMR in ^{208}Pb can be reproduced only with interactions in which the nuclear matter compression modulus is in the range $K_{nm}=260$ - 270 MeV [142]. The apparent discrepancy between relativistic and non-relativistic models is still not fully understood.

4.2 The Puzzle of Isoscalar Dipole Strength Distribution

Information on the nuclear matter incompressibility can be extracted from another compression mode, the isoscalar giant dipole resonance (ISGDR). The first order of the isoscalar dipole mode corresponds to a motion of a center of mass, which cannot be associated with a nuclear excitation. Therefore, ISGDR is a second order effect, built on $3\hbar\omega$, or higher configurations. It corresponds to a density oscillation, where the volume of the nucleus remains constant, but a compression wave travels back and forth through the nucleus along a definite direction [143]. An exotic behavior of this type, analogous to a sound wave, has also been addressed as a "squeezing mode". From the scaling model, ISGDR excitation energy is related to the nuclear incompressibility K_A [144], i.e.

$$E_{ISGDR} = \hbar \sqrt{\frac{7 K_A + \frac{27}{25} \epsilon_F}{3 m \langle r^2 \rangle}} \quad (4.2)$$

where ϵ_F corresponds to the Fermi energy. Although the existence of ISGDR resonance has been reported two decades ago, only recently it has been clearly separated from the nearby high-energy octupole resonance, by using inelastic α scattering at and near 0° [145]. Systematics of the present status on ISGDR investigations can be found in Refs. [146, 147, 149, 124]. In Fig. 4.2 we plot the RQRPA isoscalar dipole response to the

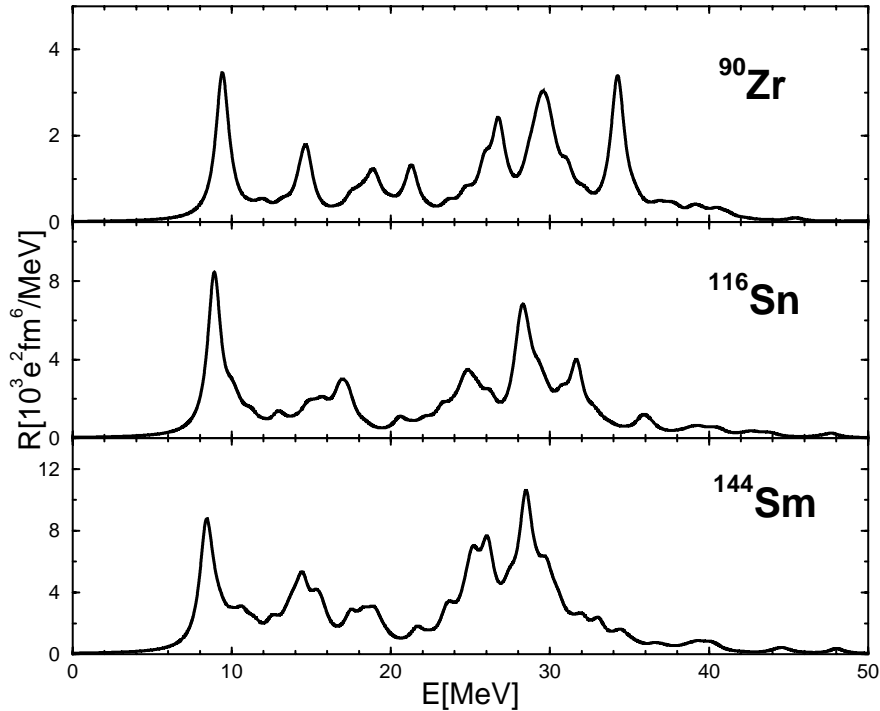


Figure 4.2: RQRPA isoscalar dipole strength distributions in ^{90}Zr , ^{116}Sn , and ^{144}Sm , calculated with NL3 effective interaction.

operator (4.10) in three nuclei: ^{90}Zr , ^{116}Sn , and ^{144}Sm . In addition to the giant resonance in the high energy region, a non-negligible low-lying strength is systematically obtained with centroid energy in the region 10-14 MeV. Recent investigation on ISGDR obtained by using inelastic scattering of α particles on ^{208}Pb [145], and on ^{90}Zr , ^{116}Sn , ^{144}Sm , and ^{208}Pb [148, 124], resulted in a qualitatively similar structure. ISGDR response has been analyzed also in the non-relativistic Hartree-Fock plus RPA framework [64], and with relativistic mean-field plus RPA (RRPA) calculations [50, 52]. In Table 4.2 we compare

Nucleus	E_b	RQRPA	QRPA [64]	EXP [124]
^{90}Zr	22	14.1	14.5	16.2 ± 0.8
^{116}Sn	20	12.0	12.5	14.7 ± 0.5
^{144}Sm	21	12.8	13.5	
^{208}Pb	17	10.7	10.9	12.2 ± 0.6

Table 4.2: RQRPA(NL3) centroid energies (2.57) of the low-lying and high energy region of the ISGDR strength distribution in ^{90}Zr , ^{116}Sn , ^{144}Sm , and ^{208}Pb . The results are compared with non-relativistic Skyrme-type QRPA calculations from Ref. [64] and with experimental values [124]. The boundary energies E_b which separate the low and high energy region are adopted from Ref. [64]. All energies are in MeV units.

Nucleus	E_b	RQRPA	QRPA [64]	EXP [124]
^{90}Zr	22	30.8	30.0	25.7 ± 0.7
^{116}Sn	20	29.3	27.5	23.0 ± 0.6
^{144}Sm	21	28.7	26.6	
^{208}Pb	17	25.4	23.9	19.9 ± 0.8

Table 4.3: The same like Table 4.2, but for the high-energy region corresponding to the ISGDR.

the RQRPA centroid energies (2.57) of the low-lying part of ISGDR strength distribution with other investigations [64, 124]. The boundary E_b between the low and high energy region could vary somewhat among different nuclei. However, to compare results directly with the non-relativistic QRPA, we take the same values for E_b from Ref. [64]. The ISGDR properties of the high energy region are listed in Table 4.3. In addition, ISGDR has been investigated in ^{208}Pb by using inelastic scattering of 400 MeV α particles, where for the first time all instrumental background from single inelastic scattering spectra has been eliminated [149]. The results of this study are compared with theoretical predictions in Table 4.4. All analyzes have shown that: (a) there is a strong disagreement between theory and the reported experimental data on the position of the ISGDR centroid energies, and (b) calculations that predict the splitting of the ISGDR strength distribution into two broad structures, one in the high-energy region above 20 MeV, and one in the low-energy window between 8 MeV and 14 MeV. Effective interactions, both non-relativistic and relativistic, which reproduce the experimental excitation energies of the ISGMR, predict centroid energies of the ISGDR that are ≈ 5 MeV higher than those extracted

	$m_1/m_0(\text{LOW})$	$m_1/m_0(\text{HIGH})$
RRPA(NL3)	10.7	25.4
RPA(SGII) [64]	10.9	23.9
RRPA(NL-C) [59]	≈ 8	24.4
EXP. (α, α') [124]	12.2 ± 0.6	19.9 ± 0.8
EXP. (α, α') [149]	13.0 ± 0.5	23.0 ± 0.5

Table 4.4: ISGDR centroid energies (2.57) of the low and high-lying region in ^{208}Pb calculated by the self-consistent RRPA with NL3 effective force. Results are compared with recent theoretical investigations and measurements (all units are MeV).

from small angle α -scattering spectra. This disagreement between theory and experiment is an order of magnitude larger than for other giant resonances. Another puzzling result is the theoretical prediction of a substantial amount of isoscalar dipole strength in the 8 – 14 MeV region. In Ref. [50] it has been suggested that the RRPA peaks in this region do not correspond to a compression mode, but rather to a kind of toroidal motion with dynamics determined by surface effects. In a very recent article [124], Clark *et al.* reported new experimental data on the isoscalar dipole strength functions in ^{90}Zr , ^{116}Sn , and ^{208}Pb , measured with inelastic scattering of α particles at small angles. They found that the isoscalar E1 strength distribution in each nucleus consists of a broad component at $E_x \approx 114/A^{1/3}$ MeV containing approximately 100% of the E1 EWSR, and a narrower one at $E_x \approx 72/A^{1/3}$ MeV containing 15 – 28 % of the total isoscalar E1 strength. The higher component is identified as the E1 compression mode, whereas the lower component may be the new mode predicted by the RRPA analysis of Ref. [50]. In the present work we suggest that the observed low-lying E1 strength may correspond to the toroidal giant dipole resonance (TGDR).

4.3 Toroidal Giant Dipole Resonances

The role of toroidal multipole form factors and moments in the physics of electromagnetic and weak interactions has been extensively discussed in Refs. [150] and [151]. They appear in multipole expansions for systems containing convection and induction currents. In particular, the multipole expansion of a four-current distribution gives rise to three families of multipole moments: charge moments, magnetic moments and electric transverse moments. The later are related to the toroidal multipole moments and result from the expansion of the transverse electric part of the current. The toroidal dipole moment, in particular, describes a system of poloidal currents on a torus. Since the charge density is zero for this configuration, and all the turns of the torus have magnetic moments lying in the symmetry plane, both the charge and magnetic dipole moments of this configuration are equal to zero. The simplest model is an ordinary solenoid bent into a torus.

Vortex waves in nuclei were analyzed in a hydrodynamic model [152]. By relaxing the assumption of irrotational motion, in this pioneering study solenoidal toroidal vibrations were predicted, which correspond to the toroidal giant dipole resonance at excitation

energy $E_x \approx (50-70)/A^{1/3}$ MeV. It was suggested that the vortex excitation modes should appear in electron backscattering. In the framework of the time-dependent Hartree-Fock theory, the isoscalar 1^- toroidal dipole states were also studied by analyzing the dynamics of the moments of the Wigner transform of the density matrix [153].

In this work the toroidal dipole strength distributions are calculated in the relativistic random phase approximation (RRPA). A self-consistent calculations ensures that the same correlations which define the ground-state properties, also determine the behavior of small deviations from the equilibrium. Two points are essential for the successful application of the RRPA in the description of dynamical properties of finite nuclei: (i) the use of effective Lagrangians with non-linear terms in the meson sector, and (ii) the fully consistent treatment of the Dirac sea of negative energy states. In particular, in Ref. [53] it has been shown that configurations which include negative-energy states have an especially pronounced effect on isoscalar excitation modes.

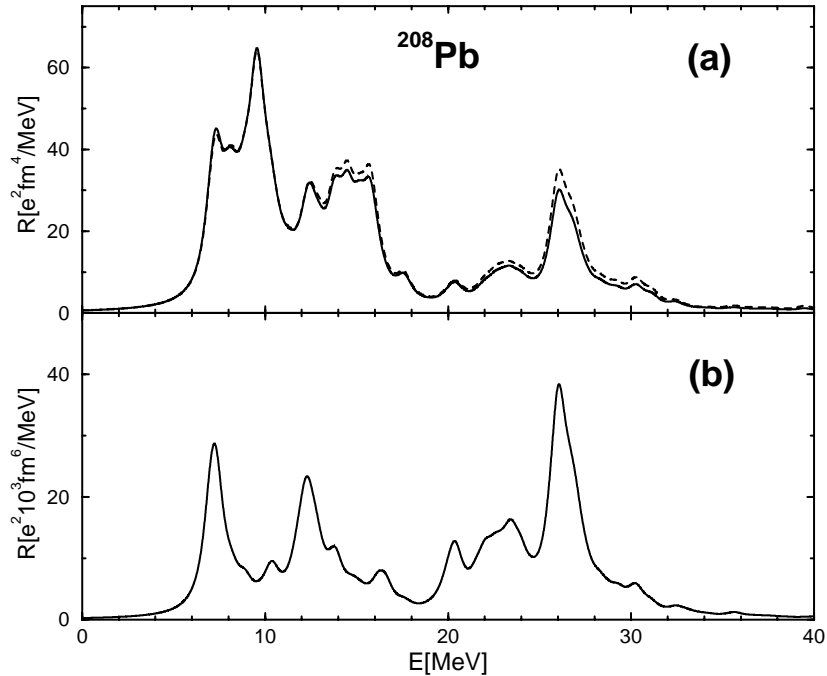


Figure 4.3: (a) Toroidal dipole strength distributions in ^{208}Pb , calculated without (dashed) and with (solid) projection of spurious center-of-mass components. (b) ISGDR strength distributions in ^{208}Pb .

In Fig. 4.3(a) we display the RRPA toroidal dipole strength distribution for ^{208}Pb . As the transition operator in Eq. 2.36 we use the isoscalar toroidal dipole operator defined as [150]

$$\hat{Q}_{1\mu}^{T=0} = -\sqrt{\pi} \int \left[r^2 \left(\vec{Y}_{10\mu}^* + \frac{\sqrt{2}}{5} \vec{Y}_{12\mu}^* \right) - \langle r^2 \rangle_0 \vec{Y}_{10\mu}^* \right] \cdot \vec{J}(\vec{r}) d^3r. \quad (4.3)$$

In the relativistic framework the expression for the the isoscalar baryon current reads

$$J^\nu = \sum_{i=1}^A \bar{\psi}_i \gamma^\nu \psi_i, \quad (4.4)$$

where the summation is over all occupied states in the Fermi sea. The resulting toroidal dipole operator is

$$\hat{Q}_{1\mu}^{T=0} = -\sqrt{\pi} \sum_{i=1}^A \left[r_i^2 \left(\vec{Y}_{10\mu}^*(\Omega_i) + \frac{\sqrt{2}}{5} \vec{Y}_{12\mu}^*(\Omega_i) \right) \cdot \vec{\alpha}_i - \langle r^2 \rangle_0 \vec{Y}_{10\mu}^*(\Omega_i) \cdot \vec{\alpha}_i \right], \quad (4.5)$$

where $\vec{Y}_{l\mu}$ denotes a vector spherical harmonic, and $\vec{\alpha}$ are the Dirac α -matrices. The calculations have been performed with the self-consistent Dirac-Hartree plus relativistic RPA. The effective mean-field Lagrangian contains nonlinear meson self-interaction terms, and the configuration space includes both particle-hole pairs, and pairs formed from hole states and negative-energy states. The inclusion of the term $-\langle r^2 \rangle_0 \vec{Y}_{10\mu}^*$ in the operator ensures that the TGDR strength distributions do not contain spurious components that correspond to the center-of-mass motion [152]. In Fig. 4.3(a) we compare the toroidal strength distributions calculated without (dashed) and with (solid) the inclusion of this term in the operator.

The projection of spurious center-of-mass motion components can also be performed by subtracting the spurious transition current, following a procedure similar to that adopted in Refs. [64, 154] for the ISGDR. The toroidal dipole strength distribution can be written as

$$R(E) = \left| \int d^3r \delta\vec{j}(\vec{r}) \cdot \vec{Q}(\vec{r}) \right|^2 \quad (4.6)$$

where $\vec{Q}(\vec{r})$ is the vector toroidal operator, and $\delta\vec{j}(\vec{r})$ is the transition current

$$\delta\vec{j}(\vec{r}) = j_-(r) \vec{Y}_{10\mu}^*(\Omega) + j_+(r) \vec{Y}_{12\mu}^*(\Omega). \quad (4.7)$$

The radial functions $j_-(r)$ and $j_+(r)$ are defined in Ref. [155]. We have verified that identical strength distributions (solid curve in Fig. 4.3) are obtained when: (a) the transition current (4.7) is used and the toroidal operator is corrected by including the term $-\langle r^2 \rangle_0 \vec{Y}_{10\mu}^*$, or (b) this term is not included in the operator and the spurious component is subtracted from the transition current at each energy

$$\delta\vec{j}(\vec{r}) - a\rho_0\vec{e}_z. \quad (4.8)$$

The second term in this expression is the spurious transition current [156]. ρ_0 is the ground-state density and \vec{e}_z denotes the unit vector in the direction of the center-of-mass motion. The energy dependent coefficient a is determined by the condition that the integral of the transition current over the nucleus should vanish at each energy

$$\int d^3r \left(\delta\vec{j}(\vec{r}) - a\rho_0\vec{e}_z \right) = 0. \quad (4.9)$$

The strength distributions in Fig. 4.3 have been calculated with the NL3 [80] effective interaction. In Ref. [56] it has been shown that isoscalar giant monopole resonances calculated with this effective force ($K_{\text{nm}} = 271.8$ MeV) are in excellent agreement with experimental data, and in Ref. [50] this interaction was used in the RPA analysis of the ISGDR. By using effective interactions with different values of the nuclear matter compressibility modulus, it was shown that only the high-energy (above 20 MeV) portion of the isoscalar dipole strength distribution corresponds to a compression mode. The same effect is observed for the toroidal strength function: the position of the peaks in the low-energy region (below 20 MeV) depends only weakly on the incompressibility, while the structure in the high-energy region is strongly affected by the choice of the compression modulus of the interaction. In Fig. 4.3(b) we plot the strength function of the isoscalar dipole compression operator [50]

$$\hat{Q}_{1\mu}^{T=0} = \sum_{i=1}^A \gamma_0 (r^3 - \frac{5}{3} \langle r^2 \rangle_0 r) Y_{1\mu}(\theta_i, \varphi_i). \quad (4.10)$$

We note that both dipole strength distributions, toroidal in Fig. 4.3(a) and compressional in Fig. 4.3(b), display two broad structures: one at low energies between 8 and 15 MeV, and one in the high-energy region 25 – 30 MeV. Obviously, one could expect a strong coupling between the two isoscalar 1^- modes. This coupling becomes even more evident if one rewrites the expression in square brackets of the toroidal operator (4.3) as [152]

$$\nabla \times (\vec{r} \times \nabla) (r^3 - \frac{5}{3} \langle r^2 \rangle_0 r) Y_{1\mu}, \quad (4.11)$$

and compares it with the isoscalar dipole operator of the compression mode (4.10). The relative position of the two resonance structures will, therefore, depend on the interaction between the toroidal and compression modes.

In Fig. 4.4 we display the RPA toroidal dipole strength distributions in ^{90}Zr , ^{116}Sn , and ^{208}Pb , calculated with the NL3, NL1 and NL-SH effective interactions. In all three nuclei a broad, strongly fragmented structure is found in the low-energy region, where "the low-lying component of the ISGDR" has been observed [124]. The strength distributions vary only slightly in calculations with different effective force parameterizations. The toroidal strength distributions in the low-energy region should be compared with the experimental centroid energies of the "low-lying component" [124]: 16.2 ± 0.8 MeV for ^{90}Zr , 14.7 ± 0.5 MeV for ^{116}Sn , and 12.2 ± 0.6 MeV for ^{208}Pb . The calculated peaks in the high-energy region, on the other hand, correspond to the compression mode. The dynamics of the solenoidal toroidal vibrations is illustrated in Fig. 4.5, where we plot the velocity fields for the four most pronounced peaks of the toroidal dipole strength distributions in ^{116}Sn (see Fig. 4.4). The velocity distributions are derived from the corresponding transition currents, following the procedure described in Ref. [155]. A vector of unit length is assigned to the largest velocity. All the other velocity vectors are normalized accordingly. Since the collective flow is axially symmetric, we plot the velocity field in cylindrical coordinates. The z -axis corresponds to the symmetry axis of a torus. We note that the two lowest peaks at 8.82 MeV and 10.47 MeV are completely dominated

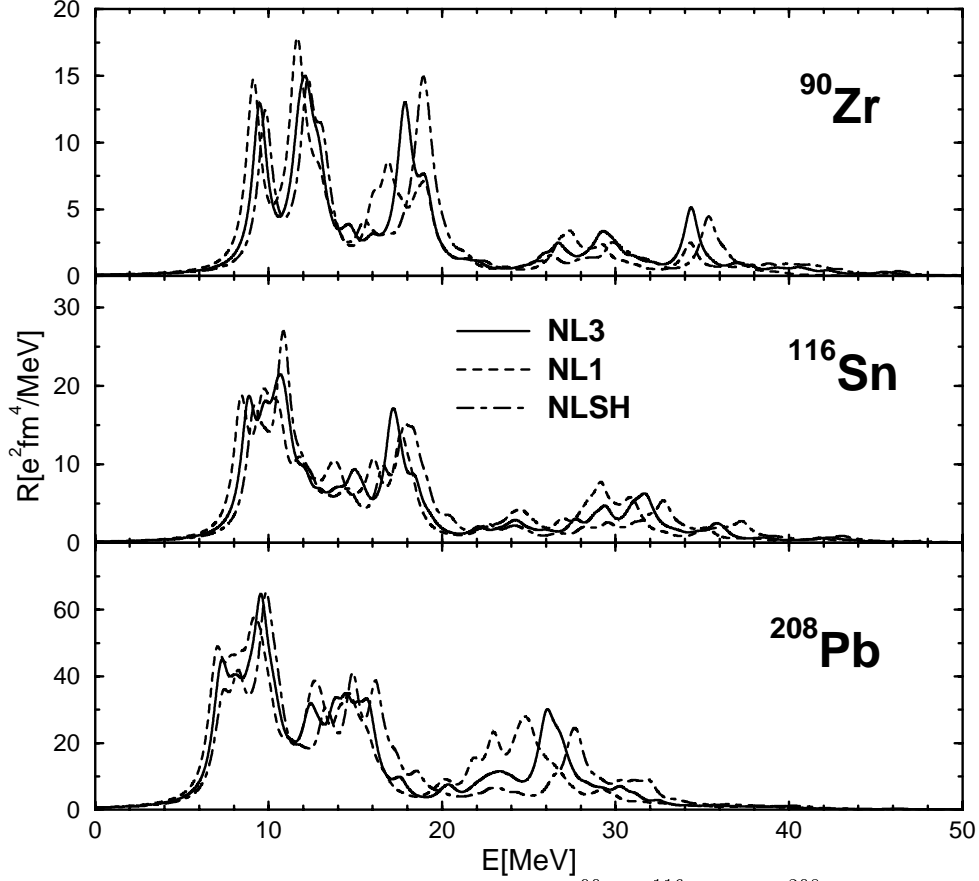


Figure 4.4: Toroidal dipole strength distributions in ^{90}Zr , ^{116}Sn and ^{208}Pb , calculated with the NL3, NL1 and NL-SH effective interaction.

by vortex collective motion. The velocity fields in the (z, r_{\perp}) plane correspond to poloidal currents on a torus with vanishing inner radius. The poloidal currents determine the dynamical toroidal moment. The high-energy peak at 30.97 MeV displays the dynamics of dipole compression mode. The "squeezing" compression mode is identified by the flow lines which concentrate in the two "poles" on the symmetry axis. The velocity field corresponds to a density distribution which is being compressed in the lower half plane, and expands in the upper half plane. The centers of compression and expansion are located on the symmetry axis, at approximately half the distance between the center and the surface of the nucleus. Finally, the intermediate peak at 17.11 MeV clearly displays the coupling between the toroidal and compression dipole modes. A very similar behavior of the velocity distributions as function of excitation energy is also observed for ^{90}Zr and ^{208}Pb .

We suggest, therefore, that the recently observed "low-lying component of the isoscalar dipole mode" [124] might in fact correspond to the toroidal giant dipole resonance. By employing the fully consistent relativistic random phase approximation, in Ref. [50] and in the present analysis we have shown that the toroidal dipole strength is concentrated in the low-energy region around 10 MeV, while the isoscalar dipole excitations in the high-

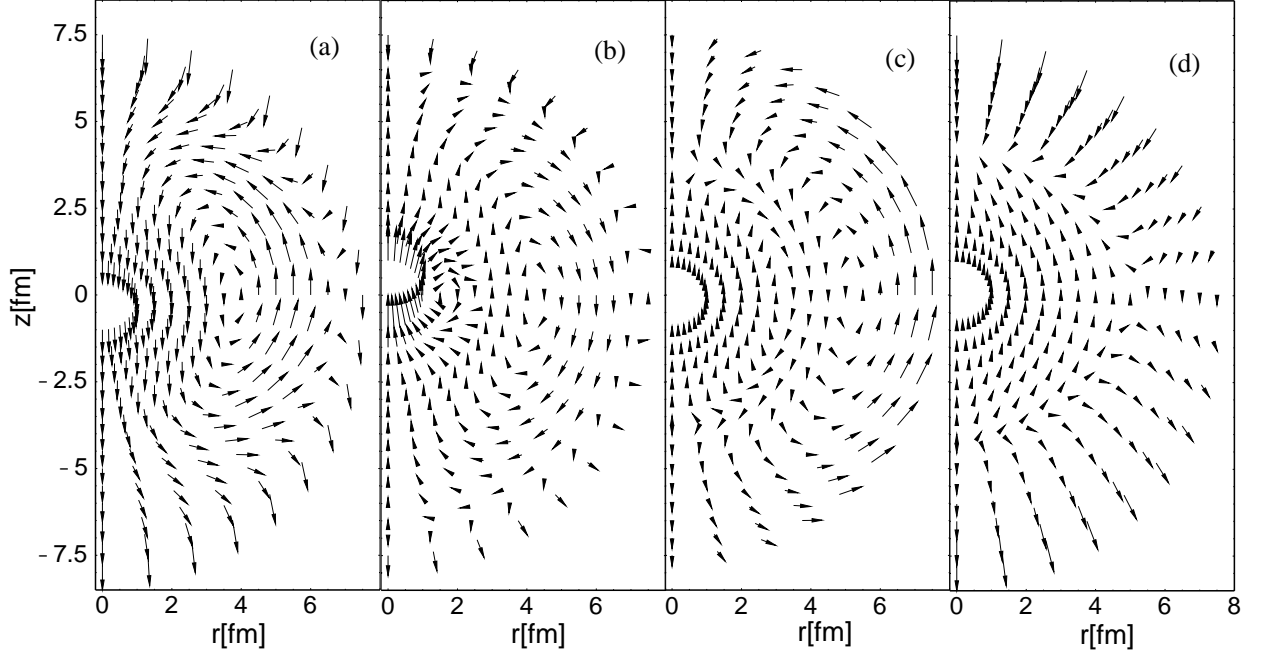


Figure 4.5: Velocity distributions for the most pronounced dipole peaks in ^{116}Sn (see Fig. 4.4). The velocity fields correspond to the peaks at 8.82 MeV (a), 10.47 MeV (b), 17.11 MeV (c), and 30.97 MeV (d).

energy region above 20 MeV correspond to the "squeezing" compression mode. States in the intermediate region display a strong mixing between the two dipole resonances. The pronounced coupling between the toroidal resonance and the ISGDR, predicted by the RRPA calculations, might also explain the strong discrepancy between theory and the experimental position of the ISGDR centroid energies [124, 154, 64, 50]. Namely, the interaction causes a repulsion of the two 1^- isoscalar modes, i.e. it pushes the ISGDR to higher energies and pulls the TGDR to lower energies. This effect would explain the observation of Ref. [124] that: "The centroids of the higher (compression) mode calculated with interactions which reproduce GMR energies are about 4 MeV higher than the experimental centroids, whilst the calculated centroids for the lower mode lie 1-2 MeV below the experimental values."

Chapter 5

Proton-Neutron Relativistic Quasiparticle RPA

Collective spin and charge-exchange excitations in atomic nuclei in the past have been a subject of many theoretical and experimental studies [157]. Especially interesting is the spin-flip isospin-flip mode, known as the Gamow-Teller resonance (GTR), composed from the proton-quasiparticle - neutron-quasiparticle 1^+ excitations, mainly from the neutron orbits $j_> = l + 1/2$ to the spin-orbit partners $j_< = l - 1/2$ on the proton side. It had been predicted in 1962 [158], and in 1975 was experimentally discovered in (p, n) charge-exchange reactions at intermediate energies [159]. Reliable knowledge on GTR mode provides valuable information on the isovector properties of the effective nucleon-nucleon interaction. In addition, GT^\pm strength distributions are essential for the understanding of nucleosynthesis. In particular, the low-lying GT strength is directly related to the β^\pm -decay rates, as well as to the electron-capture processes leading to the stellar collapse and supernova evolution. Recent developments in experimental methods using radioactive beams suggested that the spin-flip isospin-flip excitation modes could be employed to measure the neutron-skin thickness [160].

The measured GT strength distribution appeared to be quenched by more than 20% when compared to a model independent sum rule. Theoretical investigation suggested that GTR quenching could originate from (i) couplings to the $2p - 2h$ states [161], and (ii) the contributions of Δ -isobar-particle nucleon-hole configurations at higher excitation energies [162, 163]. Recent charge exchange (p, n) experiments indicated that only a small fraction of the GT quenching originates from $\Delta - h$ transitions [164].

The GT^\pm excitations and related β^\pm -decays have in the past been investigated from two major theoretical directions: (i) the shell model and (ii) non-relativistic proton-neutron quasiparticle random approximation. In the large-basis shell model one assumes that the nuclear structure properties are determined by the valence nucleons, occupying several different single-particle states which are partially filled [165]. The experimental data on charge-exchange excitations in light and medium-light nuclei have been very successfully explained within shell-model calculations. However, as the number of nucleons under consideration increases, the dimension of shell-model Hamiltonian becomes too large for practical calculations. Recently, the large scale shell-model has been extended to

the region of pf -shell nuclei $A = 45 - 65$, in order to reproduce experimentally available Gamow-Teller strength distributions and nuclear decay half-lives [166]. The GT response has also been reproduced in the iron region nuclei by using the shell model Monte Carlo (SMMC) approach, which appeared rather flexible and allowed more realistic calculations than the usual methods using direct diagonalization [167].

On the other hand, the pn-QRPA models are also capable of treating nuclei in regions which are presently beyond the scope of the most sophisticated shell-model approaches. The pn-QRPA excitations are built from the 2qp creation and annihilation operators acting on the ground state, obtained from different mean-field models. The first pioneering work on this subject was based on the simple separable forces by Halbleib and Sorensen [168]. In further developments, the zero-range interactions with BCS have been employed, with inclusion of the particle-particle interaction in the RPA residual interaction, which appeared to be rather important for β -decay matrix elements [169].

Since in medium and heavy nuclei the proton and neutron Fermi levels are well separated from one another, the proton-neutron pairing has usually been neglected. However, within the new radioactive beam studies, unstable nuclei close to $N=Z$ line have become more accessible, renewing the interest in the role of pn pairing. The GT strengths have been studied as a function of the particle-particle strength parameter, in the QRPA approach with pn pairing, where the quasi-particle operators are mixed combinations of both neutron and proton creation and annihilation operators [170]. Most investigations have been based on Skyrme interactions [171, 172, 173, 174]. Recently a pn-QRPA model involving Skyrme forces and finite-range proton-neutron pairing, have been employed to investigate the β -decay rates for neutron-rich nuclei at the r-process waiting points [39]. The low-lying part of GT^- strength distribution is closely related to the β^- transition rates. However, since the proton-neutron $T=0$ pairing also contributes to the GT low-energy tail, in practical calculations the $T=0$ pairing strength is given by a free parameter that is fitted to the β -decay half-lives [175]. A consistent treatment, involving both ph and pp interactions, appeared to be essential to resolve the discrepancies between the theoretical models and experimental results for β -decay and electron capture. In the cases of both 0ν and 2ν double β -decay, the inclusion of the pp matrix elements in the residual interaction resulted in a significant suppression of the decay rates [176].

In the microscopic picture, where the effective nuclear interaction is described by the meson exchange, the spin and isospin dependence is included via ρ -meson and pion. The pion plays an important role in unnatural-parity spin-flip isospin-flip excitations. Since it has relatively small mass, which can be extracted from experimental data, it mediates the interaction over large distances. The non-relativistic models based on the ρ, π -meson exchange have already been implemented in studies of charge-changing resonances [177]. In the relativistic description of spin-flip and isospin-flip excitations, we in fact employ fields with the same degrees of freedom in the residual interaction.

5.1 Matrix Equations of the pn-RQRPA in the RHB Canonical Basis

The use of relativistic mean-field models to study the charge-exchange excitations in finite nuclei has been rather limited in the past. The first relativistic RPA calculations of the isobaric analog and Gamow-Teller resonances has only been performed recently [66]. However, this investigation was constrained to the small configuration space in the closed-shell nuclei only. Furthermore, the contributions from the ph configurations including transitions to the negative-energy Dirac sea have so far been neglected. In very recent work, however, it has been shown that in the relativistic models the antinucleon degrees of freedom play an important role in the non-energy weighted Gamow-Teller sum rules [68].

Following the investigation in Ref. [66], we formulate the relativistic proton-neutron quasiparticle RPA (pn-RQRPA) for its use in open-shell nuclei, with possible extension to regions away from the valley of β -stability. In addition, we expand the pn-RQRPA model to include the charge-changing 2qp pairs which also include the antiparticle states from the Dirac sea. We start from the 0^+ initial ground state of an even-even nucleus, composed from the discrete states of the canonical RHB single-particle basis. In this way, we have included both the self-consistent relativistic mean field, which includes the long range ph correlations, and the pairing field which encloses pp correlations (details of the ground state calculations are given in Chapter 3). By employing the charge exchange operators

$$\tau_{\pm} = \frac{1}{\sqrt{2}} (\tau_x \pm i\tau_y) \quad (5.1)$$

to the ground state of a parent nucleus, two quasiparticle excitations are built in the isobaric adjacent odd-odd nucleus. Here τ_+ (τ_-) is the isospin raising (lowering) operator responsible for changing a proton to a neutron (and vice versa). The charge changing transition is induced by a phonon creation operator defined as,

$$\hat{Q}_v^{+(JM)} = \sum_{\pi\nu} X_{\pi\nu}^{v,J} \hat{O}_{\pi\nu}^{+(JM)} - (-1)^{J+M} Y_{\pi\nu}^{v,J} \hat{O}_{\pi\nu}^{(J-M)}, \quad (5.2)$$

where \hat{O} corresponds to the coupled combination of proton (π) and neutron (ν) quasiparticle creation operators,

$$\hat{O}_{\pi\nu}^{+(JM)} = \sum_{m_{\pi} m_{\nu}} \langle j_{\pi} m_{\pi} j_{\nu} m_{\nu} | JM \rangle \alpha_{j_{\pi} m_{\pi}}^+ \alpha_{j_{\nu} m_{\nu}}^+. \quad (5.3)$$

When acting with the phonon creation operator (5.2) on the canonical RHB ground state $|\phi\rangle$, an excited state is obtained, i.e. $\hat{Q}_v^{+(JM)}|\phi\rangle = |v\rangle$, while $\hat{Q}_v^{(JM)}|\phi\rangle = 0$. From the equation of motion method [85], we gain the relativistic proton-neutron quasiparticle random phase approximation equations in the angular momentum coupled representation,

$$\begin{pmatrix} A^J & B^J \\ B^{*J} & A^{*J} \end{pmatrix} \begin{pmatrix} X^{v,JM} \\ Y^{v,JM} \end{pmatrix} = E_v \begin{pmatrix} 1 & 0 \\ 0 & -1 \end{pmatrix} \begin{pmatrix} X^{v,JM} \\ Y^{v,JM} \end{pmatrix}, \quad (5.4)$$

where the matrices A and B are given by

$$A_{\pi\nu\pi'\nu'}^J = \langle \phi | [\hat{O}_{\pi\nu}^{(JM)}, [H, \hat{O}_{\pi'\nu'}^{+(JM)}]] | \phi \rangle \quad (5.5)$$

and

$$B_{\pi\nu\pi'\nu'}^J = -\langle \phi | [\hat{O}_{\pi\nu}^{(JM)}, [H, (-1)^{(J+M)} \hat{O}_{\pi'\nu'}^{(J-M)}]] | \phi \rangle. \quad (5.6)$$

As the RHB Hamiltonian in the canonical basis is not diagonal, we see that from the one-body operator,

$$H^{11} = \sum_{\kappa\lambda} H_{\kappa\lambda}^{11} \alpha_{\kappa}^{\dagger} \alpha_{\lambda} \quad (5.7)$$

we have to include not only the unperturbed 2qp energies on the diagonal of the A -matrix, but also the additional unperturbed non-diagonal terms, i.e.

$$A_{\pi\nu\pi'\nu'}^{J11} = H_{\pi\pi'}^{11} \delta_{\nu\nu'} + H_{\nu\nu'}^{11} \delta_{\pi\pi'} \quad (5.8)$$

$$B_{\pi\nu\pi'\nu'}^{J11} = 0 \quad (5.9)$$

From H^{22} and H^{40} two-body terms in Hamiltonian (2.15), follows the interaction part in pn-RQRPA matrices,

$$A_{\pi\nu\pi'\nu'}^J = \frac{1}{2} (\eta_{\pi\nu}^+ \eta_{\pi'\nu'}^+ + \eta_{\pi\nu}^- \eta_{\pi'\nu'}^-) V_{\pi\nu'\nu\pi'}^{phJ} + \frac{1}{2} (\xi_{\pi\nu}^+ \xi_{\pi'\nu'}^+ + \xi_{\pi\nu}^- \xi_{\pi'\nu'}^-) V_{\pi\nu\pi'\nu'}^{ppJ} \quad (5.10)$$

$$B_{\pi\nu\pi'\nu'}^J = \frac{1}{2} (\eta_{\pi\nu}^+ \eta_{\pi'\nu'}^+ - \eta_{\pi\nu}^- \eta_{\pi'\nu'}^-) V_{\pi\nu'\nu\pi'}^{phJ} + \frac{1}{2} (\xi_{\pi\nu}^+ \xi_{\pi'\nu'}^+ - \xi_{\pi\nu}^- \xi_{\pi'\nu'}^-) V_{\pi\nu\pi'\nu'}^{ppJ} \quad (5.11)$$

where the occupation probabilities of the canonical basis single-particle states are included within $\eta_{\pi\nu}^{\pm}$ and $\xi_{\pi\nu}^{\pm}$ in the same way as in Eqs. (2.21) and (2.22). V^{ph} and V^{pp} correspond to the ph and pp residual interaction, respectively. The isospin part of the isoscalar one-boson exchange interaction,

$$V_{\tau}^{T=0} = \mathbf{1}_1 \mathbf{1}_2 \quad (5.12)$$

actually gives no contribution to the V^{ph} , since

$$\langle \pi\nu' | \mathbf{1}_1 \mathbf{1}_2 | \nu\pi' \rangle = 0. \quad (5.13)$$

On the other hand, from the isovector type of interaction,

$$V_{\tau}^{T=1} = \vec{\tau}_1 \vec{\tau}_2 = 4t_{1z}t_{2z} + 2t_{1+}t_{2-} + 2t_{1-}t_{2+} \quad (5.14)$$

we get non-vanishing isospin two-body matrix elements, i.e.

$$\langle \pi\nu' | \vec{\tau}_1 \vec{\tau}_2 | \nu\pi' \rangle = 2. \quad (5.15)$$

Therefore, in the pn-RQRPA model, only the isovector fields actually contribute to the ph matrix elements of the residual interaction. In the present study, the interaction is built on the following degrees of freedom for the one-boson exchange: (i) the isovector vector field $\vec{\rho}$, and (ii) the isovector pion field $\vec{\pi}$ with the pseudovector coupling to the nucleon. The pseudovector coupling defined by the interaction part of the Lagrangian density,

$$\mathcal{L}_\pi = -\frac{f_\pi}{m_\pi} \bar{\psi} \gamma_5 \gamma_\mu \partial^\mu \vec{\pi} \vec{\tau} \psi \quad (5.16)$$

is preferred over the pseudoscalar one, since it provides a better description of π -nucleon scattering data. The mass of the pion and its coupling constant are fixed to the well known experimental values,

$$m_\pi = 138.0 \text{ MeV} \quad \frac{f_\pi^2}{4\pi} = 0.08. \quad (5.17)$$

More details about the evaluation of the corresponding matrix elements are given in Appendix A.

Additional contributions to the pn-RQRPA matrices come from the proton-neutron pairing correlations. Since the proton and neutron Fermi surfaces in neutron-rich nuclei are far apart, this channel of interaction has a negligible contribution in the ground state calculations [39]. On the other side, in the pn-RQRPA the like particle pairing gives no contribution to the matrix elements. The $T = 1$ component of the pn interaction has a very small effect [39], while $T = 0$ pn pairing correlations can be adjusted with a free parameter, since it has no contribution on the RHB level. Following Ref. [39] we take for the pairing interaction a finite range Gogny-type force composed of two Gaussians having different ranges. The strength of the interaction is given by the free parameter V_0 . This particular selection of the force appeared to be very important, since a delta force that successfully describes the like-particle pairing may result in divergencies at the QRPA level as the configurational space is increased [39].

The transition strength for the operator $Q_{\beta^\pm}^{(F,GT)}$ inducing the charge exchange excitations of the Fermi (isospin flip) or Gamow-Teller (isospin-flip and spin-flip) type is given by

$$B_{\beta^\pm}^{(F,GT)}(E_v) = \frac{1}{2J_i + 1} \left| \sum_{\pi\nu} \langle \pi \parallel Q_{\beta^\pm}^{(F,GT)} \parallel \nu \rangle (X_{\pi\nu}^v u_\pi v_\nu + Y_{\pi\nu}^v v_\pi u_\nu) \right|^2, \quad (5.18)$$

where E_v and (X^v, Y^v) are eigen-solutions of the pn-RQRPA equation (5.4), while $u_{\pi(\nu)}$ and $v_{\pi(\nu)}$ correspond to the occupation probabilities for the proton (neutron) single-particle states in the RHB canonical basis. The discrete strength distribution is folded by a Lorentzian function (2.47) in the usual way by employing the width parameter $\Gamma = 1 \text{ MeV}$.

Next we test the pn-RQRPA model in the limit of a few closed shell nuclei. In actual calculations, the canonical basis is truncated by imposing a cut-off in 2qp energies obtained

from the diagonal matrix elements of the one-quasiparticle Hamiltonian H^{11} . We have adopted the NL3 effective interaction in the ph channel of the residual interaction [80].

5.2 An Illustrative Example - Isobaric Analog Resonances

In the first step, we wish to check the present pn-RQRPA model in the case of isobaric analog resonance (IAR). It is the simplest charge-exchange excitation mode, detected almost 40 years ago in the proton elastic scattering from heavy nuclei, and interpreted as a mode composed from the transitions between isobaric analog states of the compound nucleus composed from the target nucleus with an additional proton [178]. If the nuclear interaction were charge-independent, the isobaric analog ground states would be degenerate among isobaric partners. However, some parts of the nuclear interaction (e.g. Coulomb interaction) break the isospin symmetry in the nuclear Hamiltonian, reflecting this property in the IAR mode. The IAR excitation energies, as well as its total widths, have so far been investigated in many different microscopic models ([179, 157, 180, 66] and references therein).

By using the present pn-RQRPA model, we calculate the IAR strength distributions, i.e. the $J^+ = 0^+$ mode generated by the transition operator of the Fermi type,

$$Q_{\beta^\pm}^F = \sum_{i=1}^A \tau_{\pm}. \quad (5.19)$$

In Fig. 5.1 we display the pn-RRPA response to the operator (5.19) for ^{48}Ca , ^{90}Zr and ^{208}Pb . The main contribution to the resonance comes from transitions between isobaric analog states. Whereas for the β^- transitions, the necessary proton isobaric analog states are unoccupied, this is not the case for the neutron states in β^+ excitations. Therefore here, due to the Pauli blocking, only the $Q_{\beta^-}^F$ operator actually gives some significant contribution to IAR. All excitation energies are evaluated with respect to the target ground state of listed nuclei. Consequently this means that we have to add to the measured excitation energy of product nuclei both the mass difference between target and product nucleus, and the difference among the neutron and proton mass [172].

The strength distributions consist of a single dominant IAR peak which corresponds to the coherent superposition of $\pi p - \nu h$ (or proton-neutron 2qp) excitations. In Table 5.1 the excitation energies of present model are compared with other RPA studies [172, 66], as well as with the (n, p) scattering data for ^{48}Ca [181], ^{90}Zr [182, 164], and ^{208}Pb [183]. In particular, for the transition $^{208}\text{Pb}(n, p)^{208}\text{Bi}$ we obtain for IAR energy with respect to the target nucleus, $E=17.91$ MeV, that is reasonably close to the experimental value $E=18.83$ MeV [184, 183]. A similar IAR excitation energy in ^{208}Bi ($E=18.64$ MeV for SGII and 18.49 MeV for SIII effective interaction), has been obtained in a recent microscopic model formulated using the self-consistent Hartree-Fock + RPA, employing configurations with coupling to the continuum, and additionally including ph plus phonon configurations [172]. In the case of ^{208}Bi , similarly good agreement with experiment

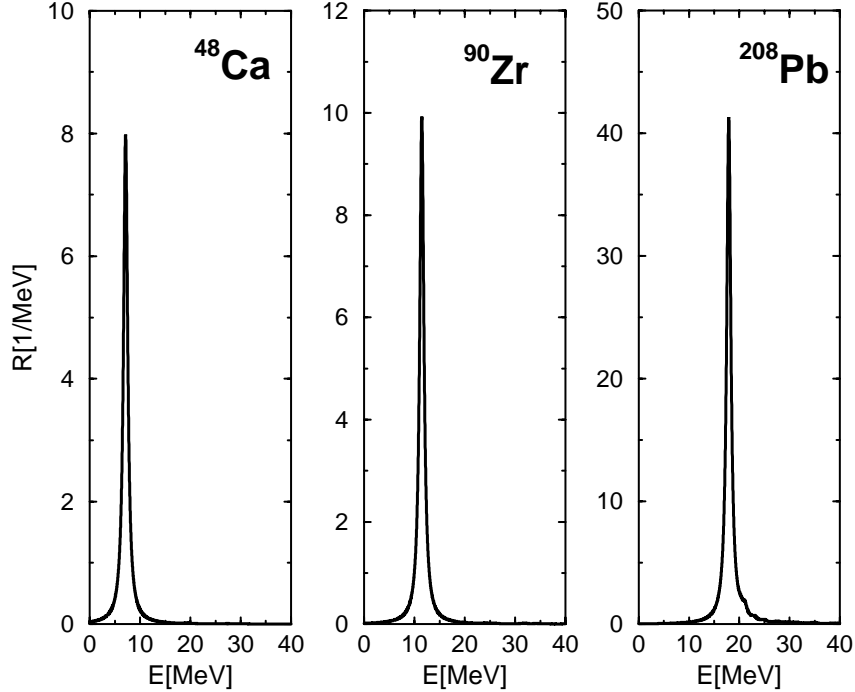


Figure 5.1: pn-RRPA strength distributions of the isobaric analog resonances in various closed-shell nuclei, evaluated with the NL3 effective interaction.

has been achieved with another recent self-consistent continuum Hartree-Fock+Tamm-Dancoff approximation model, where IAR is located at energy $E=18.8$ MeV [174]. The pn-RRPA excitation properties of IAR in ^{48}Ca and ^{90}Zr are very close to the measured values [181]. Another important quantity to be verified is the well known Ikeda sum rule [157] which relates the total sum of B^F strength, i.e. the non-energy weighted sum rule for the Fermi-type β^- decay, to the number of excess neutrons in nucleus:

$$S_{\beta^-}(F) = N - Z. \quad (5.20)$$

It is a completely model independent quantity. Even though the strength function $B_{\beta^-}^F(E)$ depends directly on the nuclear structure properties of target nuclei, the sum rule infers that the summed IAR strength depends only on the proton and neutron number, without any additional information as to how nucleons actually build the nuclear ground state of the target nuclei. The Ikeda sum rule provides an important insight into the completeness of the measured β^- strength. Furthermore, if the selected configuration space in the theoretical model is complete, this sum rule should hold exactly. In Fig. 5.2 we plot the pn-RRPA running sum

$$S_{\beta^-}^F(E) = \sum_{E_v < E} B_{\beta^-}^F(E_v) \quad (5.21)$$

where the IAR strength is summed up to the selected maximal energy E . In the cases of ^{48}Ca , ^{90}Zr , and ^{208}Pb , the Ikeda sum rules (5.20) (plotted with horizontal dotted

		pn-RRPA(NL3)	RRPA [66]	RPA(SGII) [172]	EXP.
²⁰⁸ Pb	\bar{E} [MeV]	17.91	18.6	18.64	18.83±0.02
	$\sum S(E)$ [%]	100.1	99	97	≈ 100
⁹⁰ Zr	\bar{E} [MeV]	11.45	11.9		12.0±0.2
	$\sum S(E)$ [%]	100.4	101.3		≈ 100
⁴⁸ Ca	\bar{E} [MeV]	7.15	7.48		7.17
	$\sum S(E)$ [%]	100.2	100.4		≈ 100

Table 5.1: Mean energy \bar{E} and the summed strength $S_{\beta^-}(F)$ in the units of Ikeda sum rule $N - Z$ for the isobaric analog resonances in several nuclei, by using the NL3 effective interaction. Results are compared with the RRPA [66] and Skyrme-type RPA [172] calculations, as well as with the experimental data for ⁴⁸Ca [181], ⁹⁰Zr [182, 164], and ²⁰⁸Pb [183]. In (ρ, π) -exchange non-relativistic model, for ²⁰⁸Pb $E(\text{IAR})=17.0$ MeV, whereas exp. $E(\text{IAR})=18.0$ MeV [177].

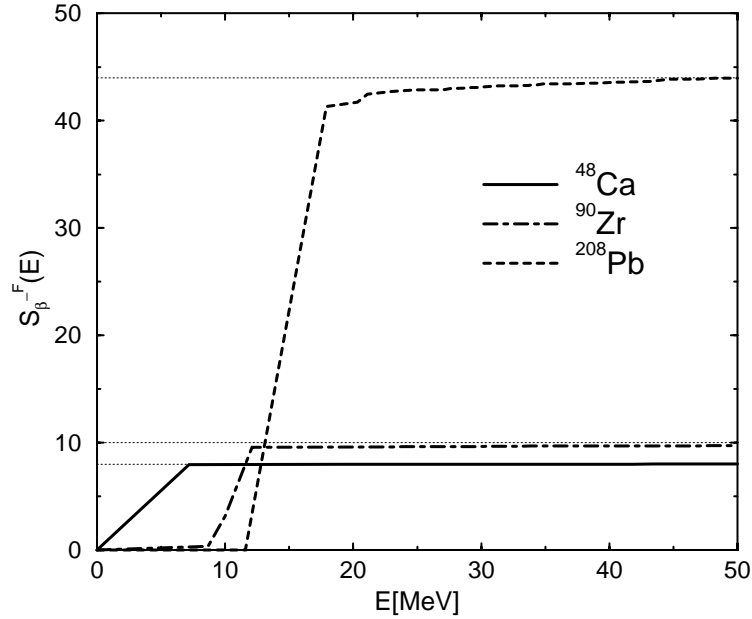


Figure 5.2: The IAR running sum (5.21) for ⁴⁸Ca, ⁹⁰Zr and ²⁰⁸Pb. The values corresponding to the model-independent sum rules for β -transitions of a Fermi type, $S_{\beta^-}(F) = N - Z$, are displayed by the horizontal dotted lines.

lines) appear to be very accurately fulfilled. As it is shown in Table 5.1, this property is somewhat more precisely achieved in our model than in other microscopic calculations. In conclusion, we note that the present model reproduces the simplest charge exchange mode (IAR) reasonably, in a good agreement with other theoretical studies.

5.3 Gamow-Teller resonance

We next employ the pn-RRPA model to describe $J^\pi = 1^+$ collective GT mode, composed from the isospin-flip (T=1) plus spin-flip (S=1) transitions. The Gamow-Teller β^\pm transition is generated by the weak interaction mediated via a spin-isospin operator,

$$Q_{\beta^\pm}^{GT} = \sum_{i=1}^A \Sigma \tau_\pm \quad (5.22)$$

where the spin-dependent part is built from the Pauli matrices,

$$\Sigma = \begin{pmatrix} \boldsymbol{\sigma} & \mathbf{0} \\ \mathbf{0} & \boldsymbol{\sigma} \end{pmatrix}. \quad (5.23)$$

In the relativistic description of Gamow-Teller excitations, only operators connecting large components of Dirac spinors (e.g. $\Sigma \tau_\pm$ -operator) have a significant contribution to the transition probabilities. In the non-relativistic limit, this leads to the usual GT operator $\sigma \tau_\pm$. Other terms involving odd operators (e.g. α -matrix) which connect the small components with the large ones, have a small overall transition strength that vanishes for the non-relativistic nucleon velocities.

The pn-RRPA residual interaction for the charge-exchange 1^+ excitations is built on the one boson exchange of the isovector vector $\vec{\rho}$ -meson and $\vec{\pi}$ -meson with the pseudovector coupling to the nucleon. However, the derivative type of pion-nucleon coupling contains a zero-range term that is expected to be suppressed by the short-range correlations. Since in reality nucleon and meson have finite sizes, the contact force would be suppressed by the correlations due to the repulsion of the nucleon-nucleon potential at short distances. [66]. In order to remove these spurious components of the contact term, the two-body matrix elements of the δ -force

$$V(1, 2) = g'_0 \left(\frac{f_\pi}{m_\pi} \right)^2 \vec{\tau}_1 \cdot \vec{\tau}_2 \boldsymbol{\sigma}_1 \cdot \boldsymbol{\sigma}_2 \delta(r_1 - r_2) \quad (5.24)$$

with an adjustable strength g'_0 are explicitly subtracted. This term corresponds to the zero-range Landau-Migdal force from the non-relativistic (ρ, π) -exchange models [177]. From the theoretical point of view, the zero-range interaction from the pseudovector π -exchange should be completely eliminated with $g'_0=1/3$. However, in both the non-relativistic [177] and relativistic calculations [66, 185], a purely phenomenological value $g'_0=0.7$ has been used in order to obtain agreement with the measured energies of collective unnatural parity excitations.

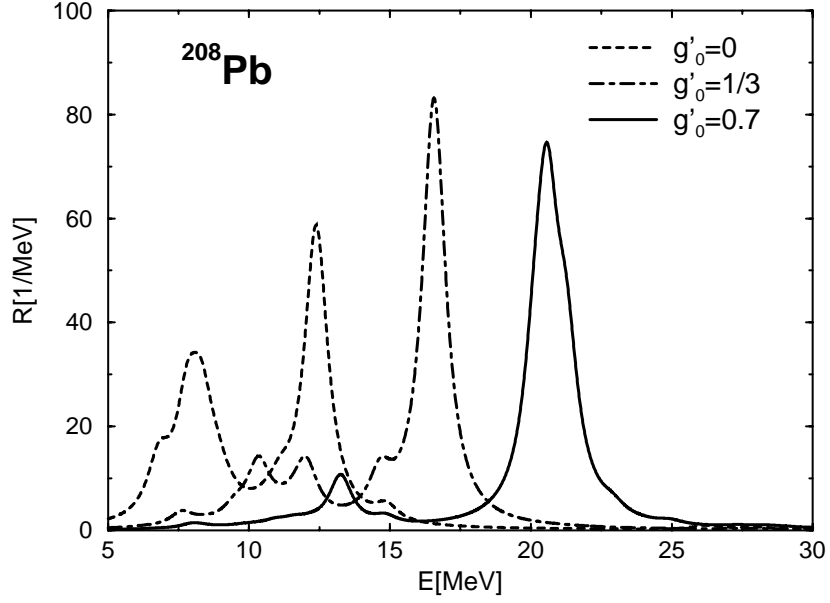


Figure 5.3: The pn-RRPA Gamow-Teller strength distribution with respect to the parent nucleus ^{208}Pb , evaluated with NL3 effective interaction. Different values for the strength parameter of the contact term are used, i.e. $g'_0 = 0, 1/3$ and 0.7 .

		RRPA (NL3)	RRPA [66]	RPA (SIII) [172]	RPA (SIII) [174]	EXP.
^{208}Pb	$E[\text{MeV}]$	20.31	18.9	21.11	18.8	19.2 ± 0.2
	$\sum S(E)[\%]$	99.8	80*	61*	63.6*	60-70
^{90}Zr	$E[\text{MeV}]$	16.3	16.0			15.6 ± 0.3
	$\sum S(E)[\%]$	100.0	80*			28
^{48}Ca	$E[\text{MeV}]$	11.06	11.0			≈ 10.5
	$\sum S(E)[\%]$	99.9	82*			35

Table 5.2: The same like in Table 5.1, but for the Gamow-Teller 1^+ excitations. The summed Gamow-Teller strength is evaluated with respect to the model independent sum rule $3(N-Z)$. pn-RRPA results are compared with experimental data for ^{48}Ca [181], ^{90}Zr [182, 164], and ^{208}Pb [184, 183, 186].

* Here $\sum S(E)$ corresponds only to the nearby region of the Gamow-Teller peak.

In Fig. 5.3 we display the pn-RRPA response to the Gamow-Teller operator (5.22) for ^{208}Pb . The transition strength function $R(E)$ is plotted for three different cases with respect to the strength of contact term: (i) $g'_0=0$, (ii) $g'_0=1/3$, and (iii) $g'_0=0.7$. The first case (i) results in an unrealistic strength distribution, located mainly in two pronounced low-lying peaks far below the experimental value of GTR excitation energy 19.2 ± 0.2 MeV with respect to the target nuclei. When we remove the delta-function contribution with $g'_0=1/3$, although the main GT peak is shifted to ≈ 17 MeV, it is still located below the measured value. Only after we employ a phenomenological value $g'_0=0.7$, is the GT energetics properly recovered. This result is in agreement with the relativistic RPA calculations in Ref. [66]. In another investigation [67], the phenomenological Landau-Migdal force has been substituted by a microscopic nucleon-nucleon interaction, generated from the rho-nucleon tensor coupling. However, this coupling appeared to have a very small effect on the GT excitations, only redistributing the strength in the low energy region between 5 and 15 MeV. On the other hand, when the short-range correlations are simulated by the simple extraction of the contact term, the overall effect turned out to be too large, i.e. $g'_0=0.7$ is replaced by a significantly larger value $g'_{0(\pi+\rho)}=1.6$ in (5.24), resulting in an overestimated GTR energy.

In Table 5.2 we list the GTR excitation energies and the amount of exhausted strength with respect to the Ikeda sum rule in ^{48}Ca , ^{90}Zr and ^{208}Pb as target nuclei for the charge-exchange (p, n) scattering. We compare the pn-RRPA results with another non-relativistic [172, 174] and relativistic studies [66], as well as with the experimental values for ^{48}Ca [181], ^{90}Zr [182, 164], and ^{208}Pb [184, 183, 186]. We note that the GTR excitations are well reproduced with the NL3 effective interaction by using a fixed phenomenological constant $g'_0=0.7$. In addition, the model independent Ikeda sum rule is very precisely fulfilled, in contrast to a selection of experimental studies. In the next section, we investigate in more detail the issue of sum rules in relativistic models.

The asymmetry between the neutron and proton number in the parent nuclei is closely related to the difference among GT^+ and GT^- strength distributions. In particular, as one moves away from the valley of β -stability towards the neutron drip-line, the β^- strength from (p, n) reactions dominates over the β^+ strength measured in (n, p) scattering.

5.4 Effects of the Dirac Sea in the Gamow-Teller sum-rule

The problem of GTR strength quenching has been addressed in many theoretical and experimental studies over the last two decades. By using the properties of isospin raising and lowering operators, the total sum of the Gamow-Teller strength can be expressed by the well known Ikeda sum rule [158, 157],

$$\left(S_{\beta^-}^{GT} - S_{\beta^+}^{GT} \right) = 3(N - Z), \quad (5.25)$$

where $S_{\beta^\pm}^{GT}$ corresponds to the total sum of Gamow-Teller strength for the β^\pm transitions, i. e. to the m_0 moment. N and Z are numbers of neutrons and protons in the parent

nucleus. Even though the summed strength $S_{\beta^\pm}^{GT}$ directly depends on the nuclear structure of the parent ground state, the difference between the strengths for β^+ and β^- types of excitation is only determined by a difference in the nucleon numbers, and not on the way in which the protons and neutrons are actually bound in the ground state. In this sense, the sum rule (5.25) is completely model independent, and it can be employed to test the completeness of the single particle basis used, as well as to check whether the measured strength function is complete [187]. Since both $S_{\beta^\pm}^{GT}$ are positive definite quantities, the sum rule (5.25) specifies a minimum strength $S_{\beta^-}^{GT}$ that is expected from (p, n) scattering experiments, i.e.

$$S_{\beta^-}^{GT} \geq 3(N - Z). \quad (5.26)$$

As a consequence of the Pauli blocking effect, usually $S_{\beta^-}^{GT} \gg S_{\beta^+}^{GT}$, leading to an approximate Gamow-Teller sum rule $S_{\beta^-}^{GT} \approx 3(N - Z)$. However, in the first systematic (p, n) experiment, GT strength exhausted only a fraction of 1/2 to 2/3 of this value [188]. Since then, the missing strength has been searched for in various models, ranging from those with more complex configurations of normal nucleons, to those including other baryon degrees of freedom in addition to the protons and neutrons. In a recent investigation, the problem of GT strength quenching, appeared to be solved in the $^{90}\text{Zr}(p, n)^{90}\text{Nb}$ reaction, where the sum of GT strength also included a higher energy region beyond the GT peak ($E \leq 50$ MeV), resulting in $90 \pm 5\%$ of the Ikeda sum rule [164]. This is in agreement with theoretical studies where the GT strength distribution became somewhat pushed toward the region beyond the main resonance peak, due to the coupling between the one phonon (ph) and two-phonon states ($2p - 2h$) [161, 189]. A more popular approach suggested that in addition to the usual ph configurations, excitations of the nucleons to the Δ -state could contribute to the shift of GT strength toward the Δ -excitation region. In that case, the high energy GT strength nearby ~ 300 MeV has been suggested as the origin of the missing strength [163]. However, a measurement from Ref. [164] implied that the contributions to GTR sum-rule due to $\Delta - h$ configurations are, in fact, less than 10% [164].

In the first relativistic RPA study of charge-exchange resonances, the summed GT strength exhausted only $\approx 93\%$ of the Ikeda sum rule [66]. This quenching has been justified by the absence of $2p - 2h$ and $\Delta - h$ excitations in the model. However, as has been shown, the contributions from the Δ degrees of freedom are relatively small, and when going from the usual ph RPA to the second random phase approximation (SRPA) including the interaction between both ph and $2p - 2h$ states [190], the difference of the non-energy weighted sum rules is conserved,

$$\left(S_{\beta^-}^{GT} - S_{\beta^+}^{GT} \right)_{RPA} = \left(S_{\beta^-}^{GT} - S_{\beta^+}^{GT} \right)_{SRPA}. \quad (5.27)$$

The main effect from $2p - 2h$ configurations is only the redistribution of the GT strength toward higher energies. It means that the RRPA sum rule quenching from Ref. [66] must have some other origin. We will show that an additional contribution to the total GT strength must be considered coming from the αh configurations, including transitions to the negative energy states in the Dirac sea (α), which have not been accounted for

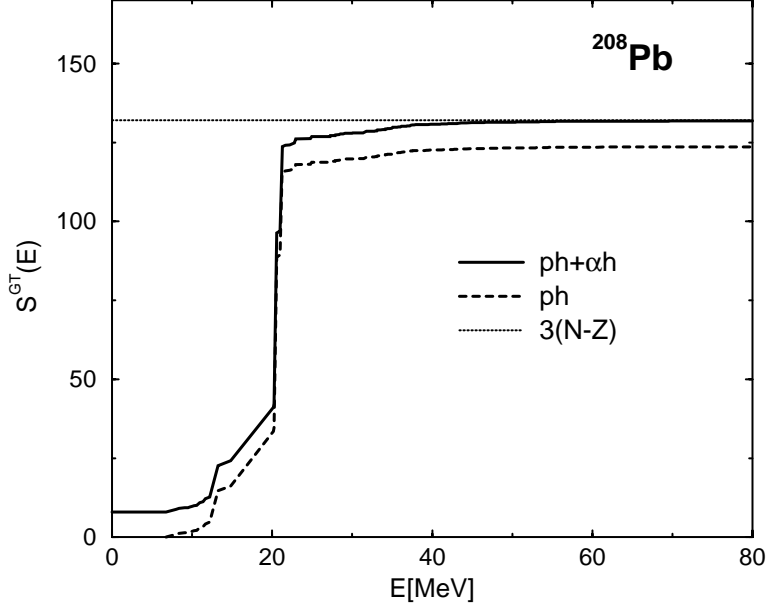


Figure 5.4: The running sum of GTR strength distribution for ^{208}Pb . The solid line corresponds to the full pn-RRPA calculation that includes both the ph and αh configurations. The case without configurations involving the negative-energy states from the Dirac sea is shown by the dashed line. The total sum of GT strength is compared to the model independent Ikeda sum rule (dotted line).

in previous RRPA investigations [66, 67]. These configurations play an important role in achieving a proper description of ISGMR excitation energies. In Chapter 2 we have also shown that the total energy-weighted sum rule of IVGDR is significantly reduced if the antiparticle degrees of freedom are neglected. Since the sum rules depend on the completeness of a selected single-particle basis, the antiparticle states have an important contribution in the relativistic models. Recently, it has been shown that $\approx 12\%$ of the Ikeda sum rule is taken by nucleon-antinucleon states with high excitation energy [68]. In the present pn-RQRPA model, the sum rule (5.25) is only very accurately fulfilled for the full space including both ph and αh configurations (see Table 5.2). This property is exemplified in Fig 5.4, where we plot the GT running sum,

$$S^{GT}(E) = \sum_{E_v < E} B_{\beta^-}^{GT}(E_v) - \sum_{E_\pi < E} B_{\beta^+}^{GT}(E_\pi), \quad (5.28)$$

in order to investigate the completeness of the pn-RRPA configuration space. If only the usual ph single-phonon space is employed, the GT running sum is systematically below the value $3(N-Z)$ of the model independent Ikeda sum rule. After we expand the ph configuration space with an additional set of configurations, which include the antiparticle degrees of freedom, the missing $\approx 10\%$ of the expected total strength is exactly recovered.

To illustrate how the excitations to the Dirac sea actually contribute to the strength

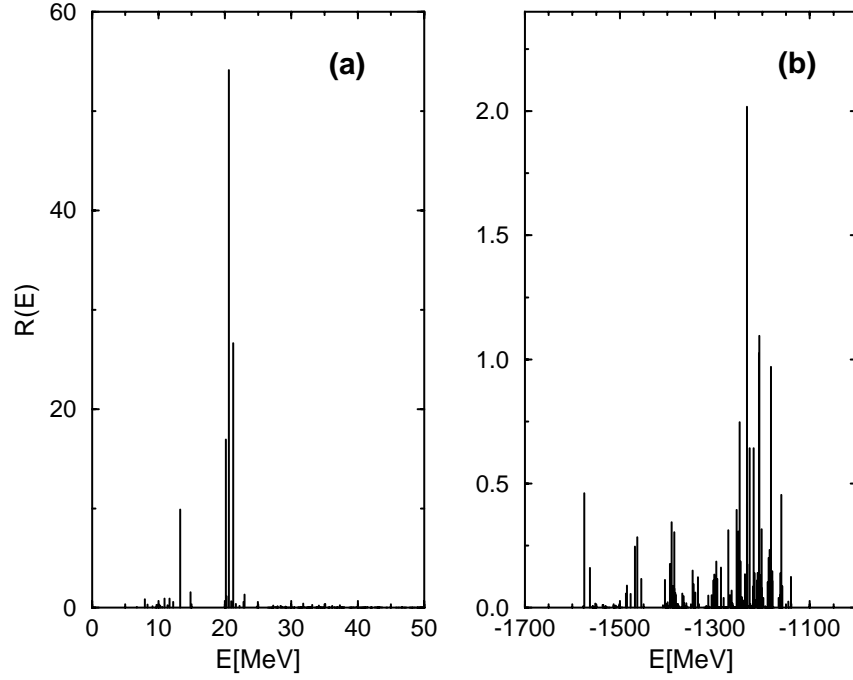


Figure 5.5: The strength distribution of discrete GT^- states from (a) particle and (b) antiparticle degrees of freedom included in the pn-RRPA configuration space (with NL3 parameterization, $g_\delta=0.7$).

distribution, in Fig. 5.5 we plot the discrete GT^- pn-RRPA response in ^{208}Pb . Two regions of excitation energies are displayed: (a) the usual $\pi p - \nu h$ based medium-energy strength with a pronounced Gamow-Teller peak at 20.31 MeV, and (b) the spectrum built from $\pi\alpha - \nu h$ transitions. Even though the strength of the peaks due to configurations involving the Dirac sea of negative-energy states are relatively small with respect to the major GTR peak, their overall sum contributes to make up for the missing strength.

Conclusion

In the present investigation, we have formulated the relativistic quasiparticle random phase approximation (RQRPA) in the canonical single-nucleon basis of the relativistic Hartree-Bogoliubov (RHB) model. The RHB model presents the relativistic extension of the Hartree-Fock-Bogoliubov framework, and it provides a unified description of mean-field and pairing correlations [37]. In the RHB framework the ground state of a nucleus can be written either in the quasiparticle basis as a product of independent quasi-particle states, or in the canonical basis as a highly correlated BCS-state. By definition, the canonical basis diagonalizes the density matrix and it is always localized [7]. It describes both the bound states and the positive-energy single-particle continuum. The RHB+RQRPA model employed in this work is fully self-consistent. For the interaction in the particle-hole channel effective Lagrangians with nonlinear meson self-interactions are used, and pairing correlations are described by the pairing part of the finite range Gogny interaction. Both in the ph and pp channels, the same interactions are used in the RHB equations that determine the canonical quasiparticle basis, and in the matrix equations of the RQRPA. This is very important, because the energy weighted sum rules are only satisfied if the pairing interaction is consistently included both in the static RHB and in the dynamical RQRPA calculations. On the other side, the self-consistency is essential to ensure that the RQRPA strength distributions are free of the spurious components associated with the center-of-mass motion or with mixing of the nucleon number in the RHB ground state.

The two-quasiparticle configuration space includes states with both nucleons in the discrete bound levels, states with one nucleon in the bound levels and one nucleon in the continuum, and also states with both nucleons in the continuum. The RQRPA configuration space includes the Dirac sea of negative energy states. In addition to the configurations built from two-quasiparticle states of positive energy, the RQRPA configuration space contains pair-configurations formed from the fully or partially occupied states of positive energy and the empty negative-energy states from the Dirac sea. The inclusion of configurations built from occupied positive-energy states and empty negative-energy states is also essential for the decoupling of spurious states.

In the present work, we apply the RHB+RQRPA model to investigate unique excitation phenomena exhibited by nuclei with a large neutron excess. In particular we study the possible occurrence of collective isovector modes in the energy region below the giant resonances, i.e. the pygmy resonance. This mode could provide important information on the isospin and density dependence of the effective nuclear interaction. For example, the pygmy dipole resonance can be directly related to the neutron excess, and therefore the splitting between the GDR and the pygmy resonance represents a measure of the neutron

skin. Precise information on neutron skin in heavy nuclei is essential for the quantification of the isovector channel of effective nuclear forces.

We have analyzed the low-lying multipole strength distributions, the transition densities, the neutron and proton ph excitations which determine the structure of the transition amplitudes, the transition currents and velocity distributions of loosely bound neutrons and core densities. We have also studied the evolution of collectivity in the low-energy isovector dipole response throughout the nuclide chart.

The RHB+RQRPA approach is used to study the multipole excitations of neutron rich oxygen isotopes. In particular, we investigated isoscalar monopole, isovector dipole and isoscalar quadrupole excitations of ^{22}O . The NL3 parameterization has been used for the RMF effective Lagrangian [80], and the Gogny D1S finite range interaction has been employed in the pp channel [84]. In the present numerical implementation the RHB eigenvalue equations, the Klein-Gordon equations for the meson fields, and the RQRPA matrix equations are solved by expanding the nucleon spinors and the meson fields in a basis of eigenfunctions of a spherical harmonic oscillator. The calculations have illustrated the importance of a consistent treatment of pairing correlations in the RHB+RQRPA framework. The results have been compared with calculations performed in the non-relativistic continuum QRPA based on the coordinate state representation of the HFB framework [38]. It has been shown that the RHB+RQRPA results are in agreement with recent experimental data [21, 96, 22] and with non-relativistic model calculations of the multipole response of neutron rich oxygen isotopes [35, 100, 102, 40, 103].

The dipole response in nuclei with large neutron to proton ratio is characterized by the fragmentation of the strength distribution and its spreading into the low-energy region, and by the mixing of isoscalar and isovector modes. In light nuclei the onset of dipole strength in the low-energy region is due to non-resonant excitations of the loosely bound neutrons. In heavier nuclei, low-lying dipole states appear which are characterized by a more distributed structure of the RRPA amplitude, exhausting approximately 2% of the EWSR. Among several peaks characterized by single particle transitions, a single collective isovector dipole state is identified below 10 MeV. A coherent superposition of many neutron particle-hole configurations characterizes its RRPA amplitude. An analysis of the corresponding transition densities and velocity distributions reveals the dynamics of the dipole pygmy resonance: the vibration of the excess neutrons against the inert core composed of equal numbers of protons and neutrons.

The RHB+RQRPA has also been employed in the analysis of the evolution of the low-lying isovector dipole strength in Ca, Ni, and Sn isotopes and $N=82$ isotones. The analysis is motivated by very recent data on the concentration of electric dipole strength below the neutron separation energy in $N = 82$ semi-magic nuclei [121]. It has been shown that in neutron rich nuclei a relatively strong peak appears in the dipole response below 10 MeV, with a QRPA amplitude characterized by a coherent superposition of many neutron two-quasiparticle configurations. The dynamics of this state corresponds to that of a pygmy dipole resonance: the oscillation of the skin of excess neutrons against the core composed of an equal number of protons and neutrons. It should be emphasized that, even though the IV GDR excitation energies calculated with the NL3 effective interaction are in excellent agreement with experimental data on Sn isotopes, the pygmy peaks in

the low-energy region do not compare too well with the data on low-lying dipole strength in $N = 82$ isotones. The calculated peaks are ≈ 2 MeV higher than the experimental weighted mean energies. This might indicate that there are problems with the isovector channel of the effective interaction. Namely, if the pygmy resonance is directly related to the thickness of the neutron skin, the splitting between the excitation energies of the pygmy state and the IV GDR should be determined by the isovector channel of the effective force.

In addition, we have investigated possible existence of a skin oscillation mode in the stable neutron-rich nuclei. In the case of closed shell nuclei, the RHB+RQRPA approach limits to Dirac-Hartree+relativistic random phase approximation (RRPA) model. We used a fully self-consistent RRPA to analyze the isovector dipole strength distribution in ^{208}Pb . In particular, we have investigated the relationship between the neutron particle-hole excitations at low energy and the onset of dipole pygmy resonances. In the case of ^{208}Pb , RRPA calculations reproduce the excitation energy of the isovector giant dipole resonance. In addition, the low-lying E1 peaks are calculated in the energy region between 7 and 11 MeV. While some of these represent the fine structure of the giant resonance, a collective state has been identified whose dynamics correspond to that of a dipole pygmy resonance. By analyzing transition densities and velocity distributions, we have related the onset of pygmy resonance at 7.29 MeV to the vibration of the excess neutrons against the inert core composed of protons and neutrons in the same shell model orbitals. This result is in excellent agreement with the very recent NRF experimental data [26].

The RHB+RQRPA model has also been applied to study the compression modes in a series of nuclei, from ^{90}Zr , toward Sn and Sm isotopes, up to ^{208}Pb . The isoscalar giant monopole resonances are the best reproduced by using the effective interaction NL3, associated with the nuclear matter incompressibility $K_{nm}=271.8$ MeV. Very good agreement in ISGMR energies is achieved in particular with the recent (α, α') scattering experiment [138] with somewhat higher excitation energies than the previous investigations [139, 140]. More exotic compression mode, the isoscalar giant dipole resonance, similar as other nonrelativistic calculations, in the present model results with a giant resonance state several MeV higher than the experimental prediction. In addition to the compression dipole mode above 20 MeV, significant dipole strength is obtained in the low lying region. This structure of the E1 strength distribution is very similar to other nonrelativistic calculations [64]. Recent experiments also predict some strength in the low-lying region. To get a better understanding of this puzzling structure of isoscalar dipole strength distribution, we relate this problem with isoscalar toroidal dipole strength distributions in spherical nuclei, calculated in the framework of a fully self-consistent relativistic random phase approximation. Whereas the ISGDR is mainly the "squeezing" mode characterized by the volume oscillations, the dynamics of the toroidal dipole mode is dominated by vortex collective motion corresponding to a transverse wave. According to our investigation, we suggest that the recently measured "low-lying component of the isoscalar dipole mode" might correspond to the toroidal giant dipole resonance. Although predicted by several theoretical models, the existence of toroidal resonances has not yet been confirmed in experiment. Recently, it has been suggested that the transversal E1 excitations could be investigated in the electron scattering with small momentum transfer

at S-DALINAC(GSI) [121]. The strong mixing between the toroidal resonance and the dipole compression mode might help to explain the large discrepancy between theory and experiment on the position of isoscalar giant dipole resonances.

Finally, we have extended the present model to the proton-neutron RQRPA formulated in RHB canonical basis, for studies of the charge-exchange excitations in atomic nuclei. The residual interaction is based on the relativistic one-boson exchange interaction composed from the isovector vector ρ -field plus an isovector pion field with pseudovector coupling. This type of interaction necessitates a special treatment of the contact term, by including an equivalent of the non-relativistic zero-range Landau-Migdal force, with a phenomenological strength parameter. The pn-RQRPA excitation energies of isobaric analog and Gamow-Teller resonances appeared to be in a good agreement with other theoretical and experimental studies. In addition, we have extended the pn-RQRPA configuration space to include the antinucleon degrees of freedom, which have been usually neglected in previous investigations. We have shown that $2qp$ configurations that involve transitions to the negative-energy Dirac sea, actually play an important role to fulfill the model independent sum rules for the Gamow-Teller resonance. In future investigations, the present pn-RQRPA model will be further extended in studies related to the fundamental nucleosynthesis processes in particular the electron capture and nuclear β -decay.

In conclusion, the relativistic QRPA formulated in the canonical basis of the RHB model represents a significant contribution to the theoretical tools that can be employed in the description of exotic multipole response, not only in stable nuclei, but also in weakly bound nuclei away from the valley of β -stability.

Appendix A

Relativistic Two-body Matrix Elements in the RQRPA Residual Interaction

The ph part of RQRPA residual interaction is based on the relativistic one-boson-exchange interaction. In the case of equal particle RQRPA, σ , ω^μ , $\vec{\rho}^\mu$ and photon field A^μ are taken into account, whereas in pn-RQRPA only the isovector ρ -meson and pion with pseudovector coupling actually contribute to RPA matrices. Here we give only a short preview of basic formulae, more elaborate outline is available in Ref. [17]. A general form of the two-body matrix elements in RQRPA ph residual interaction is given by

$$\langle 12|V_\chi|34\rangle = \int d\mathbf{r}_1 d\mathbf{r}_2 \bar{\psi}_1(\mathbf{r}_1) \bar{\psi}_2(\mathbf{r}_2) V_\chi(|\mathbf{r}_1 - \mathbf{r}_2|) \psi_3(\mathbf{r}_1) \psi_4(\mathbf{r}_2), \quad (\text{A.1})$$

where χ corresponds to the fields ($\sigma, \omega, \rho, \gamma, \pi$), while the Dirac spinor $\psi_i(\mathbf{r})$ for spherical symmetry is defined in (1.84). The matrix elements are coupled to a good angular momentum in the following way:

$$\begin{aligned} \langle 1 2|V_\chi|3 4\rangle^J &= \sum_{m_1, m_3} \sum_{m_4, m_2} (-)^{j_3 - m_3} \langle j_1 m_1, j_3 - m_3 | JM \rangle (-)^{j_2 - m_2} \langle j_4 m_4, j_2 - m_2 | JM \rangle \\ &\cdot \langle j_1 m_1 j_2 m_2 | V_\chi | j_3 m_3 j_4 m_4 \rangle. \end{aligned} \quad (\text{A.2})$$

By using the representation of propagator in the momentum space, for the spin-independent vertices Γ , the matrix elements simplify into,

$$\begin{aligned} \langle 1 2|V_\chi|3 4\rangle^J &= \frac{(4\pi g_\chi)^2}{2J+1} (-)^{j_2 - j_4} \int \frac{q^2 dq}{(2\pi)^3} \\ &\cdot \langle 1 ||\Gamma_\chi j_J(qr) Y_J || 3 \rangle D_\chi(q) \langle 2 ||\Gamma_\chi j_J(qr) Y_J || 4 \rangle, \end{aligned} \quad (\text{A.3})$$

while for the spin-dependent vertices we get,

$$\langle 1 2|V_\chi|3 4\rangle^J = \sum_L \frac{(4\pi g_\chi)^2}{2J+1} (-)^{j_2 + j_4 + L + J} \int \frac{q^2 dq}{(2\pi)^3} \quad (\text{A.4})$$

$$\cdot \langle 1 ||j_L(qr) [\vec{\gamma} Y_L]_J || 3 \rangle D_\chi(q) \langle 2 ||j_L(qr) [\vec{\gamma} Y_L]_J || 4 \rangle, \quad (\text{A.5})$$

where $j_L(qr)$ is the spherical Bessel function. The propagators in the coordinate space have a Yukawa form dependent only on the relative coordinate, whereas in the momentum space they reduce to,

$$D_\chi(q) = \frac{1}{q^2 + m_\chi^2}. \quad (\text{A.6})$$

Explicitely, for the isoscalar σ -meson and time-like part of ω -meson,

$$\begin{aligned} \langle 1 \ 2 | V_\sigma | 3 \ 4 \rangle^J &= \frac{(4\pi g_\sigma)^2}{2J+1} (-)^{j_2-j_4} \langle j_1 || Y_J || j_3 \rangle \langle j_2 || Y_J || j_4 \rangle \\ &\cdot \int \frac{q^2 dq}{(2\pi)^3} \langle 1 \ | \ \gamma_0 j_J(qr) | 3 \ \rangle D_\sigma(q) \langle 2 \ | \ \gamma_0 j_J(qr) | 4 \ \rangle \end{aligned} \quad (\text{A.7})$$

$$\begin{aligned} \langle 1 \ 2 | V_\omega | 3 \ 4 \rangle^J &= \frac{(4\pi g_\omega)^2}{2J+1} (-)^{j_2-j_4} \langle j_1 || Y_J || j_3 \rangle \langle j_2 || Y_J || j_4 \rangle \\ &\cdot \int \frac{q^2 dq}{(2\pi)^3} \langle 1 \ | \ j_J(qr) | 3 \ \rangle D_\omega(q) \langle 2 \ | \ j_J(qr) | 4 \ \rangle \end{aligned} \quad (\text{A.8})$$

where the radial matrix elements are defined as,

$$\langle 1 | \gamma_0 j_J(qr) | 3 \rangle = \int r^2 dr j_J(qr) (f_1^*(r) f_3(r) - g_1^*(r) g_3(r)) \quad (\text{A.9})$$

$$\langle 1 | j_J(qr) | 3 \rangle = \int r^2 dr j_J(qr) (f_1^*(r) f_3(r) + g_1^*(r) g_3(r)). \quad (\text{A.10})$$

On the other side, for the spatial part of ω - and ρ -mesons, the vertex $\Gamma = \boldsymbol{\alpha}$, and for the reduced matrix elements in (A.4) we have,

$$\begin{aligned} \langle 1 \ || j_L(qr) [\boldsymbol{\alpha} Y_L]_J || 3 \ \rangle &= - \left\{ \langle l_1 j_1 || [\vec{\sigma} Y_L]_J || \tilde{l}_3 j_3 \rangle i \int r^2 dr j_L(qr) f_1^*(r) g_3(r) \right. \\ &\quad \left. - \langle \tilde{l}_1 j_1 || [\vec{\sigma} Y_L]_J || l_3 j_3 \rangle i \int r^2 dr j_L(qr) g_1^*(r) f_3(r) \right\}. \end{aligned} \quad (\text{A.11})$$

For the π -meson with pseudovector coupling, the two-body matrix element is given by [17],

$$\begin{aligned} \langle 1 \ 2 | V_\pi^{(pv)} | 3 \ 4 \rangle^J &= (4\pi \frac{f_\pi}{m_\pi})^2 \frac{(-)^{j_2-j_4}}{(2J+1)^2} \int \frac{q^4 dq}{(2\pi)^3} \\ &\cdot ((J+1) \langle n_1 j_1 || j_{J+1}(qr) [\Sigma Y_{J+1}]_J || n_3 j_3 \rangle D_\pi(q) \langle n_2 j_2 || j_{J+1}(qr) [\Sigma Y_{J+1}]_J || n_4 j_4 \rangle \\ &+ \sqrt{J(J+1)} \langle n_1 j_1 || j_{J+1}(qr) [\Sigma Y_{J+1}]_J || n_3 j_3 \rangle D_\pi(q) \langle n_2 j_2 || j_{J-1}(qr) [\Sigma Y_{J-1}]_J || n_4 j_4 \rangle \\ &+ \sqrt{J(J+1)} \langle n_1 j_1 || j_{J-1}(qr) [\Sigma Y_{J-1}]_J || n_3 j_3 \rangle D_\pi(q) \langle n_2 j_2 || j_{J+1}(qr) [\Sigma Y_{J+1}]_J || n_4 j_4 \rangle \\ &+ J \langle n_1 j_1 || j_{J-1}(qr) [\Sigma Y_{J-1}]_J || n_3 j_3 \rangle D_\pi(q) \langle n_2 j_2 || j_{J-1}(qr) [\Sigma Y_{J-1}]_J || n_4 j_4 \rangle \end{aligned} \quad (\text{A.12})$$

with Σ defined in (5.23), while the reduced matrix elements read,

$$\begin{aligned} \langle n_1 j_1 || j_{J+1}(qr) [\Sigma Y_{J+1}]_J || n_3 j_3 \rangle &= \langle l_1 j_1 || [\sigma Y_{J+1}]_J || l_3 j_3 \rangle \int r^2 dr j_{J+1}(qr) f_{n_1}^*(r) f_{n_3}(r) \\ &+ \langle \tilde{l}_1 j_1 || [\sigma Y_{J+1}]_J || \tilde{l}_3 j_3 \rangle \int r^2 dr j_{J+1}(qr) g_{n_1}^*(r) g_{n_3}(r) \end{aligned} \quad (\text{A.13})$$

whereas the propagator is given by,

$$D_\pi^{(pv)}(q) = -\frac{1}{q^2 + m_\pi^2}. \quad (\text{A.14})$$

The matrix elements for the pion exchange interaction with the pseudovector coupling (A.12) contain an unrealistic contact term in the central spin-dependent channel of the force. Therefore we have to subtract the contribution of delta-interaction from the matrix elements for pions. The propagator for contact interaction is a constant in the momentum space,

$$D_{\delta_\pi}(q) = \frac{1}{3} \quad (\text{A.15})$$

resulting with the following two body matrix element:

$$\begin{aligned} \langle 1 \ 2 | V_{\delta_\pi}^{(pv)} | 3 \ 4 \rangle^J &= -\frac{1}{3} \left(\frac{f_\pi}{m_\pi} \right)^2 \frac{1}{2J+1} (-1)^{j_2+j_4+J} \sum_L (-1)^L \\ &(\langle l_1 j_1 || [\sigma Y_L]_J || l_3 j_3 \rangle \langle l_2 j_2 || [\sigma Y_L]_J || l_4 j_4 \rangle \int r^2 dr f_{n_1}^*(r) f_{n_2}^*(r) f_{n_3}(r) f_{n_4}(r) \\ &+ \langle l_1 j_1 || [\sigma Y_L]_J || l_3 j_3 \rangle \langle \tilde{l}_2 j_2 || [\sigma Y_L]_J || \tilde{l}_4 j_4 \rangle \int r^2 dr f_{n_1}^*(r) g_{n_2}^*(r) f_{n_3}(r) g_{n_4}(r) \\ &+ \langle \tilde{l}_1 j_1 || [\sigma Y_L]_J || \tilde{l}_3 j_3 \rangle \langle l_2 j_2 || [\sigma Y_L]_J || l_4 j_4 \rangle \int r^2 dr g_{n_1}^*(r) f_{n_2}^*(r) g_{n_3}(r) f_{n_4}(r) \\ &+ \langle \tilde{l}_1 j_1 || [\sigma Y_L]_J || \tilde{l}_3 j_3 \rangle \langle \tilde{l}_2 j_2 || [\sigma Y_L]_J || \tilde{l}_4 j_4 \rangle \int r^2 dr g_{n_1}^*(r) g_{n_2}^*(r) g_{n_3}(r) g_{n_4}(r)). \end{aligned} \quad (\text{A.16})$$

Appendix B

The Pairing Two-Body Matrix Elements

The pairing matrix elements in the RHB model include only $T = 1$ channel, i.e. the interaction between the same type of nucleons. To include the pairing effectively both in the ground state calculations, as well as in the RQRPA equations, we use the pairing part of the Gogny-type force (1.76) which corresponds to the sum of two Gaussians combined together with the spin and isospin exchange operators

$$P^\sigma = \frac{1}{2} (1 + \boldsymbol{\sigma}^{(1)} \boldsymbol{\sigma}^{(2)}) \quad (\text{B.1})$$

$$P^\tau = \frac{1}{2} (1 + \vec{\tau}^{(1)} \vec{\tau}^{(2)}) . \quad (\text{B.2})$$

By using the definition of total spin,

$$\mathbf{S} = \frac{1}{2} (\boldsymbol{\sigma}^{(1)} + \boldsymbol{\sigma}^{(2)}) , \quad (\text{B.3})$$

the spin operator (B.1) acting on the two-nucleon state results with

$$P^\sigma |(\frac{1}{2} \frac{1}{2}) S\rangle = (2S - 1) |(\frac{1}{2} \frac{1}{2}) S\rangle = \begin{cases} +1 & \text{for } S = 1 \\ -1 & \text{for } S = 0 \end{cases} \quad (\text{B.4})$$

In the case of $T = 1$ pairing, the expression for Gogny force (1.76) can be written in a compact form,

$$V(1, 2) = \sum_{i=1,2} V_i(|\mathbf{r}_1 - \mathbf{r}_2|) (A_i + B_i P^\sigma) \quad (\text{B.5})$$

where the radial part of the interaction reads,

$$V_i(|\mathbf{r}_1 - \mathbf{r}_2|) = e^{-\frac{(\mathbf{r}_1 - \mathbf{r}_2)^2}{\mu_i^2}} . \quad (\text{B.6})$$

In the following we expand this term can as an infinite sum of separable terms in the angular coordinates of two nucleons

$$V(|\mathbf{r}_1 - \mathbf{r}_2|) = \sum_{\lambda=0}^{\infty} V_\lambda(r_1, r_2) P_\lambda(\cos \theta_{12}) , \quad (\text{B.7})$$

where

$$P_\lambda(\cos \theta_{12}) = \frac{4\pi}{2\lambda + 1} \sum_{\mu} Y_{\lambda\mu}^*(\hat{\mathbf{r}}_1) Y_{\lambda\mu}(\hat{\mathbf{r}}_2), \quad (\text{B.8})$$

and

$$V_\lambda(r_1, r_2) = \frac{2\lambda + 1}{2} \int_{-1}^1 d \cos \theta_{12} V(|\mathbf{r}_1 - \mathbf{r}_2|) P_\lambda(\cos \theta_{12}). \quad (\text{B.9})$$

Using this expression, the two-nucleon matrix element between the non-normalized states,

$$V_{JM} = \langle rlj, r'l'j' | V(|\mathbf{r} - \mathbf{r}'|) | r\tilde{l}\tilde{j}, r'\tilde{l}'\tilde{j}' \rangle_{JM}, \quad (\text{B.10})$$

within the LS-coupling scheme, reduces to the form

$$V_{JM} = \sum_{LS} \sum_{\tilde{L}, \tilde{S}} \hat{j}\hat{j}'\hat{L}\hat{S}\hat{j}\hat{j}'\hat{L}\hat{S} \langle rr', (ll')SLJM | V(|\mathbf{r} - \mathbf{r}'|) | \tilde{r}\tilde{r}', (\tilde{l}\tilde{l}')\tilde{S}\tilde{L}JM \rangle \left\{ \begin{array}{ccc} \frac{1}{2} & \frac{1}{2} & S \\ l & l' & L \\ j & j' & J \end{array} \right\} \left\{ \begin{array}{ccc} \frac{1}{2} & \frac{1}{2} & \tilde{S} \\ \tilde{l} & \tilde{l}' & \tilde{L} \\ \tilde{j} & \tilde{j}' & J \end{array} \right\}. \quad (\text{B.11})$$

Here J , M , L and S are the total angular momentum, and its z -projection, the total orbital angular momentum and the total spin of the two-nucleon state, respectively. The usual notation for $\hat{j} = \sqrt{2j+1}$ is used. Including the expansion (B.7), the LS-coupling matrix element yields

$$V_{S\tilde{S}L\tilde{L}}^{JM} = \sum_{\lambda} \frac{4\pi}{2\lambda + 1} V_\lambda(r, r') \sum_{\mu} \langle (ll')SLJM | Y_{\lambda\mu}^*(\hat{\mathbf{r}}) Y_{\lambda\mu}(\hat{\mathbf{r}}') (A + B\hat{P}^\sigma) | (\tilde{l}\tilde{l}')\tilde{S}\tilde{L}JM \rangle, \quad (\text{B.12})$$

whereas the radial factors $V_\lambda(r, r')$ are evaluated from Eq. (B.9), and the angular part takes the form

$$\sum_{\mu} \langle (ll')SLJM | Y_{\lambda\mu}^*(\hat{\mathbf{r}}) Y_{\lambda\mu}(\hat{\mathbf{r}}') (A + B\hat{P}^\sigma) | (\tilde{l}\tilde{l}')\tilde{S}\tilde{L}JM \rangle = \delta_{S\tilde{S}} \delta_{L\tilde{L}} (A + B(2S - 1)) (-1)^{L+l+\tilde{l}} \frac{\hat{l}\hat{l}'\hat{\lambda}^2}{4\pi} \begin{pmatrix} l & \lambda & \tilde{l} \\ 0 & 0 & 0 \end{pmatrix} \begin{pmatrix} l' & \lambda & \tilde{l}' \\ 0 & 0 & 0 \end{pmatrix} \left\{ \begin{array}{ccc} \tilde{l} & \tilde{l}' & L \\ l' & l & \lambda \end{array} \right\} \quad (\text{B.13})$$

For the pairing channel in RHB model, we only consider matrix elements between two-nucleon states with total angular momentum $J = 0$, leading to

$$V_{J=0} = \delta_{jj'} \delta_{\tilde{j}\tilde{j}'} \delta_{ll'} \delta_{\tilde{l}\tilde{l}'} (2l + 1)(2\tilde{l} + 1) \hat{j}\hat{j}' \sum_{S=0,1} (-1)^{j+\tilde{j}+1+S} (2S + 1) \left\{ \begin{array}{ccc} l & l & S \\ \frac{1}{2} & \frac{1}{2} & j \end{array} \right\} \left\{ \begin{array}{ccc} \tilde{l} & \tilde{l} & S \\ \frac{1}{2} & \frac{1}{2} & \tilde{j} \end{array} \right\} \sum_{\lambda} V_\lambda(r, r') (A + B(2S - 1)) \begin{pmatrix} l & \lambda & \tilde{l} \\ 0 & 0 & 0 \end{pmatrix}^2 \left\{ \begin{array}{ccc} l & \tilde{l} & \lambda \\ \tilde{l} & l & S \end{array} \right\}. \quad (\text{B.14})$$

Appendix C

Frequently Used Abbreviations

RMFT	Relativistic Mean Field Theory
TDRMFT	Time Dependent RMFT
RRPA	Relativistic Random Phase Approximation
DFT	Density Functional Theory
HFB	Hartree Fock Bogoliubov
RHB	Relativistic Hartree-Bogoliubov
RQRPA	Relativistic Quasiparticle Random Phase Approximation
pn-RQRPA	Proton-Neutron RQRPA
NL1,NL3,NL-SH	parameterizations of the relativistic mean field
D1S	parameterization of the pairing Gogny-type interaction
EWSR	Energy Weighted Sum Rule
TRK	Thomas Reiche Kuhn sum rule
GMR	Giant Monopole Resonance
GDR	Giant Dipole Resonance
GQR	Giant Quadrupole Resonance
IV	Isovector
IS	Isoscalar
PDR	Pygmy Dipole Resonance
TGDR	Toroidal Giant Dipole Resonance
GTR	Gamow-Teller Resonance
IAR	Isobaric Analog Resonance
GSI	Gesellschaft für Schwerionenforschung (Germany)
RIA	Rare Isotope Accelerator (USA)
QPM	Quasiparticle Phonon Model
SM	Shell Model
NRF	Nuclear Resonance Fluorescence

Bibliography

- [1] J. Dobaczewski and W. Nazarewicz, *Prog. Theor. Phys. Supp.* 146, 70 (2002).
- [2] I. Tanihata, *Prog. Theor. Phys. Supp.* 146, 1 (2002).
- [3] S. A. Austin and G. F. Bertsch, *Sci. Am.*, 67, June (1995).
- [4] S. Mizutori, J. Dobaczewski, G. A. Lalazissis, W. Nazarewicz, and P. G. Reinhard, *Phys. Rev. C* 61, 044326 (2000).
- [5] H. Iwasaki et. al., *Phys. Lett. B* 491, 8 (2000).
- [6] T. Otsuka, R. Fujimoto, Y. Utsuno, R. A. Brown, M. Honma and T. Mizusaki, in *Ref. [192]*, 41 (2002).
- [7] J. Dobaczewski, W. Nazarewicz, T. R. Werner, J. F. Berger, C. R. Chinn, and J. Dechargé, *Phys. Rev. C* 53, 2809 (1996).
- [8] Yu. Ts. Oganessian et. al. *Nature* 400, 242 (1999).
- [9] V. Ninov et. al., *Phys. Rev. Lett.* 83, 1104 (1999).
- [10] A. T. Kruppa et. al. *Phys. Rev. C* 61, 034313 (2000).
- [11] G. E. Brown, T. T. S. Kuo, *Nucl. Phys. A* 92, 481 (1967).
- [12] B. D. Serot and J. D. Walecka, *Adv. Nucl. Phys.* 16, 1 (1986).
- [13] J. Boguta and A. R. Bodmer, *Nucl. Phys. A* 292, 43 (1977).
- [14] P. G. Reinhard, *Rep. Prog. Phys.* 52, 439 (1989).
- [15] T. Nikšić, D. Vretenar, and P. Ring, *Phys. Rev. C* 66, 024306 (2002).
- [16] P. Ring, *Prog. Part. Nucl. Phys.* 37, 193 (1996).
- [17] M. Serra, Ph.D. Thesis, Technische Universität München (2001).
- [18] M. Serra and P. Ring, in *Ref. [192]*, 169 (2002).
- [19] P. Ring, in *Ref. [191]*, 23 (2001).
- [20] S. Nakayama et. al., *Phys. Rev. Lett.* 85, 262 (2000).
- [21] T. Aumann et. al., *Nucl. Phys. A* 649, 297c (1999).
- [22] A. Leistenschneider et al., *Phys. Rev. Lett.* 86, 5442 (2001).
- [23] F. Bauwens et. al., *Phys. Rev. C* 62, 024302 (2000).
- [24] K. Govaert et. al., *Phys. Rev. C* 57, 2229 (1998).
- [25] R. D. Herzberg et. al., *Phys. Rev. C* 60, 051307 (1999).
- [26] N. Ryezayeva, T. Hartmann, Y. Kalmykov, H. Lenske, P. von Neumann-Cosel, V. Yu. Ponomarev, A. Richter, A. Shevchenko, S. Volz, and J. Wambach, *Phys. Rev. Lett.* 89, 272502 (2002).

- [27] F. Catara, C.H. Dasso and A. Vitturi, Nucl. Phys. A 602, 181 (1996).
- [28] F. Catara, E. G. Lanza, M. A. Nagarajan, and A. Vitturi, Nucl. Phys. A 614, 86 (1997).
- [29] I. Hamamoto, H. Sagawa and X.Z. Zhang, Phys. Rev. C 56, 3121 (1997).
- [30] Radhe Mohan, M. Danos and L.C. Biedenharn, Phys. Rev. C 3, 1740 (1971).
- [31] Y. Suzuki, K. Ikeda and H. Sato, Prog. Theor. Phys. 83, 180 (1990).
- [32] J. Chambers, E. Zaremba, J.P. Adams and B. Castel, Phys. Rev. C 50, R2671 (1994).
- [33] F. Catara, E.G. Lanza, M.A. Nagarajan and A. Vitturi, Nucl. Phys. A 624, 449 (1997).
- [34] J. P. Adams, B. Castel and H. Sagawa, Phys. Rev. C 53, 1016 (1996).
- [35] H. Sagawa and T. Suzuki, Phys. Rev. C 59, 3116 (1999).
- [36] Toshio Suzuki, H. Sagawa and P. F. Bortignon, Nucl. Phys. A 662, 282 (2000).
- [37] T. Gonzalez-Llarena, J. L. Egido, G. A. Lalazissis, and P. Ring, Phys. Lett. B 379, 13 (1996).
- [38] M. Matsuo, Prog. Theor. Phys. Supp. 146, 110 (2002).
- [39] J. Engel, M. Bender, J. Dobaczewski, W. Nazarewicz, and R. Surman, Phys. Rev. C 60, 014302 (1999).
- [40] M. Matsuo, Nucl. Phys. A 696, 371 (2001).
- [41] E. Khan, N. Sandulescu, M. Grasso, and Nguyen Van Giai, Phys. Rev. C 66, 024309 (2002).
- [42] W. Pöschl, D. Vretenar, G. A. Lalazissis and P. Ring, Phys. Rev. Lett. 79, 3841 (1997).
- [43] G. A. Lalazissis, D. Vretenar, W. Pöschl and P. Ring, Nucl. Phys. A 632, 363 (1998).
- [44] G. A. Lalazissis, D. Vretenar and P. Ring, Phys. Rev. C 57, 2294 (1998).
- [45] G. A. Lalazissis, D. Vretenar, W. Pöschl and P. Ring, Phys. Lett. B 418, 7 (1998).
- [46] D. Vretenar, G. A. Lalazissis, and P. Ring, Phys. Rev. Lett. 82, 4595 (1997).
- [47] G. A. Lalazissis, D. Vretenar and P. Ring, Nucl. Phys. A 650, 133 (1999).
- [48] G. A. Lalazissis, D. Vretenar, and P. Ring, Nucl. Phys. A 679, 481 (2001).
- [49] A. Wandelt, Ph.D. Thesis, Technische Universität München (2000).
- [50] D. Vretenar, A. Wandelt, and P. Ring, Phys. Lett. B 487, 334 (2000).
- [51] Z. Y. Ma, N. Van Giai, A. Wandelt, D. Vretenar and P. Ring, Nucl Phys A 687, 64c (2001).
- [52] Z. Y. Ma, N. Van Giai, A. Wandelt, D. Vretenar and P. Ring, Nucl. Phys. A 686, 173 (2001).
- [53] P. Ring, Z.Y. Ma, N. Van Giai, D. Vretenar, A. Wandelt and L.G. Cao, Nucl. Phys. A 694, 249 (2001).
- [54] Z. Y. Ma, A. Wandelt, N. Van Giai, D. Vretenar, P. Ring and L. G. Cao, Nucl. Phys. A 703, 222 (2002).
- [55] D. Vretenar, H. Berghammer and P. Ring, Nucl. Phys. A 581, 679 (1995).

- [56] D. Vretenar, G. A. Lalazissis, R. Behnsch, W. Pöschl and P. Ring, Nucl. Phys. A 621, 853 (1997).
- [57] D. Vretenar, N. Paar, P. Ring and G. A. Lalazissis, Phys. Rev. E 60, (1999) 308.
- [58] D. Vretenar, P. Ring, G. A. Lalazissis, and N. Paar, Nucl. Phys.A 649, 29 (1999).
- [59] J. Piekarewicz, Phys.Rev. C 64, 024307 (2001).
- [60] D. Vretenar, N. Paar, P. Ring, and G. A. Lalazissis, Phys. Rev. C 63, 047301 (2001).
- [61] D. Vretenar, N. Paar, P. Ring, and G. A. Lalazissis, Nucl. Phys. A 692, 496 (2001).
- [62] N. Paar, T. Nikšić, D. Vretenar and P. Ring, Phys. Rev. C 67, 034312 (2003).
- [63] S. Goriely and E. Khan, Nucl. Phys. A 706, 217 (2002).
- [64] G.Colò, N. Van Giai, P. F. Bortignon and M. R. Quaglia, Phys. Lett. B 485, 362 (2000).
- [65] K. Langanke, in Ref. [192], 315 (2002).
- [66] C. De Conti, A. P. Galeão and F. Krmpotić, Phys. Lett. B 444, 14 (1998).
- [67] C. De Conti, A. P. Galeão, and F. Krmpotić, Phys. Lett. B 494, 46 (2000).
- [68] H. Kurasawa, T. Suzuki and N. Van Giai, to be published (2003).
- [69] B. D. Serot, Rep. Prog. Phys. 55, 1855 (1992).
- [70] S. A. Chin and J. D. Walecka, Phys. Lett. B 52, 24 (1974).
- [71] C. J. Horowitz and B. D. Serot, Phys. Lett. B 140, 181 (1984).
- [72] D. A. Wasson, Phys. Lett. B 210, 41 (1988).
- [73] Z. Y. Zhu, H. J. Mang and P. Ring, Phys. Lett. B 254, 325 (1991).
- [74] P. Hohenberg and W. Kohn, Phys. Rev. 136 B, 864 (1964).
- [75] W. Kohn and L. J. Sham, Phys. Rev. 137 A, 1697 (1965).
- [76] K. A. Brueckner et. al. Phys. Rev. 171, 1188 (1968).
- [77] R. N. Schmid, E. Engel and R. M. Dreizler, Found. of Phys. 27, 1257 (1997).
- [78] P.G. Reinhard, M. Rufa, J. Maruhn, W. Greiner and J. Friedrich, Z. Phys. 323, 13 (1986).
- [79] M.M. Sharma, M.A. Nagarajan and P. Ring, Phys. Lett. B 312, 377 (1993).
- [80] G.A. Lalazissis, J. König, and P. Ring, Phys. Rev. C 55, 540 (1997).
- [81] H. Kucharek and P. Ring, Z. Phys. A 339, 23 (1991).
- [82] J.G. Valatin, Phys. Rev. 122, 1012 (1961).
- [83] Y.K. Gambhir, P. Ring, and A. Thimet, Ann. Phys. (N.Y.) 511, 129 (1990).
- [84] J. F. Berger, M. Girod and D. Gogny, Nucl. Phys. A 428, 25c (1984).
- [85] P. Ring and P. Schuck, The Nuclear Many-Body Problem, Springer-Verlag, New York, (1980).
- [86] M. Serra and P. Ring, Phys. Rev. C 65, 064324 (2002).
- [87] Z.Y. Ma, N. Van Giai, and H. Toki, Phys. Rev. C42, 2389 (1997).
- [88] C. Bloch and A. Messiah, Nucl. Phys. 39, 95 (1962).
- [89] F. Dawson and R. J. Furnstahl, Phys. Rev. C 42 2009 (1990).

- [90] N. Van Giai, H. Sagawa, Nucl. Phys. A 371, 1 (1981).
- [91] I. Hamamoto, H. Sagawa, and X. Z. Zhang, Phys. Rev. C 53, 765 (1996).
- [92] A. deShalit and H. Feshbach, Theoretical Nuclear Physics, Vol I: Nuclear Structure, Wiley & Sons, Toronto (1974).
- [93] C. E. Price and G. E. Walker, Phys. Lett. B 155, 17 (1985).
- [94] J. R. Shepard, E. Rost and J. A. McNeil, Phys. Rev. C 40, 2320 (1989).
- [95] J. A. McNeil, R. J. Furnstahl, E. Rost and J. R. Shepard, Phys. Rev. C 40, 399 (1989).
- [96] E. Tryggestad et al. , Nucl. Phys. A 687, 231c (2001).
- [97] E. Tryggestad et al. , Phys. Lett. B 541, 52 (2002).
- [98] J. K. Jewell et. al., Phys. Lett. B 454, 181 (1999).
- [99] E. Khan et. al., Phys. Lett. B 490, 45 (2000).
- [100] H. Sagawa and T. Suzuki, Nucl. Phys. A 687, 111c (2001).
- [101] P. G. Reinhard, Nucl. Phys. A 649, 305c (1999).
- [102] E. Khan and N. Van Giai, Phys. Lett. B 472, 253 (2000).
- [103] G. Coló and P. F. Bortignon, Nucl. Phys. A 696, 427 (2001).
- [104] M. Tohyama and A. S. Umar, Phys. Lett. B 516, 415 (2001).
- [105] D. Guillemaud-Mueller et. al., Phys. Rev. C 41, 937 (1990).
- [106] M. Fauerbach et. al., Phys. Rev. C 53, 647 (1996).
- [107] H. Sakurai et. al., Phys. Lett. B 448, 180 (1999).
- [108] O. Tarasov et. al., Phys. Lett. B 409, 64 (1997).
- [109] H. Sagawa, C. A. Bertulani, Prog. Theor. Phys. Supp. 124, 143 (1996).
- [110] J. G. Woodworth et. al., Phys. Rev. C 19, 1667 (1979).
- [111] H. Sagawa, N. Van Giai, N. Takigawa, M. Ishihara and K. Yazaki, Z. Phys. A 351, 385 (1995).
- [112] C. H. Dasso, H. M. Sofia, S. M. Lenzi, M. A. Nagarajan and A. Vitturi, Nucl. Phys. A 627, 349 (1997).
- [113] A. Ozawa, T. Kobayashi, T. Suzuki, K. Yoshida, and I. Tanihata, Phys. Rev. Lett. 84, 5493 (2000).
- [114] H. Iwasaki et. al., Phys. Lett. B 481, 7 (2000).
- [115] F. E. Bertrand, Nucl. Phys. A 354, 129c (1981).
- [116] M. Belleguic et. al., Nucl. Phys. A 682, 136c (2001).
- [117] P. G. Thirolf et. al., Phys. Lett. B 485, 16 (2000).
- [118] S. Raman et. al., Atomic Data and Nuclear Data Tables 36, 1 (1987).
- [119] T. Hartmann, J. Enders, P. Mohr, K. Vogt, S. Volz, and A. Zilges, Phys. Rev. Lett. 85, 274 (2000).
- [120] S. Ottini-Hustache, et. al., Phys. Rev. C 59, 3429 (1999).

- [121] A. Zilges, S. Volz, M. Babilon, T. Hartmann, P. Mohr, and K. Vogt, Phys. Lett. B 542, 43 (2002).
- [122] N. Pietralla et al., Phys. Rev. Lett. 88, 012502 (2002).
- [123] D. Vretenar, T. Nikšić and P. Ring, Phys. Rev. C 65, 024321 (2002).
- [124] H. L. Clark, Y.-W. Lui and D. H. Youngblood, Phys. Rev. C 63, 031301(R) (2001).
- [125] D. Vretenar, N. Paar, T. Nikšić, and P. Ring, Phys. Rev. C 65, 021301 (2002).
- [126] F. Iachello, Phys. Lett. B 160, 1 (1985).
- [127] B. L. Berman and S. C. Fultz, Rev. Mod. Phys. 47, 713 (1975).
- [128] R. D. Starr, P. Axel and L. S. Cardman, Phys. Rev. C 25, 780 (1982).
- [129] Z. W. Bell, L. S. Cardman and P. Axel, Phys. Rev. C 25, 791 (1982).
- [130] G. Kühner, D. Meuer, S. Müller, A. Richter, E. Spamer, O. Titze and W. Knüpfer, Phys. Lett. B 104, 189 (1981).
- [131] J. Ritman *et al.*, Phys. Rev. Lett. 70, 533 (1993).
- [132] H. Steinwedel and J.H.D. Jensen, Z. Naturforsch. 5a, 413 (1950).
- [133] J. Enders et. al., Phys. Lett. B 486, 279 (2000).
- [134] G Colò, N. Van Giai, P. F. Bortignon and M. R. Quaglia, in Ref. [191], 418 (2001).
- [135] J. P. Blaizot, J. F. Berger, J. Decharge and M. Girod, Nucl. Phys. A 591, 435 (1995).
- [136] N. Van Giai, P.F. Bortignon, G.Colò, Z. Y. Ma, and M. R. Quaglia, Nucl. Phys. A 687, 44c (2001).
- [137] O. Civitarese, A. G. Dumrauf, M. Reboiro, P. Ring, and M. M. Sharma, Phys. Rev. C 43, 2622 (1991).
- [138] D. Youngblood, H. L. Clark, and Y. W. Lui, Phys. Rev. Lett. 82, 691 (1999).
- [139] S. Shlomo and D. H. Youngblood, Phys. Rev. C 47, 529 (1993).
- [140] M. M. Sharma and M. N. Harakeh, Phys. Rev. C 38, 2562 (1988).
- [141] M. Farine et. al., Nucl. Phys. A 615, 135 (1997).
- [142] D. Vretenar, T. Nikšić and P. Ring, nucl-th/0302070, (2003).
- [143] M. N. Harakeh and A. E. L. Dieperink, Phys. Rev. C 63, 65 (1981).
- [144] S. Stringari, Phys. Lett. B 108, 232 (1982).
- [145] B. F. Davis et al., Phys. Rev. Lett. 79, 609 (1997).
- [146] U. Garg, Nucl. Phys. A, 649, 66c (1999).
- [147] D. Lacroix, S. Ayik, and P. Chomaz, Phys. Rev. C 63, 064305 (2001).
- [148] H. L. Clark et al., Nucl. Phys. A 649, 57c (1999).
- [149] M. Hedden, et. al., nucl-ex/0109009, (2001).
- [150] V. M. Dubovik and A. A. Cheshkov, Sov. J. Part. Nucl. 5, 318 (1975).
- [151] V. M. Dubovik and L. A. Tosunyan, Sov. J. Part. Nucl. 14(5), 504 (1983).
- [152] S. F. Semenko, Sov. J. Nucl. Phys. 34(3), 356 (1981).
- [153] E. B. Balbutsev and I.N. Mikhailov, J. Phys.G: Nucl. Phys. 14, 545 (1988).
- [154] I. Hamamoto, H. Sagawa and X.Z. Zhang, Phys. Rev. C 57, R1064 (1998).

- [155] F. E. Serr, T.S. Dumitrescu, Toru Suzuki and C. H. Dasso, Nucl. Phys. A 404, 359 (1983).
- [156] G. F. Bertsch, Suppl. Progr. Theor. Phys. 74, 115 (1983).
- [157] F. Osterfeld, Rev. Mod. Phys. 64, 491 (1992).
- [158] K. Ikeda, S. Fujii and J. I. Fujita, Phys. Lett. 3, 271 (1963).
- [159] R. R. Doering, A. Galonsky, D. M. Patterson, and G. F. Bertsch, Phys. Rev. Lett. 35, 1961 (1975).
- [160] A. Krasznahorkay et. al., Phys. Rev. Lett. 82, 3216 (1999).
- [161] G. F. Bertsch and I. Hamamoto, Phys. Rev. C 26, 1323 (1982).
- [162] W. Knüpfer, M. Dillig, and A. Richter, Phys. Lett. B 95, 349 (1980).
- [163] A. Arima, Prog. Part. Nucl. Phys. 46, 119 (2001).
- [164] T. Wakasa et. al. Phys. Rev. C 55, 2909 (1997).
- [165] L. Zhao and B. A. Brown, Phys. Rev. C 47, 2641 (1993).
- [166] E. Caurier, K. Langanke, G. Martinez-Pinedo and F. Nowacki, Nucl. Phys. A 653, 439 (1999).
- [167] P. B. Radha, D. J. Dean, S. E. Koonin, K. Langanke and P. Vogel, Phys. Rev. C 56, 3079 (1997).
- [168] J. A. Halbleib and R. A. Sorensen, Nucl. Phys. A 98, 542 (1967).
- [169] D. Cha, Phys. Rev. C 27, 2269 (1983).
- [170] M. K. Cheoun, A. Faessler, F. Simkovic, G. Teneva and A. Bobyk, Nucl. Phys. A 587, 301 (1995).
- [171] N. Van Giai and H. Sagawa, Phys. Lett. B 106, 379 (1981).
- [172] G. Colò, N. Van Giai, P. F. Bortignon and R. A. Broglia, Phys. Rev. C 50, 1496 (1994).
- [173] I. Hamamoto and H. Sagawa, Phys. Rev. C 48, R960 (1993).
- [174] T. Suzuki and H. Sagawa, Eur. Phys. J. A 9, 49 (2000).
- [175] M. Bender, P. H. Heenen and P. G. Reinhard, Rev. Mod. Phys. 75, 121 (2003).
- [176] J. Engel, P. Vogel and M. R. Zirnbauer, Phys. Rev. C 37, 731 (1988).
- [177] S. Krewald, F. Osterfeld, J. Speth, and G. E. Brown, Phys. Rev. Lett. 46, 103 (1981).
- [178] W. R. Coker and C. F. Moore, Phys. Today, p.53, April (1969).
- [179] N. Auerbach, Phys. Rep. 98, 273 (1983).
- [180] G. Colò, H. Sagawa, N. Van Giai, P. F. Bortignon and T. Suzuki, Phys. Rev. C 57, 3049 (1998).
- [181] B. D. Anderson et. al. Phys. Rev. C 31, 1161 (1985).
- [182] D. E. Bainum et. al. Phys. Rev. Lett. 44, 1751 (1980).
- [183] H. Akimune et. al., Phys. Rev. C 52, 604 (1995).
- [184] D. J. Horen et. al. Phys. Lett. B 95, 27 (1980).

- [185] P. G. Blunden and P. McCorquodale, *Phys. Rev. C* 38, 1861 (1988).
- [186] A. Krasznahorkay et. al., *Phys. Rev. C* 64, 067302 (2001).
- [187] C. D. Goodman, J. Rapaport and S. D. Bloom, *Phys. Rev. C*, 42, 1150 (1990).
- [188] C. Gaarde et. al., *Nucl. Phys. A* 334, 334 (1980).
- [189] S. Drożdż, V. Klempt, J. Speth, and J. Wambach, *Phys. Lett. B* 166, 18 (1986).
- [190] S. Adashi and E. Lipparini, *Nucl. Phys. A* 489, 445 (1988).
- [191] Nuclear structure, Proceedings of the conference Bologna 2000-structure of the nucleus at the dawn of the century, Eds. G.C. Bonsignori, M. Bruno, A. Ventura, and D. Vretenar, World Scientific, (2001)
- [192] The nuclear many-body problem 2001, Eds. W. Nazarewicz and D. Vretenar, Kluwer Academic Publishers, Netherlands, (2002).

Curriculum Vitae

Contact information:

Physik Department, Institut für Theoretische Physik - T30f
Technische Universität München, D-85748 Garching, Germany
Tel: +49-089-289-12386, Fax: +49-089-289-12296
e-mail: npaar@ph.tum.de

Home page:

<http://www.ph.tum.de/~n paar>

Date of birth:

28. December 1972, Zagreb, Croatia

Education:

1979-1987. Elementary school, Samobor, Croatia
1987-1991. Gymnasium for Mathematics and Informatics,
Zagreb, Croatia
1991. Graduated from the gymnasium with work: "Chaotic behavior
of the oscillator with external time-dependent force"
1991-1998. Undergraduate study at the University of Zagreb
1998. Dipl. Ing. of Physics, Diploma work: "Nonlinear dynamics
of collective vibrations in nuclei in the time-dependent
relativistic mean-field", supervised by
Prof. Dr. Dario Vretenar, Physics Department,
University of Zagreb
1998-1999. Military service, Croatia
2000-2003. Graduate study on the subject "Relativistic description of
the collective dynamics in exotic nuclei" under the supervision
of Prof. Dr. Peter Ring, Physik Department,
Technische Universität München, Germany

Proficiency in languages:

Croatian (native), English (fluent), German (basic)

Programming knowledge:

C, C++, Fortran, Mathematica, HTML, LaTeX

Membership:

Deutsche Physikalische Gesellschaft, Croatian physical society

List of Publications

PUBLICATIONS IN SCIENTIFIC JOURNALS:

1. V. Paar, N. Pavin, N. Paar, B. Novakovic, "Nonlinear regular dynamics of a single-degree robot model", *Robotica* 14, 423-431 (1996).
2. D. Vretenar, P. Ring, G. A. Lalazissis, and N. Paar, "Relativistic mean-field description of the dynamics of giant resonances", *Nucl. Phys.A649*, 29-36 (1999).
3. D. Vretenar, N. Paar, P. Ring, and G. A. Lalazissis, "Nonlinear dynamics of giant resonances in atomic nuclei", *Phys. Rev. E* 60, 308-319 (1999).
4. V. Paar, N. Pavin, N. Paar and B. Novakovic, "Nonlinear dynamics of a single-degree robot model; Part2: Onset of chaotic transients", *Robotica* 18, 201-208 (2000).
5. D. Vretenar, N. Paar, P. Ring and G. A. Lalazissis, "Pygmy dipole resonances in relativistic random phase approximation", *Phys. Rev. C* 63, 047301 (2001).
6. D. Vretenar, N. Paar, P. Ring and G. A. Lalazissis, "Collectivity of the low-lying dipole strength in relativistic random phase approximation", *Nucl. Phys. A*, 692 (3-4) 496-517 (2001).
7. D. Vretenar, N. Paar, P. Ring, and T. Niksic "Toroidal dipole resonances in the relativistic random phase approximation ", *Phys. Rev. C* 65, 021301 (2002).
8. G.A. Lalazissis, D. Vretenar, N. Paar, P. Ring, "Relativistic description of regular and chaotic dynamics in the giant monopole resonances", *Chaos, Solitons & Fractals*. 17, 585-590 (2003).
9. N. Paar, T. Niksic, D. Vretenar and P. Ring "Quasiparticle random phase approximation based on the relativistic Hartree-Bogoliubov model" , *Phys. Rev. C* 67, 034312 (2003).

CONFERENCE PROCEEDINGS:

10. N. Paar, D. Vretenar, P. Ring, and G. A. Lalazissis, "Nonlinear collective dynamics in atomic nuclei", *Nuclear structure, Proceedings of the conference Bologna 2000-structure of the nucleus at the dawn of the century*, Eds. G.C. Bonsignori, M. Bruno, A. Ventura, and D. Vretenar, World Scientific, 442-445 (2001).
11. D. Vretenar, G. A. Lalazissis , P. Ring, and N. Paar, "Relativistic Hartree-Bogoliubov and RPA description of exotic nuclear structure", *RIKEN Review No.39*, 37 (2001).
12. N. Paar, D. Vretenar, P. Ring, and G. A. Lalazissis, "Collective properties of the low energy dipole response in the relativistic RPA" ,*The nuclear many-body problem 2001*, Eds. W. Nazarewicz and D. Vretenar, Kluwer Academic Publishers, 209-214 (2002).
13. D. Vretenar, P. Ring, G.A. Lalazissis, T. Niksic, P. Finelli, and N. Paar, "Relativistic Mean-Field And RPA Description Of Exotic Nuclear Structure" *Frontiers of Nuclear Structure*, Ed P. Fallon, American Institute of Physics Conference Proceedings 656, 211-218 (2003).